Rolling Contact Mechanics of Soft Elastomers on Engineered Surfaces

by

Brodie K. Hoyer

B.S., United States Military Academy, 2003

M.S., Stanford University, 2013

A thesis submitted to the

Faculty of the Graduate School of the

University of Colorado in partial fulfillment

of the requirements for the degree of

Doctor of Philosophy

Department of Mechanical Engineering

2022

Committee Members:

Mark Rentschler

Rong Long

William Doe

JianLiang Xiao

Francisco Lopez-Jimenez

Hoyer, Brodie K. (Ph.D., Mechanical Engineering)

Rolling Contact Mechanics of Soft Elastomers on Engineered Surfaces

Thesis directed by Mark E. Rentschler

This report details the experimental work done to characterize the rolling contact mechanics of engineered surfaces against highly deformable, tissue-like elastomers. This work is motivated primarily by the design of medical devices, including robotic capsule endoscopes (RCEs), endoscopy balloons, stents, catheters, and bandages. Each of these devices presents different challenges regarding different tissue interactions and optimization goals, but all rely to some extent on carefully tuned adhesive responses. A better understanding of the adhesive response of these surfaces could lead to a better models and a subsequent narrowing of the design field regarding microstructured surfaces.

Chapter 1 of this work is focused on the historical development of the contact theories that will serve as the theoretical framework on which the remainder of the research is built. Beginning with Hertz' pioneering work and continuing through modern theories incorporating adhesion, this chapter is meant to provide a brief theoretical introduction relevant to the remaining work.

Chapter 2 will focus on biological adaptations for locomotion. Driven by the basic urges to find shelter, food, and mates, many species have co-evolved, through millenia of adaptive pressure, highly advanced locomotive structures. This chapter will introduce several species and will discuss the mechanisms behind their adaptations, as well as some attempts to mimic them with engineered surfaces.

Chapter 3 presents the first aim of this work: the design, construction, and validation of a tribometric device capable of characterizing the rolling contact of soft elastomers. A device was developed capable of measuring the normal and tractive forces and contact area of a cylindrical indenter rolling freely against a fixed substrate with fixed indentation or fixed normal force and controlled translational velocity. The device was validated using a rigid acrylic cylinder and rate-

independent (polydimethylsiloxane (PDMS)) substrate, the results of which could be compared against classical contact theories. A second experimental setup, incorporating a thin (3 mm) shell of highly deformable and viscoelastic elastomer (polyvinyl chloride (PVC)) fixed to a rigid cylindrical core rolling on a flat PDMS substrate, highlights the novelty of this approach, in that the response varies greatly from analytical models due to high deformation, finite thickness corrections, and high viscoelasticity.

Chapter 4 presents the second aim of this work: the characterization of the rolling contact between elastomeric surfaces and a highly-deformable tissue-mimicking substrate. Using our tribometer, we conducted a series of rolling contact experiments involving a flat PDMS substrate and an indenter composed of a thin (3 mm) shell of PVC bonded to a rigid core. Using a range of normal forces and translational velocities, we observed tractive force dependencies on both velocity (due to the rate-dependent nature of interface energy) and normal force (due to friction caused by partial slippage of the interface). These results were compared to a finite element simulation using a Cohesive Zone Model (CZM) to simulate interfacial adhesion and a post-processing step relating normal and tractive surface tractions using Amonton's law for friction. The flat PDMS substrate was then replaced with a micropillared substrate and subjected to the same battery of tests. Through this, it was determined that the micropillars had only a modest effect on rolling contact, a finding we attribute to the high deformability of PVC leading to extensive backing layer contact between the micropillars.

Chapter 5 presents the final aim of this work: the use of readily-available manufacturing techniques for rapid prototyping of pillared surfaces in order to explore the pillar design space. The abundance of micro-manufacturing techniques, from micro-machining to lithography and laser etching molds, has created an effectively infinite design space regarding pillar shape, orientation, and aspect ratio. Because analytical solutions can rarely be determined for arbitraty pillar geometries, designers have two options for navigating the design space: simulation or developing and testing prototypes of varying pillar geometries. As many pillar shapes require the development of 3D simulations, necessitating either computationally-intensive whole-body models or the implementation of difficult and potentially non-physical boundary conditions on representative elements, prototyping offers a possible alternative to test various geometries quickly. Because many micro-manufacturing processes are time consuming or require access to highly specialized equipment, we set out to use two readily-available techniques, 3D printing and laser printing, to develop sub-millimeter mesopillars and studied the effect of their geometry on the contact mechanics with both rigid and soft indenters.

Chapters 6 and 7 present a list of the conclusions of each aspect of this work, as well as concluding discussion.

Dedication

This work is dedicated, with love, to my three children: Lorna, Cormac, and Viggo.

May you build a ladder to the stars and climb on every rung...

Acknowledgements

For their continual guidance, sound judgement, and encouragement, I would first like to thank my co-advisors on this project, Doctors Mark Rentschler and Rong Long. With your complementary abilities in device design, fundamental adhesion science, and scientific communication, you represented the very best in research collaboration and I thank you for shepherding this work to its fruition.

I would also like to thank the Faculty of the Department of Civil & Mechanical Engineering at the US Military Academy, not only for providing the opportunity and funding for embarking on this experience, but for providing so many mentors, both civilian and military, throughout my career.

Finally, and most importantly, I would like to thank my wife, Leeah. Pursuing a doctorate with a family inevitably involved tradeoffs in time and focus, and I could not have focused on my research without knowing that the kids were in good hands. Thank you, and I look forward to the next step in our family journey together.

Contents

Tables

Table

Figures

Figure

Chapter 1

Contact Mechanics

1.1 Contact Mechanics

Contact mechanics is the application of continuum solid mechanics to describe the state of stress, strain, and/or deformation within bodies which, by means of imposed force or displacement, have been brought into contact[1]. For some situations, as will be described in this chapter, the geometry and loading conditions of the bodies are such that analytical solutions exist to relate the relevant physical quantities. However, for many relevant applications, it is necessary to develop either numerical models using the Finite Element Method (FEM) or empirical relations through experimental methods.

1.2 Elliptical Bodies and Frame of Reference

In order to develop an analytical solution to a contact problem, the bodies in question must be *elliptical bodies*. The criteria for an elliptical bodies are that they must be smooth (showing no discontinuities or irregularities at any scale), and an equation describing their surface profile must be continuous up to their second derivative. Considering a general elliptical body a, there must exist an equation for the surface profile $z_a(x, y)$ such that

$$z_a(x, y) = A_1x^2 + B_1y^2 + C_1xy + \dots \tag{1.1}$$

[1] Unless stated or cited otherwise, the primary source of reference for this chapter is "Contact Mechanics" by K.L. Johnson, Cambridge University Press, 1985.

With proper selection of reference axes, the xy term is eliminated. For general elliptical contact (see Figure 1.1), the reference frame is thus defined such that the x and y axes coincide with the major and minor axes of the body, and z is defined as normal to the point of initial contact between the bodies.

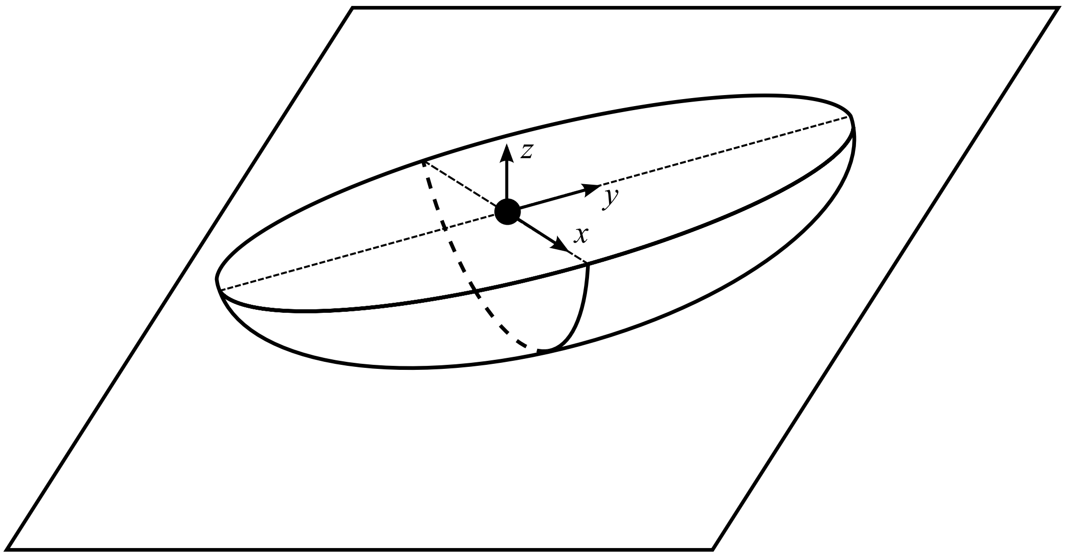

Figure 1.1: To find analytical solutions for general contact problems, the bodies in question are idealized into elliptical bodies, requiring that the bodies be both nominally smooth (no defects) and with surface profiles that are continuous up to their second derivative. The chosen reference frame typically coincides to the major axes of the body or bodies in question and the normal to the direction of contact.

In many cases, the geometry of the bodies can be adequately described in two dimensions. The two general cases in which this simplification is applicable are *bodies of revolution* in which a radial profile is understood to sweep axisymmetrically about a central axis and *cylindrical bodies* in which the radial profile is understood to extend continuously along an axis of the reference frame. Not only does this simplify the contacting geometries down to a single variable function, but it also allows for the simplification of the constitutive equations, as discussed in Section 1.4.3, to either a plane stress or plane strain condition, respectively.

Because it is most relevant to the test conditions and practical applications to be discussed throughout this document, we will focus hereafter on the contact mechanics of cylindrical bodies.

Cylindrical contact can occur when a long cylinder is pressed against a flat surface (see Figure 1.2a) or when two cylinders are pressed together such that their long axes are parallel. As shown in Figure 1.2b, the y axis corresponds to long axes of contact, x corresponds to the common tangent of both surface profiles at the instant of initial contact, and z coincides with the direction of contact. By convention, z is typically directed into the fixed body such that indentation and subsequent compressive forces are rendered positive.

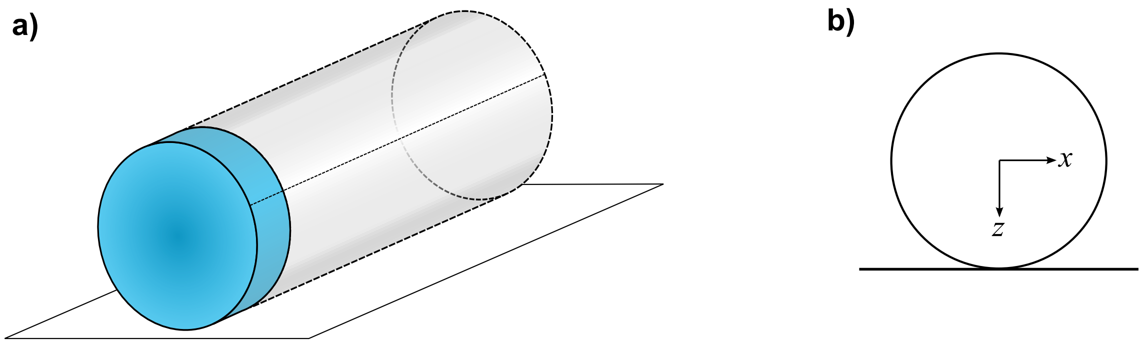

Figure 1.2: The simplifying assumption most relevant to rolling contact is that of *cylindrical contact*, in which a circular surface profile is assumed to extend along an axis common to both bodies. If the depth of the profile is much larger than the characteristic width of contact, the stress-strain relationship may be simplified to that of a plane strain condition.

1.3 Line Loading of an Elastic Half-Space

As stated in Section 1.1, the goal of contact mechanics is to relate the displacements and stresses within contacting bodies using continuum mechanics theories. In general two-dimensional cases, there are four possible boundary conditions which may be imposed at the contact interface: surface pressures ($p(x)$ for those normal to the surface and $q(x)$ for those tangential) and surface displacements ($\overline{u}_z(x)$ and $\overline{u}_x(x)$ for displacements into and along the body, respectively).[2]Surface tractions may be defined within the contact area as functions of the distance from the origin, or in some cases may be simplified to a point load applied at the origin. Normal displacements ($\overline{u}_z(x)$) may be defined by the shape of a rigid indenter. The state of interfacial friction can then be used to determine either the tangential displacement or tractions. If the interface is frictionless, $q(x) = 0$

across the surface. If a no-slip condition is specified, $\overline{u}_x(x)$ is zero through the area of contact.

In order to apply the Theory of Linear Elasticity to the contact problem, the characteristic geometries of the contacting bodies must be considerably larger than the contact width itself. If this is the case, the bodies may be treated as elastic half-spaces, semi-infinite bodies bound by plane surfaces. Under this assumption, contact stresses are concentrated near the contact area and fall to zero as the distance into the bodies approaches infinity. Moreover, the stress distributions within the body are unaffected by the shape of the bodies far away from the contact area nor by how they are supported. A further assumption relevant to cylindrical contact is that the axial length of the bodies in contact is large compared to the contact area. This allows the application of the plane-strain assumption, in which strain outside the plane defining the contact geometry is zero ($\epsilon_y = 0$).

1.4 Theory of Linear Elasticity

The theory of linear elasticity is the means by which the stresses (σ_{ii}, σ_{ij}), strains (ϵ_{ii}, ϵ_{ij}) and displacements (u_i) can be related for an arbitrary point within a continuum solid under equilibrium conditions. A linearly elastic solid is one in which there exists a linear transformation between stress and strain, or as stated in the Generalized Hooke's Law:

$$\sigma_{ij} = D_{ijkl}\epsilon_{kl} \tag{1.2}$$

where σ_{ij}, D_{ijkl}, and ϵ_{kl} represent the stress tensor, elastic modulus tensor, and strain tensor respectively. Without delving into the derivation of the elastic equations, there are several relations relevant to the solution of any linearly elastic contact problem.

1.4.1 Stress Equilibrium

For any point within a continuum solid at equilibrium, the following stress condition applies:

$$\sigma_{ij,j} + b_i = 0 \tag{1.3}$$

[2] Note that, as per Johnson, displacements or stresses occurring at the surface will be designated with an overbar.

where b_i represents a body force (force due to gravity, electromagentic forces, etc.), and in most cases is assumed to be zero. The reader is reminded that, in Einstein Notation, the comma implies differentiation.

Similarly, the state of stress for a point at the boundary of a continuum solid with imposed surface tractions can be related through the equilibrium condition

$$\sigma_{ij} n_j = T_i \tag{1.4}$$

where n_j represents the component of the surface normal in the j direction and T_i represents the component of the surface traction in the i direction. Relating this back to the conventions for cylindrical contact, for imposed surface tractions

$$\overline{\sigma}_{zz} = -p(x) \tag{1.5}$$

$$\overline{\sigma}_{xz} = -q(x) \tag{1.6}$$

within the loaded region and $\overline{\sigma}_{zz} = \overline{\sigma}_{xz} = 0$ without.

1.4.2 Displacements and Strain

A key component of linear elasticity and elastic half-spaces is that of infinitesimal strain. When strains are considered infinitesimal, strain and displacement are related by

$$\epsilon_{ij} = \frac{1}{2}(u_{i,j} + u_{j,i}) \tag{1.7}$$

Moreover, any point within the continuum must meet the strain compatibility criterion

$$\epsilon_{ii,jj} + \epsilon_{jj,ii} = \epsilon_{ij,ij} \tag{1.8}$$

1.4.3 Constitutive Equations

As stated previously, stress and strain can be related through the Generalized Hooke's Equation (1.2). If the material in question is linear and isotropic, this relationship can be simplified in such a way that the two tensors can be related through two material constants: the Poisson ratio ν and Young's modulus, E. In the case of cylindrical contact, the problem is further simplified using the plane-strain assumption ($\epsilon_{yy} = \epsilon_{xy} = \epsilon_{yz} = 0$), and the remaining stress-strain relationships are

$$\epsilon_{xx} = \frac{1}{E}[(1-\nu^2)\sigma_{xx} - \nu(1+\nu)\sigma_{zz}] \tag{1.9}$$

$$\epsilon_{zz} = \frac{1}{E}[(1-\nu^2)\sigma_{zz} - \nu(1+\nu)\sigma_{xx}] \tag{1.10}$$

$$\epsilon_{xz} = \frac{1}{E}(1+\nu)\sigma_{xz} \tag{1.11}$$

$$\sigma_{yy} = \nu(\sigma_{xx} + \sigma_{zz}) \tag{1.12}$$

1.5 Hertz Contact Theory

Modern treatment of contact mechanics begins with Hertz, who developed his theory on the elastic contact of elliptical solids [41] based on his observation of the elliptical interference fringes formed when lenses are pressed together. Hertz theory is based on the assumptions of linear elasticity and elastic half-spaces. Additionally, Hertz theory assumes a frictionless interface and that there is no adhesion between the bodies - forces are compressive through the contact area and zero without.

In the case of cylindrical contact, we will assume that both cylinders are of circular profile described by their respective radii, R_1 and R_2. At the point of initial, no-load contact (see Figure 1.3a), the two bodies meet at the origin and their respective profiles are given by

$$z_{1,2} = \pm\frac{1}{2R_{1,2}}x^2 \tag{1.13}$$

More instructive is to define the *gap function* between the two, with the distance between the two surfaces as

$$h = z_1 - z_2 = \frac{1}{2}\left[\frac{1}{R_1} + \frac{1}{R_2}\right]x^2 \tag{1.14}$$

Under a compressive load P, the two bodies will undergo a compressive displacement δ. Because the bodies are unable to interpenetrate, the contact spreads from a point to a finite area, as shown

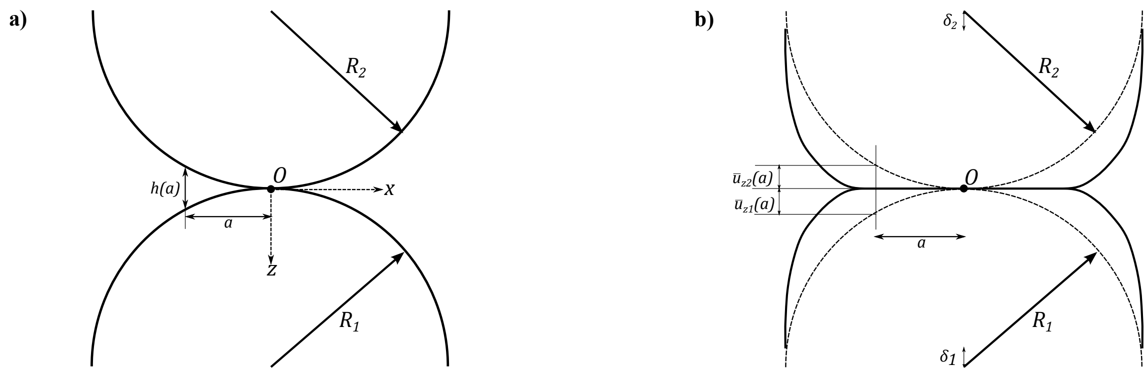

Figure 1.3: Hertzian Contact of Smooth Cylinders. At the point of initial contact, under zero load (Figure 1.3a), the bodies meet at a single point (O), and the gap between the bodies ($h(a)$) is a function of the distance from the origin. As a compressive load is applied (Figure 1.3b), the contact extends to a finite region. Within the region, the total surface displacement of coincident points on the bodies is equal to the difference between the displacement δ and gap function $h(a)$.

in Figure 1.3b. Assuming that the points of contact within the contact area are coincident, we can relate the surface displacements within the contact area to the displacement:

$$\overline{u}_{z,1} + \overline{u}_{z,2} = \delta - h \tag{1.15}$$

Similarly, any points that lie outside the contact area do not displace sufficiently to come into contact, so the combined displacement must be less than the difference between the displacement and the original gap at that distance

$$\overline{u}_{z,1} + \overline{u}_{z,2} < \delta - h \tag{1.16}$$

Any valid contact theory must satisfy the above displacement conditions.

In order to formulate his theory, Hertz assumed that the interface between the two solids was frictionless ($q(x) = 0$) and that any contact pressure $p(x)$ acted along the z-axis. Thus, the problem of Hertz theory became finding a pressure distribution that would satisfy (1.15) within the contact region and (1.16) without.

Before progressing into Hertz' derivation for cylindrical contact, we must introduce three variables relevant to the theory. The contact half-width a is defined as the distance from the center of the contact region to the outer edge in the x-direction. R is the characteristic radius for the two bodies

$$\frac{1}{R} = \frac{1}{R_1} + \frac{1}{R_2} \tag{1.17}$$

Finally, E^* is the composite plane-strain modulus for the materials of the two bodies

$$\frac{1}{E^*} = \frac{(1-\nu_1^2)}{E_1} + \frac{(1-\nu_2^2)}{E_2} \tag{1.18}$$

Given the definition for R, the gap equation can be rewritten

$$h(x) = \frac{1}{2}\,(1/R)\,x^2 \tag{1.19}$$

Furthermore, equations 1.15 and 1.16 become

$$\overline{u}_{z1} + \overline{u}_{z2} = \delta - \frac{1}{2}(1/R)x^2 \tag{1.20}$$

within the contact area and

$$\overline{u}_{z1} + \overline{u}_{z2} < \delta - \frac{1}{2}(1/R)x^2 \tag{1.21}$$

without.

Differentiating 1.20 within respect to x, we have

$$\frac{\partial \overline{u}_{z1}}{\partial x} + \frac{\partial \overline{u}_{z2}}{\partial x} = -(1/R)x \tag{1.22}$$

The surface gradient due to a normal pressure distribution over a finite area is an already established relationship. Because the bodies are in equilibrium, the pressure distribution is equal in both. Thus, for a pressure $p(x)$ leading to a contact half-width a

$$\frac{\partial \overline{u}_{z1}}{\partial x} + \frac{\partial \overline{u}_{z2}}{\partial x} = -\frac{2}{\pi E^*}\int_{-a}^{a} \frac{p(s)}{x-s}ds \tag{1.23}$$

Substituting into 1.22, we have

$$\int_{-a}^{a} \frac{p(s)}{x-s}ds = \frac{\pi E^*}{2R}x \tag{1.24}$$

Integrating the left-hand side, we are left with the expression

$$p(x) = \frac{1}{\pi(a^2-x^2)^{1/2}}\left[P - \frac{\pi E^*}{4R}(x^2-a^2)\right] \tag{1.25}$$

As stated previously, Hertz theory allows only compressive (by convention, positive) stresses. The pressure $p(x)$ must then be positive throughout the contact region $-a < x < a$. Therefore $P \geq \pi a^2 E^*/4R$. Moreover, if P is greater than the right-hand side of the expression, the pressure rises to infinity as x approaches a. This would subsequently lead to an infinite surface gradient at the edge of contact, a situation which is physically impossible. Therefore, we can relate the compressive force P to the contact half-width through the relation

$$P = \frac{\pi a^2 E^*}{4R} \tag{1.26}$$

In the analysis of many contact problems, it is instructive to relate the contact force P to the compressive displacement δ, not least because the integration of force over distance provides a quantitative measure of work. This is not possible with cylindrical contact, however. In order to equate the two, it must be assumed that the surface displacement approaches zero at an infinite distance from the contact area. Integration of the surface gradients for cylindrical contact, however, will lead to a decrease of $\ln(x)$. A reasonable approximation for the two is

$$\delta = P\frac{1-\nu^2}{\pi E}[2\ln(2d/a) - \nu/(1-\nu)] \tag{1.27}$$

Where d represents an arbitrary datum a fixed distance from the center of contact. It should also be noted that this approximation requires that one body be considered rigid, as it is replaced by an equivalent Hertzian pressure distribution.

1.6 Adhesive Contact: The JKR and DMT theories

As contact mechanics progressed, a disparity between Hertzian predictions and observed results was noted: in some situations, Hertz underpredicted the contact area for a given force. Moreover, particularly when dealing with softer materials such as rubber or gelatine, finite contact areas were observed under zero load and negative "pull-off" forces were recorded prior to separation. These phenomena were attributed to adhesion, a surface characteristic negated in Hertz. On the molecular level, adhesion can be described in terms of a surface potential defined by an equilibrium separation z_0. When points are brought closer within z_0, the potential is repellent and beyond z_0 the potential is attractive. This potential field decreases rapidly, however, usually extending only to nanometers. Thus, the phenomenon is only practically observed under atomically smooth solids or highly deformable bodies.

In the 1970's, two theories were developed to explain adhesive contact, that of Derjaguin-Muller-Toporov (DMT) [22] and Johnson-Kendall-Roberts (JKR) [49]. DMT theory assumes no additional deformation of the bodies beyond Hertz predictions but describes an adhesive zone immediately outside the contact region due to surface potentials. JKR, however, proposes that attractive surface potentials pull the elastic bodies together, increasing the actual contact region (see Figure 1.4 for comparison). Separating the two bodies requires work input to separate the interface. Because it is more relevant to the contact of highly-deformable bodies, continuing discussion will focus on JKR Theory.

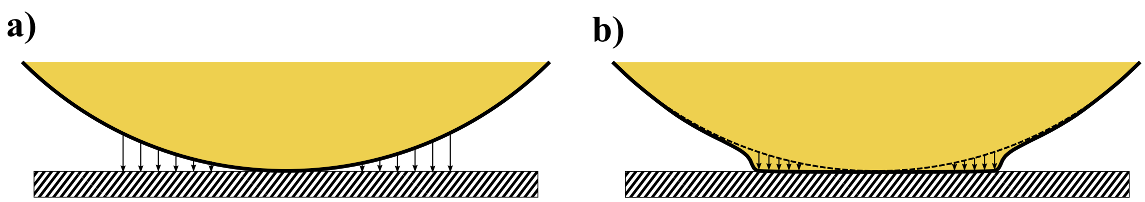

Figure 1.4: A comparison of adhesive contact for DMT (a) and JKR (b) theories. In DMT theory, no additional contact area is created, but adhesive potentials exist outside the contact region. In JKR, the adhesive forces pull the surfaces together, increasing the contact area for a given force.

In order to relate the applied force P to the contact half-width a under adhesive conditions, a Fracture Mechanics approach is required. We begin by revisiting the pressure distribution, rearranging to highlight the Hertzian contribution

$$p(x) = \frac{1}{\pi(a^2 - x^2)} \left[P - \frac{\pi E^* a^2}{4R}(2x^2/a^2 - 1) \right] \tag{1.28}$$

We can now see that the multiplicative term in the brackets is equal to the force predicted by Hertz, which will be referred to for the remainder of this section as P_H. Hertz then, assumed that the force P was equal to that quantity to avoid the square root singularity. However, after Griffith's development of linear elastic fracture mechanics [37], techniques are available to account for these singularities. First, we assume that P is less than that predicted by Hertz due to the presence of tensile surface tractions [18]. As x approaches a, the pressure approaches infinity, so we treat the edge of contact as a Mode-I crack tip, and define a stress intensity factor

$$K_I = \frac{P_H - P}{\sqrt{\pi a}} \tag{1.29}$$

In linear elastic fracture mechanics, the stress intensity factor is related to the strain energy release rate G as $G = K_I^2/2E^*$. JKR further equates the strain energy release rate to the work of adhesion w_{adh}. Thus

$$G = w_{adh} = \frac{K_I^2}{2E^*} = \frac{(P_H - P)^2}{2\pi E^* a} \tag{1.30}$$

Solving for the force P

$$P = \frac{\pi E^* a^2}{4R} - \sqrt{2\pi E^* a w_{adh}} \tag{1.31}$$

Equation 1.31 has several implications for observed contact. First, the actual load for a given contact width is reduced from the Hertzian prediction by the adhesive term, which is dependent on the material properties, length of contact, and work of adhesion. This also implies that a finite contact area will exist under zero load. Finally, adhesive contact can sustain negative (tensile) loads prior to separation.

1.7 Rolling Contact

The equations developed above are based on indentation and retraction, with contact characterized by two crack fronts, equidistant from the center of the indenter, opening or closing with equal work of adhesion. Rolling contact, by constrast, involves a crack closing at the leading edge of contact and a crack opening at the trailing edge (Figure 1.5b). Because the work of adhesion during separation is typically much larger than for indentation in most materials [17, 76], the contact area will tend to lengthen towards the trailing edge and shorten at the leading edge. For such

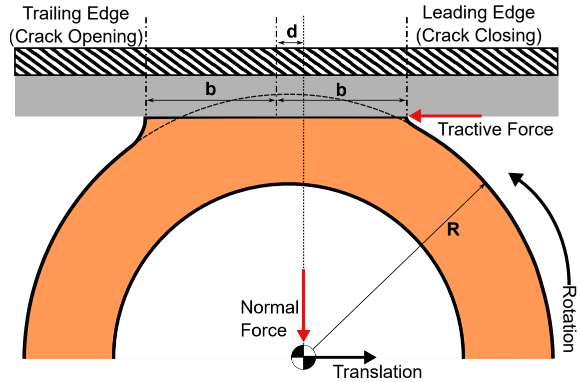

Figure 1.5: Adhesive rolling contact is characterized by the progression of two crack fronts: an opening crack at the trailing edge and a closing crack at the leading edge, governed by the work of separation and adhesion, respectively. Because work of adhesion is typically smaller, the contact area will be pulled backward a distance d from the center of the indenter.

asymmetric contact, the normal surface traction within the contact area is [16]

$$\sigma(r) = \frac{-P/\pi + (E^*/2R)(r^2 - rd - b^2/2)}{(b^2 - r^2)^{1/2}}, \tag{1.32}$$

with d representing tangential distance from the center of the indenter to the center of the contact area (Figure 1.5b) and r representing the distance of a point from the center of contact. Because the work of adhesion and separation are not equal, the crack tips must be evaluated independently. Using the leading edge of contact as an example, it is necessary to first solve for the Mode-I stress intensity factor [76]

$$K_{I,lead} = \lim_{r \to b} \sigma(r)[2\pi(b - r)]^{1/2}. \tag{1.33}$$

Because the crack tip is in equilibrium, the stress intensity factor can be related to the strain energy release rate G and work of adhesion as

$$w_{adh} = G = K_{I,lead}^2/2E^*. \tag{1.34}$$

By solving the two equations above and relating the the torque on the indenter to the contact asymmetry through the integral of the surface traction, the resulting relationship is [76, 75]

$$P = \frac{\pi E^* b^2}{4R} - \sqrt{2\pi E^* b w_{adh}} - \frac{\pi E^* b d}{2R}, \tag{1.35}$$

with F representing the tractive force on the indenter. In a similar fashion, the work of separation at the trail edge is equal to

$$P = \frac{\pi E^* b^2}{4R} - \sqrt{2\pi E^* b w_{sep}} + \frac{\pi E^* b d}{2R}. \tag{1.36}$$

Additionally, by considering the equilibrium of forces acting on the indenter, a relation between the external forces and characteristic lengths of contact can be derived [16]:

$$P = \frac{\pi E^* b^2}{4R} - \frac{FR}{d} \tag{1.37}$$

Using Equations 1.35, 1.36, and 1.37, we can derive an expression for the difference between the work of separation and work of adhesion:

$$w_{sep} - w_{adh} = F \tag{1.38}$$

which is in agreement with Kendall's theory [52]. It is important to note that the theoretical calculations above assume surface tractions only in the normal direction. Thus, rolling is a function only of the disparity in adhesive energies and not of interfacial friction.

1.8 Additional Factors

When considering adhesive contact of soft materials, there are several other factors which should be considered when comparing observed results with theoretical expectations. The first consideration is viscoelasticity, the tendency of a material's response to a load to be affected not only by the magnitude of the load but also by the rate at which it is applied. During the separation of soft materials, viscoelastic loss at the crack tip is a primary source of dissipated energy loss. In the case of rolling contact, this can lead to a strong velocity-dependence for measured forces. A second consideration is that of finite-size correction factors. All of the previously discussed contact theories are based on the elastic half-space assumption, implying that the geometry and fixturing of the contacting bodies do not affect the stress distributions within. However, as described by Shull [77], when the contact width approaches the characteristic thickness of either body, that assumption is no longer valid, causing significant deviations from expected values. A third consideration is the inherent surface roughness of the bodies. Because attractive forces decay rapidly over microscopically short length scales, the extent of adhesion is typically much smaller than predicted. Although this is somewhat negated by the high deformability of soft materials, it must still be considered, particularly if one of the contacting bodies is rigid.

Chapter 2

Biomimetics: Inspiration from Evolutionary Adepts

2.1 Introduction

Biomimetics is the study of biological structures, systems, or processes with the goal of developing an engineered analog to better accomplish a task or solve a problem. Driven by the opposing drives to hunt and evade, to eat and not be eaten, biological organisms have, over millennia, evolved naturally optimal adaptations to their environment. These adaptations include, but are certainly not limited to, locomotion (walking, climbing, swimming, flying), sensing the environment, attacking and defending, communicating, converting and storing energy, and reproducing.

2.2 Locomotion

Locomotion (for the purposes of this study limited to crawling, walking, running, and climbing) is a key evolutionary adaptation. The extent to which an organism can navigate terrain determines their access to nutrients, shelter, and potential mates. Moreover, organisms that can traverse terrain efficiently are more likely to access limited resources, will expend less energy doing so, and are more likely to either catch prey or avoid predators than their less-efficient counterparts. In the following sections, we will discuss a number of locomotive adaptations in organisms and then discuss the principles behind their respective adaptations.

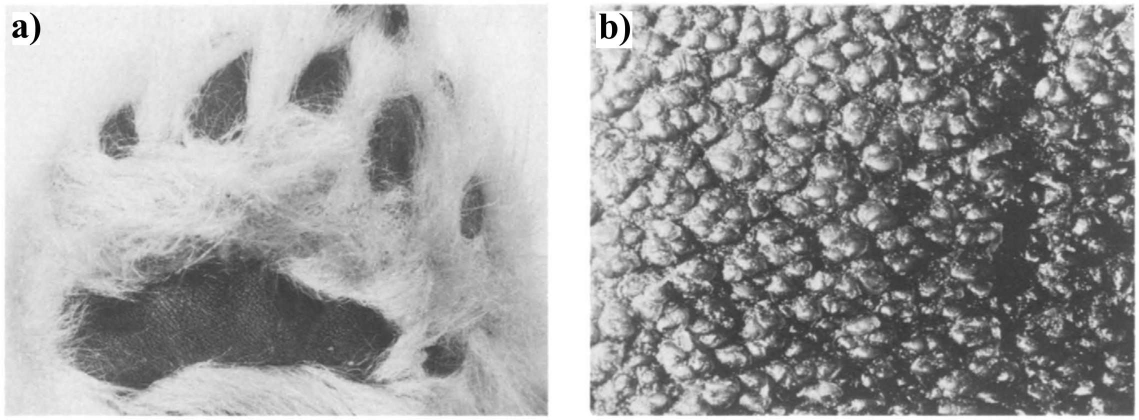

Figure 2.1: Macro- and microscopic view of the polar bear footpad. Figure 2.1a shows the totality of a polar bear footpad, while Figure 2.1b shows the papillae on the footpad. Although no scalebar is given, the papillae average 1mm in diameter. Taken from Manning et al. 1985 [61], ©Sage Publications 1985.

2.2.1 Polar Bears: Macroscopic Adaptation to a Harsh Environment

In 1985, the team of Manning et. al. endeavored to study the footpads of polar bears in order to determine an optimal surface treatment for rubber-soled shoes to minimize slippage [61]. The team studied the footpads of one male and one female polar bear using optical and scanning electron microscopy (SEM). SEM images revealed areas of raised papillae approximately 1.0 mm in diameter (Figure 2.1), as well as some areas with circular depressions. These structures were formed from a keratinous layer approximately 10 cells deep. On the macroscopic layer, the team registered a mean hardness of 24 on the Shore A scale. This hardness correlates to many silicon and natural rubbers. Although not particularly instructive, this study highlights, on a macroscopic scale, a trend which will be repeated later on the microscopic: a hard, keratinous terminal to an overall soft structure. Although not specifically mentioned in this study, the combination likely allows for maximum contact area of the footpad while still providing traction laterally.

2.2.2 Insect Attachment Structures: Two Divergent Adaptations

Insects provide a wealth of case studies on biological adhesion. For crawling and climbing insects, access to food sources may require the navigation of vertical or overhung structures of drastically varying roughness and compliance, in either wet or dry conditions. Even flying insects must often be able to land on and navigate vegetation in order to access food or shelter. This evolutionary drive has led to two broadly categorized adaptations: smooth and hairy attachment pads. Smooth attachment pads are observed most prominently in the orders *orthoptera* (grasshoppers,

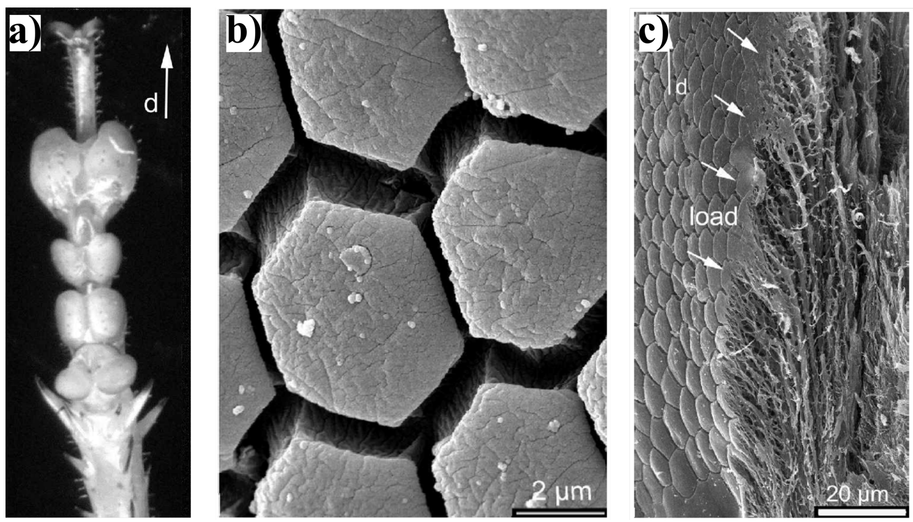

Figure 2.2: Detail of the locomotive structure of the great green bush-cricket (*t. viridissima*). Figure (a) shows the overall tarsal structures of the insect leg. Figure (b) shows the smooth hexagonal structures of the pads, while (c) shows both the fibrillar substructure, as well as preferential bending behavior. Courtesy Gorb et al. 2000 [34], ©Springer-Verlag 2000.

crickets, and locusts), *hymenoptera* (bees, wasps, and ants) and *mecoptera* (scorpionflies). Under magnification, it is seen that smooth is a misnomer, as the pads themselves are often patterned in repeating hexagonal shapes (see Figure 2.2b) or lines. In a series of studies conducted on the great green bush-cricket (*t. viridissima*), Gorb et al. [34, 35] characterized the structure of the footpad as having a smooth, hexagonal surface supported by hierarchical supportive threads (Figure 2.2c). This structural combination is highly deformable, with a measured modulus of 27.2 ± 11.6 kPa, ensuring maximal replication of the substrate, down to the micrometer scale. Additionally, the subsurface structure of the pads is directional, preferentially bending in one direction under load (Figure 2.2c), creating frictional anisotropy favoring forward movement.

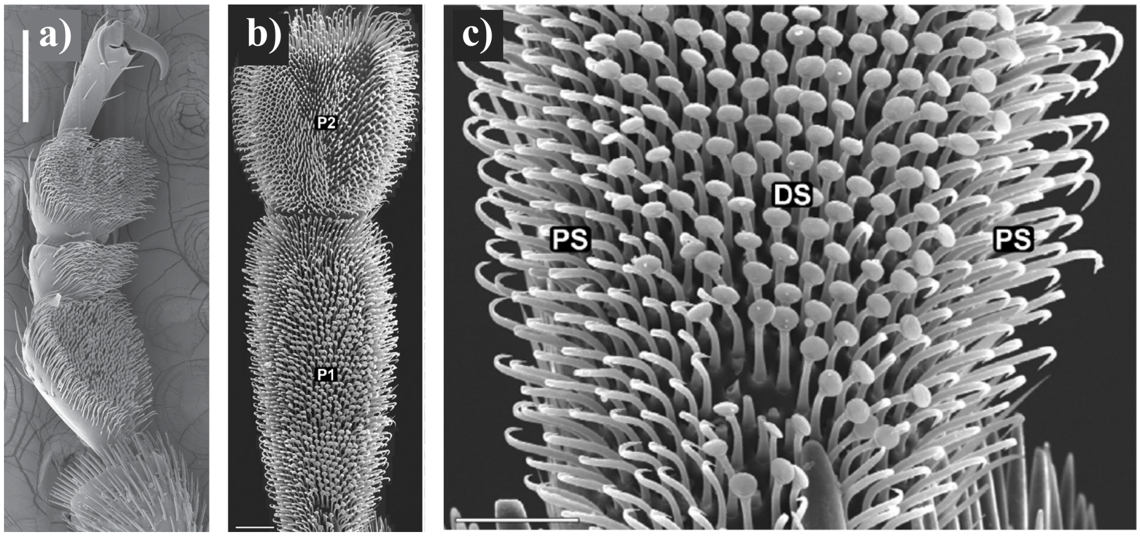

Figure 2.3: Detail of the adhesive structure of the dock (a) and ladybird (b) beetles. Both beetles display tarsal structures with tenent setae with varying distributions of pointed (PS) and discoid (DS) seta. Scalebar for (a) is 200 µm and (b),(c) is 20 µm. (a) courtesy Gernay et al. 2017 [31] ©The Authors 2017, (b),(c) courtesy Moon et al. 2012 ©The Authors 2012.

Hairy attachment structures have been found prominently among many hexapods, to include beetles and flies, as well as spiders. In the case of beetles, various studies [31, 63, 42] find that the tarsal structures of beetles are covered in tenant setae, ranging in length from 30-40 µm, with terminal structures that are either pointed (PS) or discoid (DS) (Figure 2.3c). The ends of the setae adhere primarily through intermolecular forces [42], so it is imperative to maximize contact over microscale roughness. Thus, the setal stalks provide maximum compliance in the normal direction.

Spiders also exhibit hair-like setal structures [72] for much the same reasons highlighted above. Spiders, however, show a higher degree of complexity in that their setal structures are hierarchical. That is, each setae is covered in thousands of smaller structures, called mitochondria, which are terminated with flat spatulae (Figure 2.4). These spatulae then exert the adhesive force on smooth, hard substrates, so a maximal number of spatulae in contact is critical for locomotion.

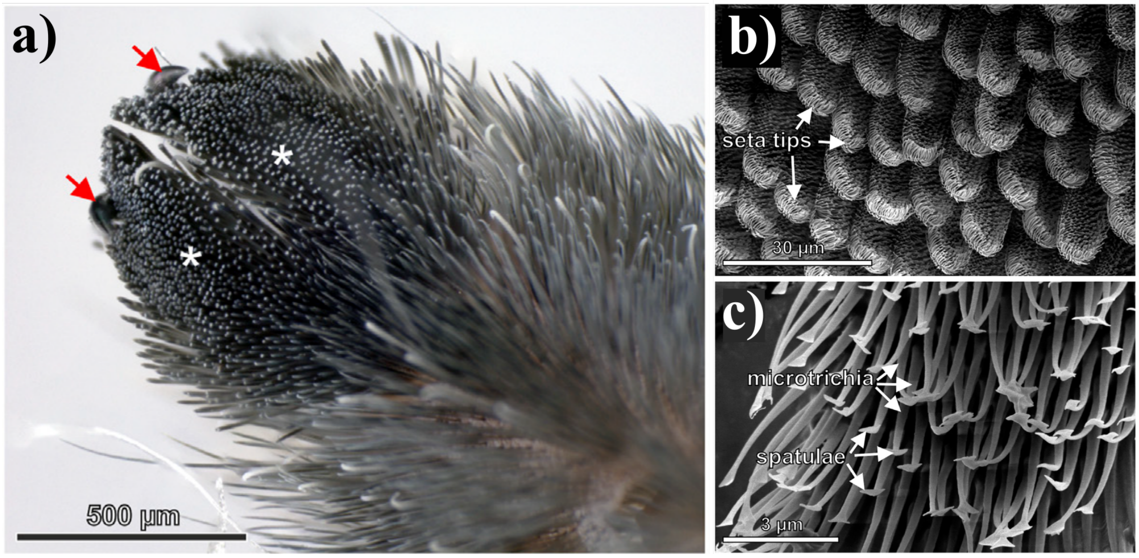

Figure 2.4: Detail of the adhesive structure of the spider *cupiennius salei*. Like the beetles above, the adhesive structures are characterized by thousands of hair-like setae (a). Each setae is further covered with thousands of mitochondria (b) which terminate at spatula-like tips (c). Courtesy of Poerschke et al. 2021 [72] ©The Authors 2021.

2.2.3 Tree Frog Attachment

Tree frogs encounter, and must be able to grip onto, a wide variety of surfaces, to include tree bark, leaves, rocks, and the skin of fellow frogs, all under varying conditions of wetness. As such, they have evolved complex adhesive structures (Figure 2.5) [24]. The frog toe pads themselves are disc-like and covered with polygonal cells of epithelial tissue, typically 10-40 µm in diameter, separated by 1 µm channels. These cells are, in turn, covered with smaller polygonal structures ranging from 0.1-0.4 µm. The hierarchical arrangement is common to many biological adhesive structures. A survey of tree frog research [57] shows that, barring one outlier, the modulus of the toe pad itself is typically on the order of 4-50 kPa.

Because mucus secretion mechanisms are incorporated into each toe pad, it was originally thought that tree frog adhesion was dominated by *wet adhesion* - adhesion driven by capillary forces created by liquid bridges in the channels between the epithelial cells and associated nanostructures. However, a study by Federle et al. [24] showed that the nanostructures reached a contact distance

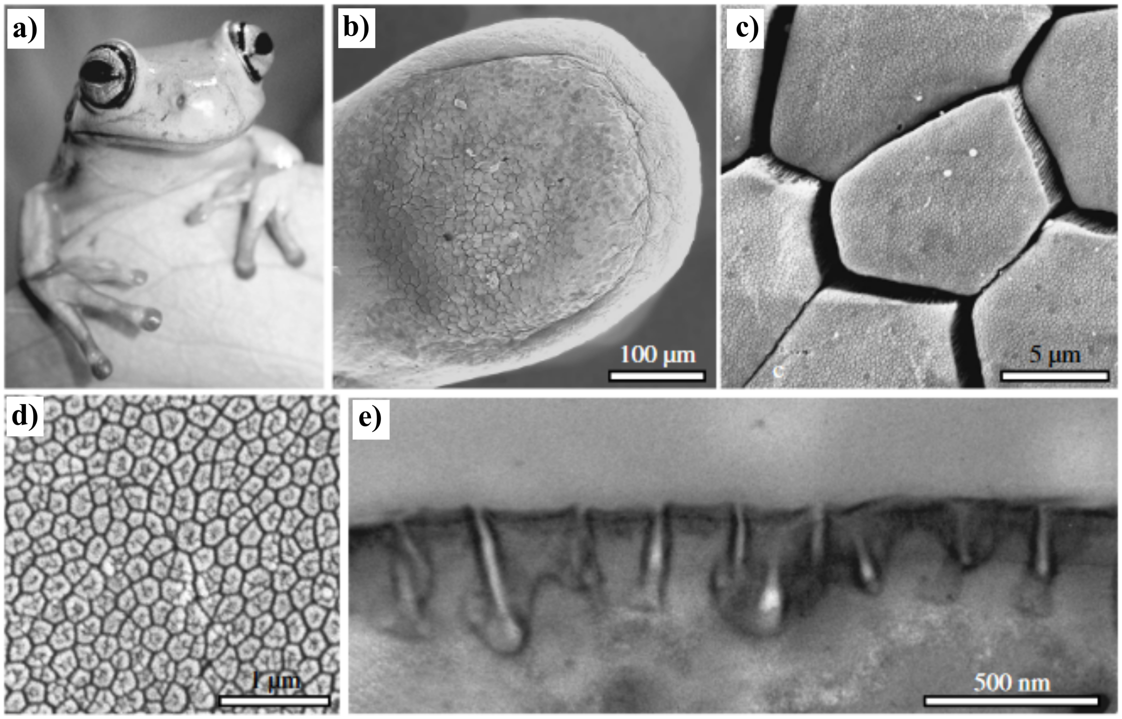

Figure 2.5: Detail of the adhesive structure of a typical tree frog (a). (b) SEM image of an individual toe pad, (c) epidermis highlighting hexagonal epithelial cells, and (d) surface of an epithelial cell. (e) cross-section of cell surface. courtesy Federle et al. 2006 [24] ©The Royal Society 2006.

too shallow to allow for capillary action. Tree frog adhesion is likely a complex combination of capillary action between the epithelial cells and intermolecular forces between the substrate and the nanostructures that is both direction and substrate dependent. Regarding the dry component of the adhesion, it is instructive that the tree frogs, like spiders geckos, have evolved hierarchical structures to maximize real contact area against the substrate.

2.2.4 Geckos: The Gold Standard for Climbing Animals

Almost every study of biomimetic adhesion includes the Gecko, and for good reason. The climbing ability of the Gecko is arguably without equal, capable of traversing up to 20 body lengths per second in vertical and overhung terrain [2], and capable of holding a force of 20 N on vertical terrain, which is roughly 40 times their average body weight (500 mN) [46]. Perhaps even more remarkable than the strength of the Gecko's grip is its reversibility - Geckos toe pads are able to detach completely in the span of 15 ms, and are able to do so without carrying along surface particles or contaminants. Observations of the Gecko's remarkable ability have led scientists for centuries to study the underlying mechanisms. However, the mechanisms would remain largely speculation until the 1990's and early 2000's, when imaging and force measurement technology would permit investigation on the microscopic level.

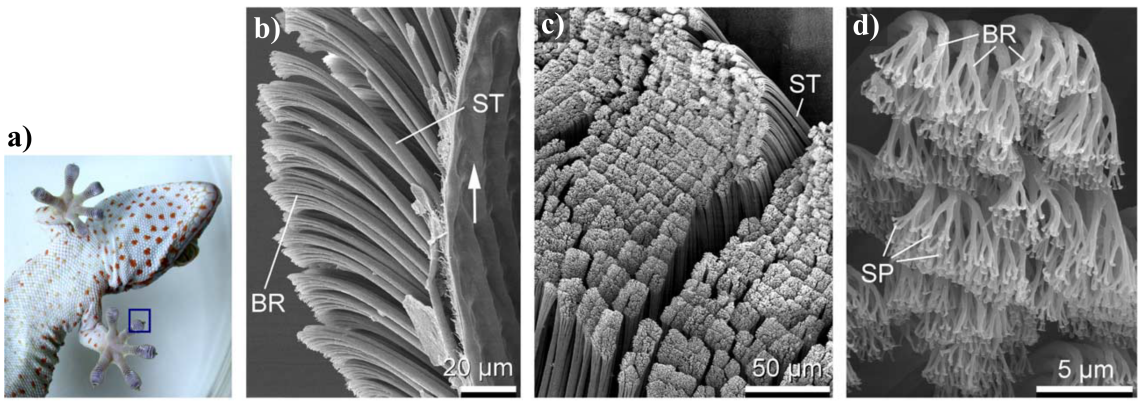

Figure 2.6: Detail of the adhesive structure of a typical Gecko (a). Each toe pad is covered with thousands of setae (ST) approximately 100 µmin length (c). Each toe pad subsequently branches (BR) hundreds of times (b) to terminal, keratinous structures called spatulae (SP) (d). These hierarchical structures enable the Gecko's remarkable climbing ability. Courtesy Gao et al. 2005 [29] ©Elsevier Ltd. 2004.

As with the insects above, the origin of the Gecko's climbing ability is the microstructure of their footpads (Figure 2.6). Each toe pad is covered with thousands of microscopic hair-like structures called *setae*, at an areal density of approximately 14,400 setae per mm^2 [4]. Each setae is approximately 100 µm long and 5 µm in diameter. Each setae then branches into hundreds of smaller *spatulae*, which terminate in flat triangular structures of keratinous tissue approximately 200 nm wide.

Studies by Autumn et al. on the adhesive force of a single setae indicate that the adhesion generated is highly directional and dependent on preload. When subjected to a small (40 µN) preload and shear displacement of 5 µm, the setae produced shear forces on the order of 200 µN, roughly 32 times that predicted by whole-lizard studies [3]. The apparent over-engineering is likely due to the fact that the majority of setae cannot be expected to make contact on rough, irregular surfaces or in the case of gait-interrupting events like attack, wind, etc. As to the reversibility of adhesion, the team found that the adhesive strength of the setae greatly diminished when the direction of pull reached 30°. This is achieved through the morphology of the Gecko toes themselves - Geckos have the ability to hyperextend their toes rearward, essentially peeling away the contact area (this is evident in Figure 2.6a).

It has been shown that the primary driver of Gecko adhesion is intermolecular (van der Waals) interactions which, as stated previously, decay rapidly beyond the nanometer range. This highlights the key advantages of a hierarchical structure such as that of the Gecko and the hairy-footed insects. Hierarchical structures provide maximal compliance in the normal direction, increasing the area of true contact between pad and subsrate. Further, they are flaw insensitive - a Gecko requires only a fraction of setae to be in adhesive contact with the substrate in order to remain affixed to the surface. These and other mechanistic explanations for biological adhesion will be discussed in the following section.

2.3 Mechanisms of Biological Attachment

Having explored several examples of locomotive adaptations, the next logical step is to discuss the mechanistic explanations for these adaptations. Fibrillar structures have co-evolved on animals as diverse as insects and geckos, implying that they are the most advantageous for climbers, and there are several reasons why. At the macroscopic level, conformance is certainly a factor. For the case of the Gecko, the keratinous material of the spatulae is more akin to metals or bone, with a modulus on the order of 1 GPa, and yet the modulus of the toe pad itself is at the range of a single MPa [29]. This macroscopic softness leads to better contact, increasing the ratio of the actual contact area, limited to the asperities of a roughened surface, to the apparent contact area set by the geometry of the toe pad. Because most adhesive phenomena are areal, increased contact area leads to stronger adhesion. This, however, is not the only, nor likely even the most important, adhesion enhancing phenomenon. Three other mechanisms relevant to biological adhesion in fibrillar structures are crack trapping, contact splitting, and directional compliance.

2.3.1 Crack Trapping

To understand crack trapping, we are reminded that, according to JKR Theory, the separation of two joined surfaces is akin to the formation and propagation of a crack in a solid body. The edge of contact is treated as a crack tip. As the bodies are pulled apart, elastic strain energy in the bodies increases and a stress concentration forms at the contact boundary. Eventually, the stress intensity at the crack tip reaches a critical value, and the crack propagates inwardly in an unstable fashion, fueled by the stored elastic energy. Once initiated, crack propagation is unstable at any length scale, provided that the bodies are continuous, and this helps to explain the advantage of microstructure.

If, instead of a single continuous surface for an indenter (or toe pad), there existed instead a series of independent microstructures, the gap between each microstructure would represent a discontinuity to the path of crack propagation. As the crack reached the edge of a microstructure, the propagation would cease and a portion of the elastic energy would be dissipated back into the bodies. Then, the process of initiating and propagating the crack would have to be reinstated at the next microstructure, requiring additional energy input. This effect is more pronounced if the materials in question display dissipative qualities such as visco- or poroelasticity.

Glassmaker et al. set out to demonstrate this phenomenon in engineered surfaces using a film-terminated fibrillar interface (Figure 2.7) [32]. Their surface featured hexagonal arrays of 14-µm square micropillars formed from polydimethylsiloxane (PDMS) with a thin (4 µm) terminal film of PDMS between the pillars (Figure 2.7). Using both a modified double cantilever beam (DCB) and spherical indentation experiment, they found adhesion enhancement of 2-9 times over the flat PDMS control. They attribute this to the fact that, although energy is released when the crack passes over a fibril, it is absorbed when passing over the film between fibrils. Thus, the energy release rate as a whole is much less than that of the flat control, requiring more work to be put into the separation of the surfaces and a higher pull-off force.

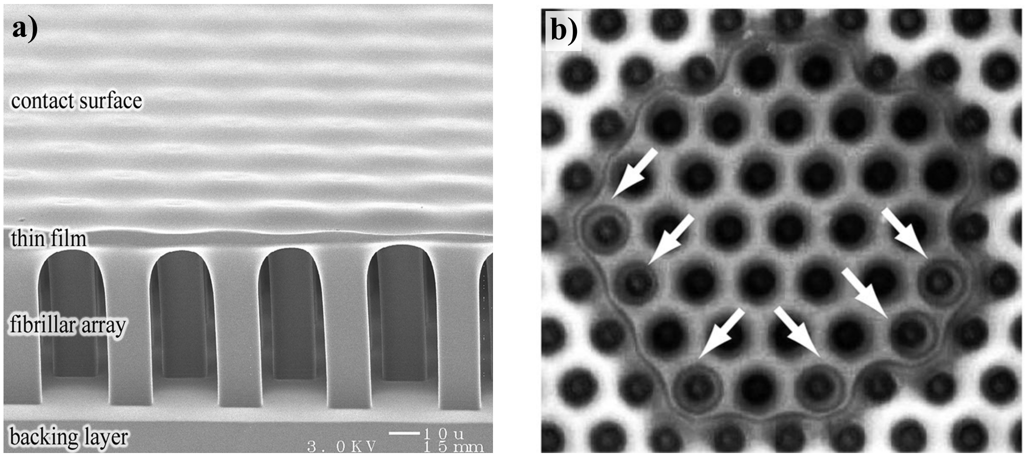

Figure 2.7: (a) SEM image of the film-termitated fibrillar structure used to mimic biological crack trapping in [32]. (b) Visual evidence of the crack trapping phenomenon; rather than progressing to the center of the indenter, individual crack fronts must traverse individual fibrils incrementally. Courtesy Glassmaker et al. 2006 [32] ©The National Academy of Sciences 2007.

2.3.2 Contact Splitting

In analyzing the adhesive structures of animals that utilize hierarchical attachment structures, a paradoxical trend arises: namely, as body mass increases, the size of terminal structures decreases. The gecko, the most massive animals to use fibrillar structures for locomotion, have the smallest spatulae, at only 200 nm. From this observation, Arzt et al. [1] came to the conclusion that the areal density N_A of fibrillar structures is crucial to adhesion, and they further developed a mathematical scaling law that matched remarkably well with biological observation.

To understand the contact splitting phenomenon, first begin by envisioning a toe pad as a single hemispherical structure radius R (Figure 2.8a). Using standard JKR theory, the critical pull-off force for that structure is

$$F_c = \frac{3}{2}\pi R\gamma \tag{2.1}$$

with γ representing the surface energy between toe pad and substrate. If that single hemisphere were divided into n smaller hemispheres of radius $R/\sqrt{n}$ (Figure 2.8b), the pull-off force to remove all the hemispheres becomes

$$F_c' = \sqrt{n}\frac{3}{2}\pi R\gamma = \sqrt{n}F_c \tag{2.2}$$

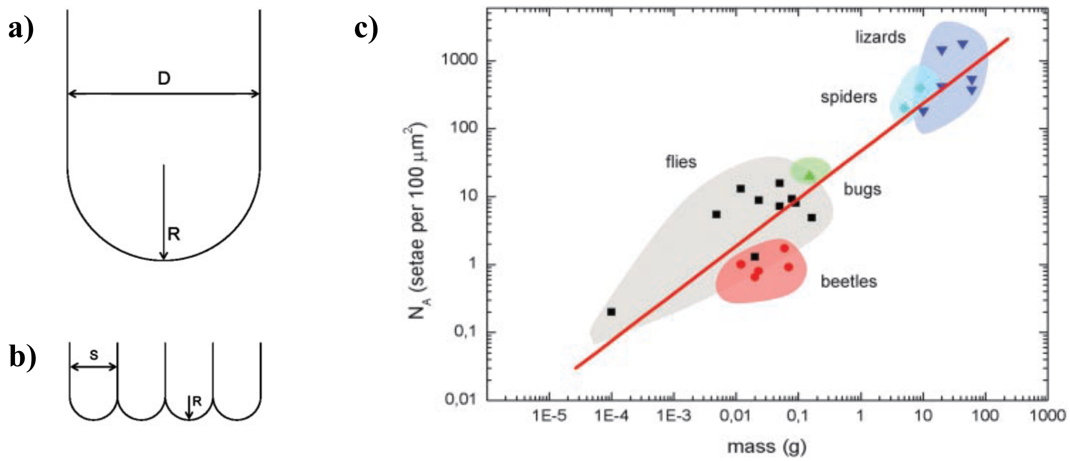

Figure 2.8: Depiction of the splitting of a single hemispherical contact structure (a) into multiple smaller hemispheres (b). The team of Arzt et al. found that, as body mass m increases, the areal density of fibrillar structures N_A increases at a rate proportional to $m^{2/3}$. Courtesy Arzt et al. 2003 [1] ©The National Academy of Sciences 2003.

If we assume that evolution is optimized such that the pull-off force is roughly equal to the body weight of the organism, we see that the surface energy required between toe pad and substrate required to hold an organism decreases at a rate of $1/\sqrt{n}$.

The team further developed this concept to propose a scaling law relating body mass to the areal density of fibrils. Take D to represent some linear dimension of a toe pad. Because mass scales with volume, we can say that

$$m = D^3 \rho p \tag{2.3}$$

where ρ represents density and p is a non-dimensional shape factor. Again, if we assume that evolutionary goal is to support body weight, the desired pull-off force is

$$F_c = mgk \tag{2.4}$$

with g representing the acceleration due to gravity and k a non-dimensional factor of safety. If we now assume that the toe pad of diameter D is split into n hemispheres of radius s, we can express the areal density as

$$N_A = \frac{n}{D^2} = \frac{1}{s^2} \tag{2.5}$$

The JKR pull-off force for the n hemispheres is

$$F_c = n\frac{3}{2}\pi\frac{s}{2}\gamma = \frac{3}{4}\pi D^2\gamma\sqrt{N_A} \tag{2.6}$$

Solving for N_A, we are left with the relation

$$N_A \propto m^{2/3} \tag{2.7}$$

Figure 2.8c depicts the $m^{2/3}$ fitting for various different families of animals. There are certainly shortfalls with this theory, most notably that it implies infinite enhancement with increasingly smaller fibrils, yet the gecko is the most massive animal documented to use these structures. Likely there is a mechanical limit beyond which fibrils could not bear the tensile stress of adhesion. However, it provides a strong mechanistic explanation for adhesion enhancement through fibrillar structures.

2.3.3 Directional Compliance

As stated before, many biological attachment structures display high degrees of compliance in the normal direction despite having very rigid keratinous or chitinous terminal structures. Macroscopically, this serves to maximize contact area and minimize flaw sensitivity. However, new research suggests that the microscopic aspect of compliance may contribute more significantly to adhesion enhancement. To explain this phenomenon, the team of Bartlett et al. [11] began by approaching adherence as an energy balance. For the contact of any arbitrary geometry, the total energy U_T will have three components: the surface energy U_S, stored elastic energy due to the deformation of the bodies U_E and energy due to the applied load U_W. In a state of equilibrium, the energies will balance such that

$$\frac{\partial U_T}{\partial A} = \frac{\partial U_S}{\partial A} + \frac{\partial U_E}{\partial A} + \frac{\partial U_W}{\partial A} = 0 \tag{2.8}$$

Moreover, for a system designed for adhesion, it is assumed that any change in elastic energy will be countered by a subsequent change in surface energy through the forming or breaking of surface

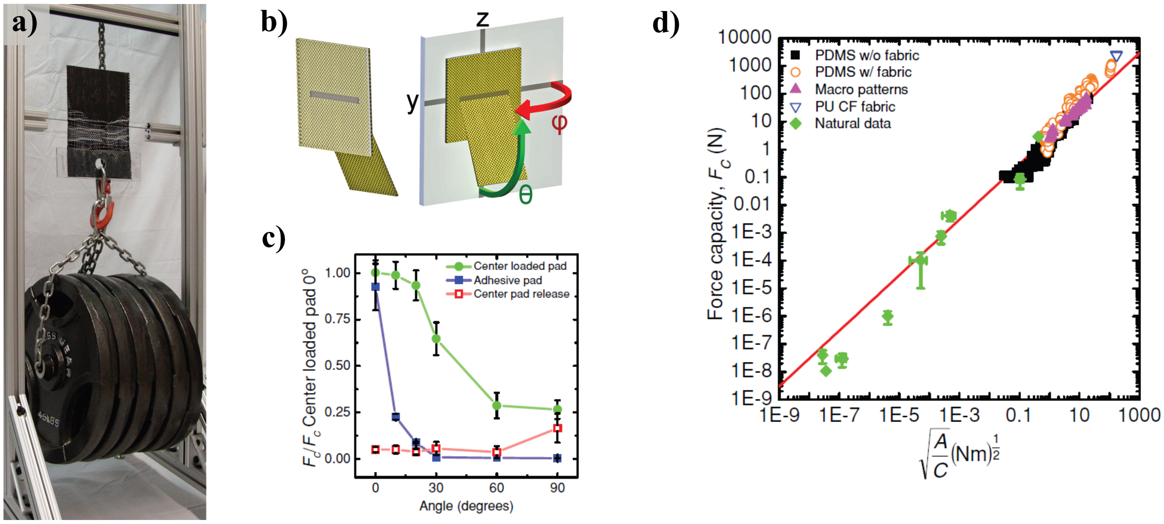

Figure 2.9: (a) Using selective compliance, the team of Bartlett et al. were able to suspend 135 kg using a 100 cm^2 pad of PU backed with Carbon Fiber. (b) Schematic of a center-loaded adhesive pad, which the team found to show good directionality as evidenced in (c): peeling from the center (green) was more angle tolerant than from the edge (blue), while peeling orthogonal to the loading direction (red) showed no tolerance. (d) The scaling law developed by the team showed good agreement for both engineered surfaces (black, orange, purple, and blue) and natural fibrillar structures (green) for flies, spiders, beetles, and geckos. Courtesy Bartlett et al. 2002 [11] ©WILEY-VCH Verlag GmbH & Co. 2012.

contacts such that

$$\frac{\partial U_S}{\partial A} = -\frac{\partial U_E}{\partial A} = G_C \tag{2.9}$$

with G_C representing, essentially, the work of adhesion between the two surfaces. If we assume the material to exhibit linear compliance, we can relate elastic energy to applied load and compliance as

$$U_E \propto F^2 C \tag{2.10}$$

with C representing the compliance of the system. Thus, we can say that

$$F_C \propto \sqrt{G_C}\sqrt{\frac{A}{C}} \tag{2.11}$$

Because G_C is a surface property and not easily manipulated, adhesion optimization is accomplished by tuning the ratio of contact area A and compliance C. It is important to note that this ratio is directional - it need not be the same in the shear and normal direction. In fact, natural fibrillar structures capitalize on this directionality: fibrils offer maximal compliance in the normal direction by bending, while this bending serves to align the fibrils in such a way as to minimize compliance in the shear direction. This creates maximum adhesion for locomotion, while still allowing for fast and facile disconnection when peeled in the normal direction. This relationship also highlights the shortcomings of most engineered dry adhesives: soft materials offer maximum contact area but very high compliance, while stiff materials minimize compliance but suffer from low contact area, particularly on rough or irregular surfaces. The team set out to overcome this by combining thin elastomeric sheets (Polyurethane(PU) and PDMS) backed by inextensible fabric sheets (cotton fabric and carbon fiber). The fabric sheets offered minimal to no extension in the shear direction while still bending easily, thus maintaining high compliance in the normal direction. The A/C ratio was tuned by altering the thickness of the compliant layer, the contact area, and the backing material. With a PU and Carbon Fiber pad, the team was able to suspend a load of 135 kg with a contact area of 100 cm^2 (Figure 2.9a). Moreover, they found that their scaling law applied to both their engineered adhesives as well as fibrillar biological structures (Figure 2.9d).

2.4 Research Aims

This chapter has presented several examples of biological adhesive structures, showing adaptations to maximize friction, as well as wet and dry adhesion, as well as attempts to better understand the mechanisms underlying these phenomena through either experimentation or by developing biomimetic surfaces. Although many advances have been made, engineered surfaces still fall well short of their biological exemplars. Millenia of evolutionary pressure, along with the ability to “build” structures at cellular resolution, likely means biomimetics will always be outpaced. However, advancements in science still continue to improve the ability to tune adhesion, making biomimetic adhesives relevant to ever-increasing applications.

Although most of the studies presented thus far have dealt with soft engineered surfaces (with or without microstructure) contacting rigid substrates, our research group seeks to flip that paradigm. In the field of medical robotics, it is often the case that the relevant contact involves elastomers (e.g. PDMS) encountering tissue which is orders of magnitude softer. By better understanding the interaction between elastomers and soft tissue, we can develop models that will help develop engineered surfaces to tune adhesion and friction so as to optimize the design of medical devices, to include robotic endoscopes (Figure 2.10a), stents, endoscopy balloons (Figure 2.10b), and adhesive bandages.

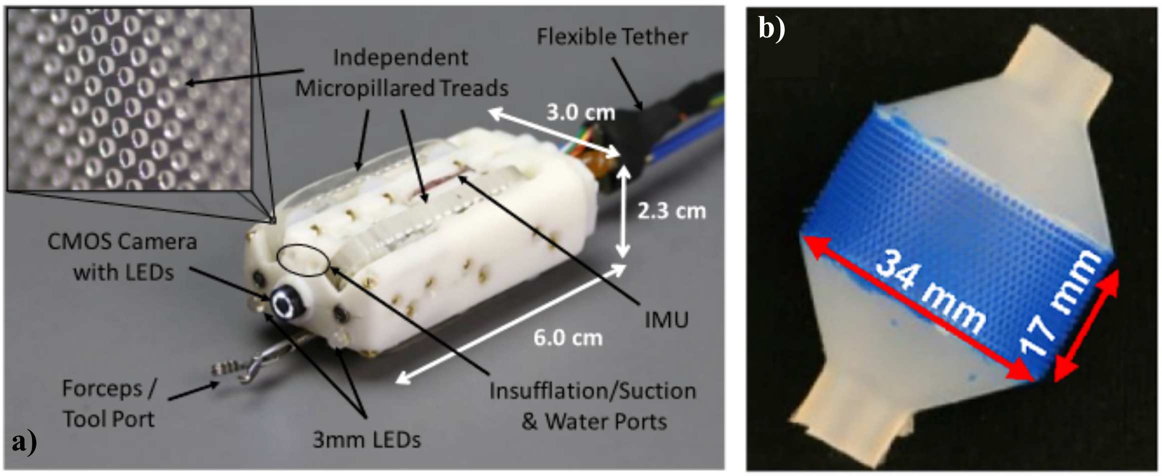

Figure 2.10: Two examples from our research group of medical devices incorporating a micropillared surface to better tune adhesive properties. (a) A Robotic Capsule Endoscope (RCE) uses micropillared treads to be better navigate the highly deformable and mucus-coated intestinal lumen - courtesy Formosa et al. 2020 [25] ©IEEE 2019. (b) an endoscopic balloon incorporating micropillars was shown to better adhere to the intestinal lumen than currently available smooth latex balloons - courtesy Bowen et al. 2020 [14] ©Elsevier Ltd. 2020.

For my part, I will investigate this interaction in terms of rolling contact. As will be explained in subsequent chapters, rolling contact provides a means of investigating the adhesive properties of highly deformable materials while avoiding shortcomings of more traditional peel or indentation tests. Through these tests, I hope to develop a numerical model for the interaction of micropillared elastomers with soft tissue, and to develop pillars with novel shapes in an attempt to display directional anisotropy. As such, my Research Aims are as follows:

(1) Design, build, and validate a tribometer capable of measuring relevant contact metrics (normal and tractive force, contact width) for the interaction of soft elastomers and engineered

surfaces.

(2) Develop a Predictive Model for the rolling contact of soft elastomers on engineered surfaces.

(3) Develop engineered surfaces with tuneable adhesive characteristics through rapid production (3D Printing and/or laser cutting) techniques.

Chapter 3

A Tribometric Device for Rolling Contact of Soft Elastomers[1]

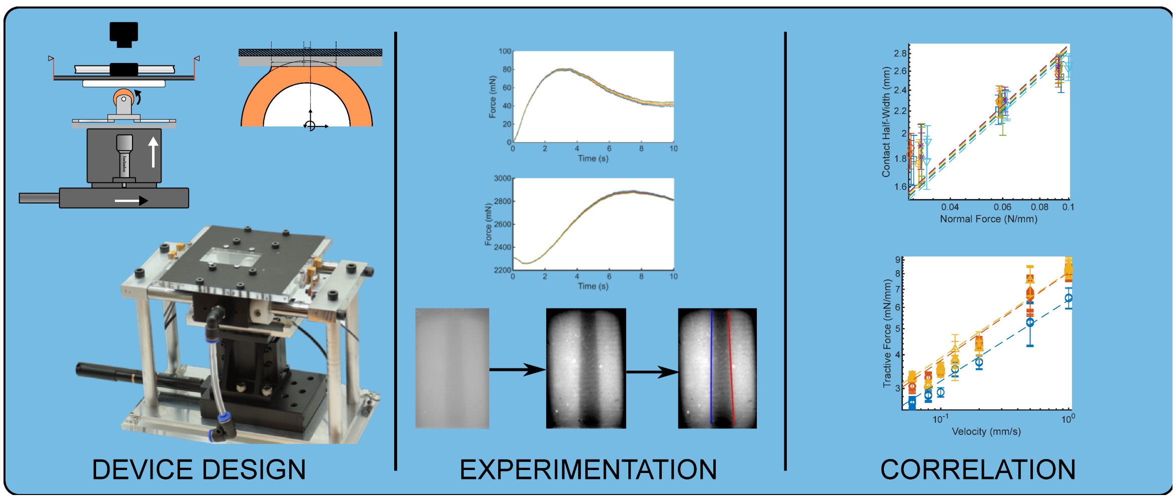

3.1 Introduction

With roots dating back over a century, contact mechanics remains a dynamic field of study with practical and theoretical relevance to myriad engineering applications. As modern contact theories more effectively incorporate complex surface geometries, interactions, and material properties, they are better able to predict and explain interactions ranging from nano- to macroscopic length scales. This predictive ability has been applied successfully to modeling and design efforts in fields as disparate as biological locomotion [1], micro-electromechancial systems [90], medical robotics [78], and automotive design [81].

[1] The results presented in this chapter are reported in the journal Tribology Letters: Hoyer BK, Long R, Rentschler ME. A Tribometric Device for Rolling Contact of Soft Elastomers. Tribology Letters, 2021.

The modern treatment of contact mechanics began with Hertz' analytical solution for the contact of spherical bodies [41]. Building upon Hertz theory, several independent contact theories were developed to incorporate adhesion [22, 49, 27, 9]. The theory of Johnson, Kendall, and Roberts captures the effect of adhesion by following a fracture mechanics approach and gained further relevance with the application of cohesive zone models [6, 23, 7, 67, 45] which regulate the stress singularity at the contact edge, making adhesion computationally tractable for finite element methods and opening the field to the investigation of almost any arbitrary geometry.

Recent advancements in adhesive contact theories have focused on surface texture and novel materials. Surface texture, in most general terms, includes inherent roughness [68, 91, 69, 70, 81] and engineered surfaces [66, 5, 47]. Regarding the materials, recent interests in friction, wear, and adhesion of materials with moduli in the sub- to single-MPa range has led to an emerging field known as soft tribology [71]. In addition to large deformation, these materials also tend to show high rate-dependency, either through visco- or poroelasticity, and may respond differently to surface texture due to their inherent deformability. Because of their relevance to biological tissue, advances in soft tribology can contribute to advances in the design of medical robotics, reversible adhesives for bandages and wearable devices, and soft grippers.

Soft materials pose several challenges for investigations on frictional or adhesive contact. In the case of indentation experiments, the high deformability of soft materials implies that material or geometrical nonlinearity may prevail even under relatively low force, which is beyond the regime of applicability of analytical contact theories. In the case of peel experiments, soft materials are often difficult to be gripped firmly and often must be affixed to an inextensible backing layer to ensure the measured extension reflects only the interface crack progression and not the stretch of the material itself.

A particularly relevant contact mode in medical robotics is rolling contact [78, 89] (Figure 3.1b), in which a cylindrical roller is brought into contact with a deformable substrate and translated across, either by means of a tangential drawbar force or imposed torque. If the indenter and substrate are stiff, it is sufficient to describe the kinetics of rolling in terms of a frictional force imposed at a small contact area or even a point. In soft materials, however, adhesion contributes significantly to both contact area and forces. By measuring the forces and contact area during rolling contact, the adhesive properties of surfaces can thus be characterized. In particular, Kendall's rolling contact theory suggests that the separation of surfaces at the trailing edge of contact is analogous to a peel experiment [52]. In this way, rolling contact experiments provide many advantages over peel experiments in that the soft material can be affixed to either the roller or base to prevent extension, preload force or displacement can be easily controlled, and imaging of the contact area is comparatively simple provided that one material is optically clear or translucent. Additionally, in the case of engineered surfaces, rolling contact experiments allow the study of surfaces with directional anisotropy that would be indistinguishable in indentation and retraction experiments [64].

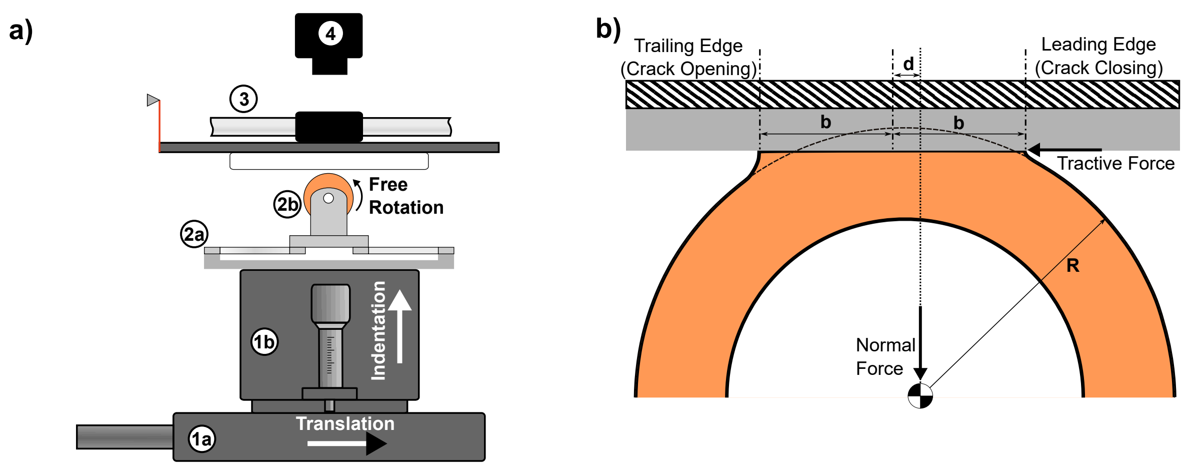

Figure 3.1: Schematic representations of **(a)** the tribometer and **(b)** adhesive rolling contact. **(a)** The functional subsystems of the tribometer include: positioning control (1) comprised of a velocity controlled horizontal stage (1a) and fixed indentation vertical stage (1b), normal force sensing (2a) and free rolling indenter (2b), frictionless stage (3) for the substrate mount and tangential force sensing, and camera (4). **(b)** In adhesive rolling contact, the leading and trailing edges of contact act as crack fronts. Because the work of adhesion is typically higher for separation, the contact area is pulled towards the trailing edge by distance d. Rolling contact geometry is defined in terms of the indenter radius R, contact half-width b, and off-center distance d

Foundational studies on soft rolling contact focused on soft-to-rigid contact, with either a rigid cylinder rolling on a rubber surface [16] or a rubber-coated cylinder rolling on a rigid surface

[28]. Recently, tribometric studies have been conducted for rolling of a periodically-structured indenter on a rigid surface [86] as well as a micropatterned wheel with imposed slip rate rolling on a viscoelastic substrate [78]. In this work, we have chosen to investigate the rolling contact of a finite-thickness, highly deformable, and rate-dependent elastomer. To do so, we designed and built a benchtop tribometric device (Figure 3.1a and Figure 3.2) capable of collecting relevant forces and contact area images in real time, and validated that device against comparatively rate-independent elastomer such that the results could be compared with analytical solutions. Section 3.2 presents a brief theoretical background for adhesive rolling contact mechanics. Section 3.3 details design of the device and experimental test setup. Section 3.4 presents results from the two experimental test configurations. Finally, the conclusions of this work are presented in Section 3.5.

3.2 Theory

As stated in the introduction, formalized contact theory begins with Hertz, who observed that when two elliptical bodies (i.e., smooth bodies whose surface profiles could be described analytically as ellipses with two characteristic axes) were brought into contact, a finite and similarly elliptical contact area was formed [48]. Under the simplifying assumptions that the contact area was significantly smaller than the characteristic lengths of the bodies, that no adhesion was present between the bodies, and that the surface interface was frictionless, Hertz developed an analytical solution relating surface tractions and stress distributions to the imposed deformations, ultimately relating compressive force to the dimensions of the contact area. The geometric case of Hertz theory relevant to rolling contact is that of cylindrical contact, in which one principal curvature of each body is zero. This is achieved practically by compressing two cylinders aligned axially or compressing a cylinder against a flat substrate. The subsequent Hertz relationship for this type of contact is [48]

$$P = \frac{\pi E^* b^2}{4R}, \tag{3.1}$$

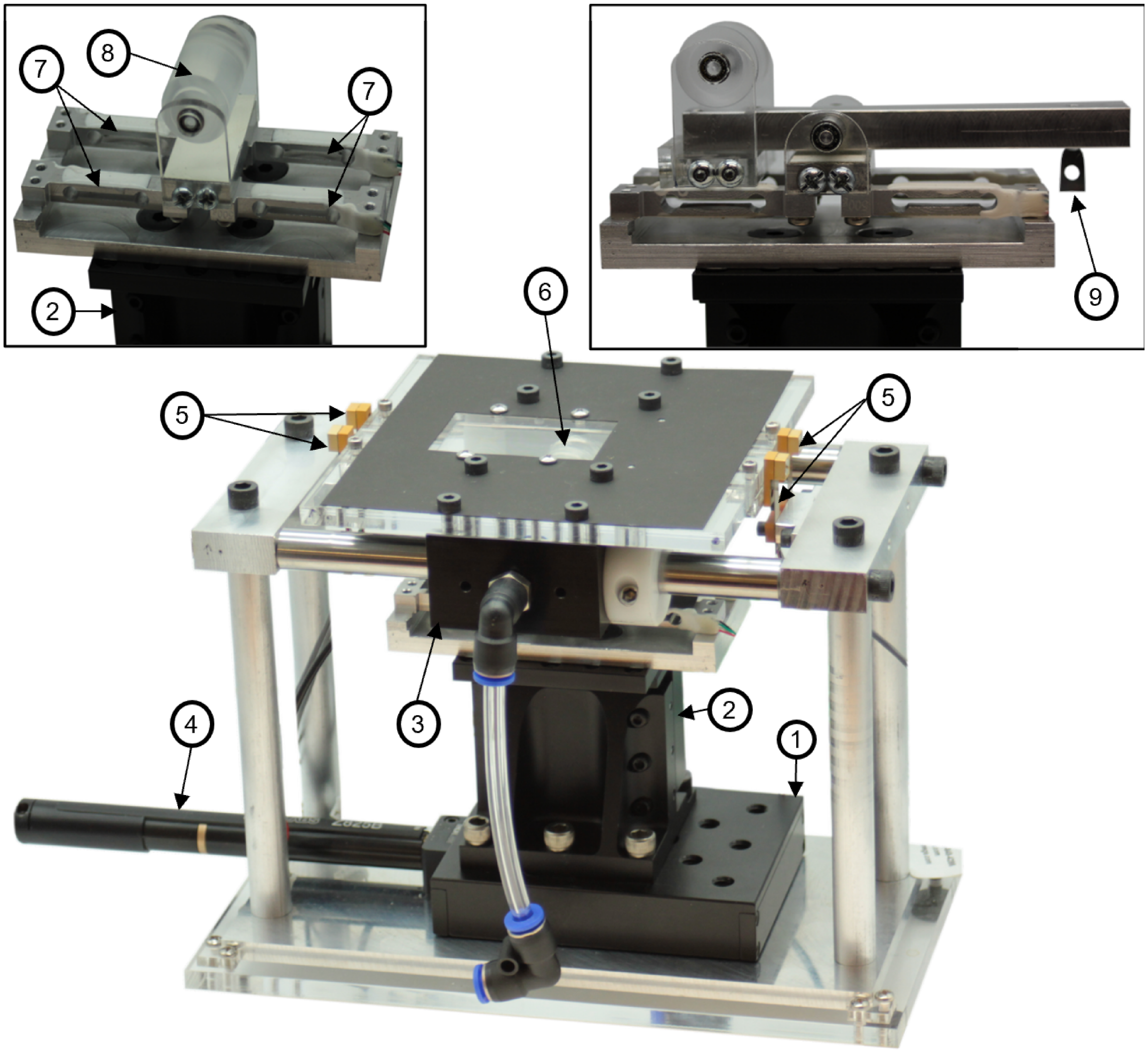

Figure 3.2: As-built picture of the tribometer with major components **(1)** horizontal stage, **(2)** vertical stage, **(3)** frictionless air bearings, **(4)** Motor and lead screw, **(5)** tangential force load cells, **(6)** substrate mount, and **(Inset Left)** normal force plate with **(7)** normal force load cells and **(8)** rolling indenter. **(Inset Right)** Rolling indenter configured for Force-Control Experiments, in which the normal force is set via a counterweight at **(9)**.

in which P represents the normal load per unit length, b is the contact half-width, R is the radius of the cylinder, and E^* represents the plane-strain modulus $E^* = E/(1 - \nu^2)$, with E and ν representing Young's Modulus and Poisson's ratio respectively.

Because Hertz Theory assumes only compressive tractions within the contact area, it tends to underestimate the observed contact length for a given compressive force, and is unable to account for the pull-off force due to adhesion. To account for adhesion, Johnson, Kendall, and Roberts (JKR) developed a contact theory in which attractive tensile tractions cause additional surface deformation, extending the contact length [49]. JKR uses an adhesive contact solution based on the minimization of total energy comprised of elastic energy due to material deformation and surface energy due to adhesion. The relevant JKR relationship for cylindrical contact is [8, 18]

$$P = \frac{\pi E^* b^2}{4R} - \sqrt{2\pi E^* b w}, \tag{3.2}$$

with w representing either the work of adhesion for bodies being brought into contact or work of separation for bodies being separated.

The equations developed above are based on indentation and retraction, with contact characterized by two crack fronts, equidistant from the center of the indenter, opening or closing with equal work of adhesion. Rolling contact, by constrast, involves a crack closing at the leading edge of contact and a crack opening at the trailing edge (Figure 3.1b). Because the work of adhesion during separation is typically much larger than for indentation in most materials [17, 76], the contact area will tend to lengthen towards the trailing edge and shorten at the leading edge. For such asymmetric contact, the normal surface traction within the contact area is [16]

$$\sigma(r) = \frac{-P/\pi + (E^*/2R)(r^2 - rd - b^2/2)}{(b^2 - r^2)^{1/2}}, \tag{3.3}$$

with d representing tangential distance from the center of the indenter to the center of the contact area (Figure 3.1b) and r representing the distance of a point from the center of contact. Because the work of adhesion and separation are not equal, the crack tips must be evaluated independently. Using the leading edge of contact as an example, it is necessary to first solve for the Mode-I stress intensity factor [76]

$$K_{I,lead} = \lim_{r \to b} \sigma(r)[2\pi(b - r)]^{1/2}. \tag{3.4}$$

Because the crack tip is in equilibrium, the stress intensity factor can be related to the strain energy release rate G and work of adhesion as

$$w_{adh} = G = K_{I,lead}^2 / 2E^*. \tag{3.5}$$

By solving the two equations above and relating the the torque on the indenter to the contact asymmetry through the integral of the surface traction, the resulting relationship is [76, 75]

$$P = \frac{\pi E^* b^2}{4R} - \sqrt{2\pi E^* b w_{adh}} - \frac{\pi E^* b d}{2R}. \tag{3.6}$$

In a similar fashion, the work of separation at the trail edge is equal to

$$P = \frac{\pi E^* b^2}{4R} - \sqrt{2\pi E^* b w_{sep}} + \frac{\pi E^* b d}{2R}. \tag{3.7}$$

Additionally, by considering the equilibrium of forces acting on the indenter, a relation between the external forces and characteristic lengths of contact can be derived [16]:

$$P = \frac{\pi E^* b^2}{4R} - \frac{FR}{d} \tag{3.8}$$

with F representing the tractive force on the indenter. Using Equations 3.6, 3.7, and 3.8, we can derive an expression for the difference between the work of separation and work of adhesion:

$$w_{sep} - w_{adh} = F \tag{3.9}$$

which is in agreement with Kendall's theory [52]. It is important to note that in the theoretical treatments of rolling contact referenced here, it is assumed that the surface traction in the contact region remains strictly normal to the interface. That is, the interface is assumed to be frictionless, and the kinetics of rolling contact are driven solely by the disparity in adhesive energies between the leading and trailing edge crack fronts.

3.3 Material and Methods

3.3.1 Tribometer Design

This section will outline the key physical and electrical systems of the tribometer, as well as data synchronization, collection, and processing.

Motion Control

The tribometer (shown schematically in Figure 1a and as-built in Figure 2) is a 3-Degree-of-Freedom (DOF) system: indentation of the indenter normal to the substrate, translation of the indenter along the substrate, and the unconstrained rotation of the rolling indenter. Constant vertical displacement (indentation) is achieved with a vertical positioning stage (THORLABS MVS-005) actuated via a dial micrometer with 0.001" gradation. Horizontal translation takes place via a sliding stage (THORLABS PT101) actuated by a DC Servo Motor and lead screw combination (THORLABS PT1-Z8R). The translational velocity is PID-controlled using a motor controller (THORLABS KDC101), with the velocity set by the user via a MATLAB Graphical User Interface (GUI). The combination of the lead screw, motor, and gearhead allows for selection of velocities ranging from 0.005 to 2 mm/s. The horizontal translation stage has a maximum range of 25.4 mm; using the outer diameter of the indenters used in both test cases (19.0 mm), this allows for maximum rotation of almost one-half of a revolution (0.85π radians).

Normal Force Sensing and Rolling Indenter

A primary consideration for the design of the device was the geometry of the indenter - whether to use a spherical or cylindrical roller. Rolling sphere on rolling disk indenter tribometers [13, 19] offer several advantages, specifically that a spherical roller is inherently self-aligning and that the rotating disk allows infinite translation. Considering the theoretical treatment, however, the rolling contact of a sphere is inherently a 3-dimensional problem as the curvature of the sphere along the axis of rotation must be considered. Because the rolling contact of a cylinder can be reduced to two dimensions, the analysis is greatly simplified. For this reason, we chose to use a cylindrical roller.

The rolling indenter housing can be easily modified to accommodate either indentation control or force control experiments. In the case of indentation control (Figure 3.2, left inset), the roller is positioned at a fixed vertical height above the translational stage. The depth of indentation is set by vertical stage micrometer and remains fixed throughout the experiment. For force control (Figure 3.2, right inset), the indenter housing occupies one end of a fulcrum, and the normal force applied to the interface is controlled by means of a counterweight applied to the opposing end.

For both configurations, the rolling indenter housing sits atop four 500 g Load Cells (Sparkfun TAL221). The displacement of the four load cells is coupled by a rigid aluminum plate, which also serves as a mounting platform for the rolling indenter. Because the indenter/substrate interface is positioned vertically above the load cells, the resulting moment must be considered. For indentation control, the moment creates equal and opposite reaction forces in the horizontally opposed pairs of load cells. The opposing force signals then cancel each other out in the summing junction described below. For force control, the mass and dimensions of all components of the fulcrum system are known, allowing the tractive moment to be factored into the sum of forces and moments when caclulating the normal force. The current device configuration can accommodate indenters up to 35 mm in length and 25 mm in diameter.

Using a numerical simulation of the load cell geometry with a linear elastic Aluminum material model (E=69 GPa, ν=0.34), we determined that the four load cells combined provided a normal stiffness of 117.3 N/mm. To compare this to the experimental materials used, we used a 2D plane-strain numerical model of the indenter geometry for both experimental configurations, with the respective elastomers modeled as hyperelastic and non-compressible. For the Rigid/PDMS configuration, we found that the contact stiffness approaches 105 N/mm at the highest compressive loads (200 gf or 1.96 N). For the PVC at the deepest indentation, the contact stiffness is much reduced, reaching only 4.60 N/mm.

Force Isolation and Tangential Force Sensing

A key design consideration for this system was the elimination of spurious strains in the tangential load cells due to axial loading from the normal force. To achieve this end, the substrate is affixed below a rigid acrylic plate which travels on two horizontal rails by means of frictionless air bearings (NewWay S301201). The air bearings serve two purposes: they prevent the transfer of normal loads to the tangential load cells and eliminate friction which would negatively impact the tractive force readings.

There are four thin-beam load cells (Omega LCL-113G, 100 g capacity) affixed to the sliding plate assembly, two on each side. The opposing ends of the load cells are affixed rigidly to the tribometer frame. Thus, any tangential translation of the sliding plate is conferred to bending moments in the load cells, correlating to tangential force on the substrate.

Modeling the thin beam load cells using beam elements with a linear elastic beryllium copper material model (E=125 GPa, ν=0.3), we determined that the combined lateral stiffness from all four load cells was approximately 17.7 N/mm. Our numerical simulation of the PVC indicates a lateral stiffness contact stiffness of 0.1 N/mm.

Contact Area Imaging

A key characteristic of adhesive cylindrical contact is the width of the contact area formed between the two solids. An HD camera (ArduCam B0280, 12MP) is mounted above the substrate window to collect real-time images of the contact for each experiment.

As stated above, a challenge in cylindrical contact experiments is maintaining consistent axial alignment between indenter and substrate. Although somewhat negated when dealing with soft materials, this still must be considered. Each of the pillars supporting the sliding plate assembly can be height adjusted slightly relative to each other, allowing some degree of alignment. Even so, the use of soft elastomers for both substrate and indenter lead to some unavoidable irregularities. To account for this, a mean contact width was calculated for each captured frame.

Data Collection and Synchronization

The load cell signal processing flow described in this paragraph (shown schematically in Figure 3.3a) is identical for both directions, normal and tangential. Unless stated specifically, the following description applies to both channels. From the measurement base, each of the four load cells emits a voltage signal proportional to the strain to which it is subjected. These four signals are then combined through a passive averaging circuit in a junction box (ANYLOAD J04-SA). The output signal from the junction box, still in the millivolt range, passes to a Signal Conditioner/Amplifier (Tacuna Systems EMBSGB200) with a two-stage low-pass filter and selectable gain amplifier. The amplified signal is then passed to a DAQ (National Instruments myDAQ). Each DAQ Channel has 16-bit resolution, resulting in maximum force resolution of 0.78 mN for normal force and 0.027 mN for tangential force (based on load cell signal range and amplification).

Overall data collection and synchronization is conducted by a MATLAB script. Based on user inputs regarding test velocity and direction of travel, test length, and number of test iterations, the MATLAB script will run the test protocol and collect the data. The data collected for each test iteration includes the time and channel voltages from the DAQ, which are subsequently converted to force measurements, video and timestamps for each frame capture from the camera, and position data from the motor controller.

3.3.2 Data Processing

For each test iteration, the normal and tractive data is smoothed using a moving mean filter with a window equivalent to 0.05 seconds. The data is then truncated to represent only the equilibrium portion of the rolling contact. Based on experimental observation, and to remain consistent, this is defined as the range 60-95% of overall execution time. From this data, mean values of tractive and normal forces are calculated.

Next, a representative sample of video frames captured during the equilibrium time bounds are randomly selected to be processed. Each frame is flattened based on calibration data specific to

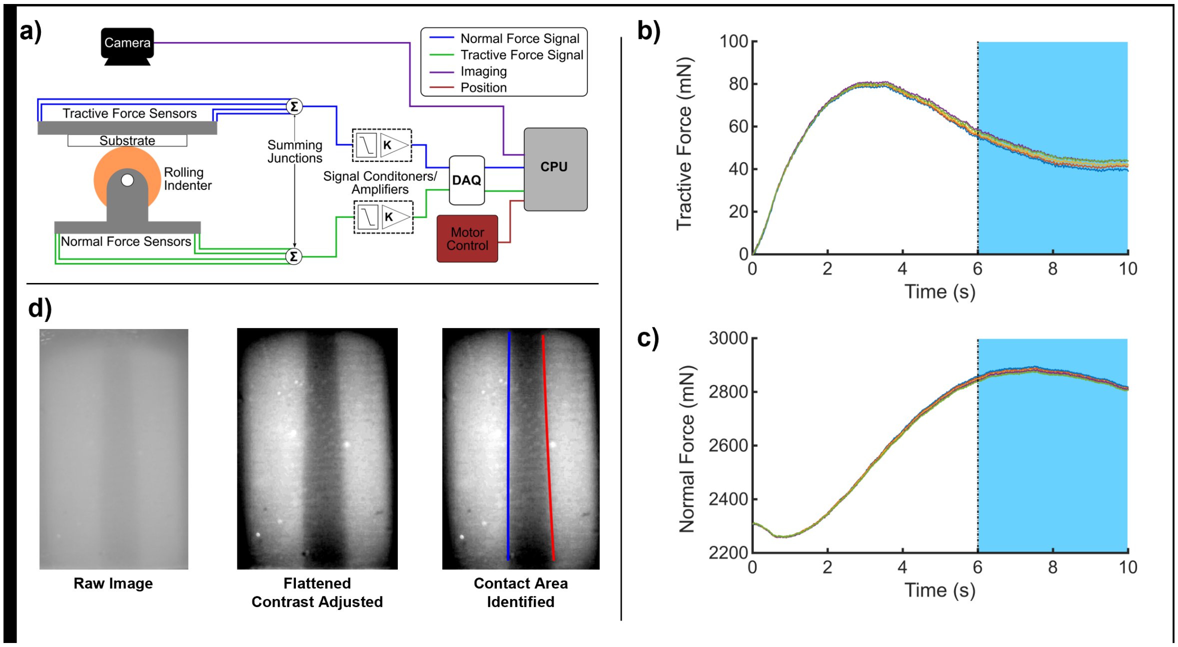

Figure 3.3: **(a)** Schematic of the data flow for the tribometer: for each force direction, voltage data from four load cells is combined in a summing junction and the single signal is filtered and amplified before passing to the DAQ. The digital signal is then converted to a force and stored via a MATLAB GUI. Examples of filtered data for multiple test iterations of a nominal indentation depth and translational velocity: **(b)** tractive force and **(c)** normal force. **(d)** Images of the contact area workflow: raw images are flattened and contrast-adjusted to heighten the contact area, and the lead and trail edges are delineated in order to determine the mean contact width.

the camera, lens, camera resolution and zoom, and contrast adjusted to accentuate the limits of the contact area (Figure 3.3d). The lead and trail edges are then identified and a mean contact width is measured. The associated timestamp of the frame capture is used to determine the indenter's center of rotation, as well as the instantaneous normal and tractive forces corresponding to the contact width.

3.3.3 Experimental Test Cases

We conducted two separate experiments. The first, intended for device validation, involved a rigid acrylic indenter rolling along a flat, comparatively rigid elastomer substrate, which could be readily compared to JKR contact theories and experimental results from previous studies. The second, designed for testing the contact with tissue-like materials, used an indenter comprised of a thin shell of a highly-deformable, viscoelastic elastomer affixed to a rigid core rolling along the same substrate.

Device Validation

When dealing with highly deformable materials, there is a potential for interfacial slip, even at low loads. To minimize the likelihood of slip, the device validation test case involved the indentation and rolling of a rigid, nominally-smooth acrylic cylinder, radius 9.5 mm and length 28.6 mm along a nominally flat silicone substrate of polydimethylsiloxane (PDMS) (Dow Corning Sylgard 184 at 10:1 base/curing agent ratio by weight) of dimensions 31.8 mm W x 50.8 mm L x 3.2 mm D. Based on extension tests conducted using an Material Testing System (Instron Corp., Norwood, MA), PDMS can be modeled as an incompressible hyperelastic material with a Young's modulus E of 2.9 MPa. Because of the comparative rigidity of the indenter and substrate, a force-controlled experiment was conducted to minimize the effects of indenter or substrate irregularities. Four normal force values of 3.22, 9.34, 19.54, and 23.62 mN were imposed on the indenter by means of a counterweight. Because the equations by which we were to validate our data are based on the assumption of elastic materials, the validation experiments were conducted quasi-statically, at a translational velocity of 0.06 mm/s. Relevant results from this test case are presented in Figure 3.4.

Tissue-Like Test Case

For the tissue-like test case, the rigid indenter was replaced with an indenter comprised of a rigid acrylic cylindrical core (radius 6 mm) with a 3 mm-thick smooth outer layer of poly(vinyl chloride) (PVC) (M-F Manufacturing Co, Fort Worth, TX), thermally bonded to the acrylic core. PVC was chosen for the deformable shell because it has been used in previous studies as a relevant mimic to biological tissue [78, 54].

Previous studies on PVC determined that it was mildly viscoelastic and could be modeled using a Standard Linear Solid (SLS) material with E_1 = 16.4 kPa, E_2 = 0.467 kPa, and η = 20.3

kPa-s [78, 84]. With E_1 representing the equilibrium arm of the system and E_2 the damped Maxwell arm, this gives an instantaneous modulus of 16.9 kPa and a relaxed modulus of 16.4 kPa, indicating that the PVC is only mildly viscoelastic. Using a PVC outer layer on the rolling indenter provided the opportunity to investigate the effects of both finite-thickness and rate-dependent phenomena. The more rigid material (PDMS) was selected as the substrate because it is optically clear and could be molded to a more reliably flat surface. Because the PVC is highly deformable, a displacement-controlled experiment was used to better control contact width. Three relative indentations[2]of 0.902 mm, 1.02 mm, and 1.12 mm were used. Additionally, the indenter was subjected to a range of translational velocities from 0.06 mm/s to 1.0 mm/s in order to observe rate-dependent effects from the PVC. Relevant results from the this test case are presented in Figure 3.6.

3.4 Results and Discussion

3.4.1 Device Validation

The analytical solutions outlined in Section 3.2 are based on the assumption that surface tractions are only in the normal direction, negating interfacial friction. Because eliminating friction via material selection was unlikely in the case of elastomers and the addition of a lubricant would affect the surface interaction between substrate and indenter, we chose materials such that the elastic and adhesive energies would be larger than the dissipation due to friction.

Using the measured values of normal force P (N/mm), contact half-width b (mm), and contact asymmetry d (mm), along with a Young's modulus of 2.9 MPa and a Poisson's ratio of 0.5, the expected values for work of adhesion and work of separation were calculated using Equations 3.6 and 3.7 respectively. The difference between the values was compared to the measured tractive force as per Equation 3.9. The results are shown in Figure 3.4a, with the blue circles representing the measured values of tractive force and purple triangles representing the theoretical values. The blue dashed line and shaded area represent the mean and standard deviation of the measured

[2] Because of the difficulty of establishing a zero point of indentation for adhesive cylindrical contact, values are relative to a zero point at which a defined contact area was no longer observed across the extent of the indenter.

tractive force. Both the experimental and measured values agree, within an order of magnitude, to those observed by Barquins and Charmet at similar velocities [16]. It is also notable that both the measured value of tractive force and analytical value of the difference between the work of separation and adhesion, remain independent of the normal force as would be expected if adhesion were the relevant predictor of contact forces. Contrary to predicted adhesive behavior, it appears that the works of separation and adhesion increase with additional normal force. We believe this is because the indenter, although nominally smooth, is not perfectly smooth. Using a confocal laser profilometer, we determined that the surface of the indenter profiles with mean and maximum height of 0.2 μm and 1.5 μm along an axial path and 0.15 μm and 0.82 μm radially around its circumference. In accordance with Persson's theories of rough contact [70, 81, 69], surface roughness creates a disparity between the real and apparent contact areas because surfaces initially contact only at asperities. As normal force increases, so also does the real contact area, affecting the works of separation and adhesion. Because this affects both the work of separation and adhesion, the difference between the two is unaffected.

To validate the normal force measurements, the measured tractive force F (N/mm), contact half-width b (mm), and contact asymmetry d (mm), along with Young's modulus and Poisson's ratio from above, were used in Equation 3.8 to calculate the expected normal force. The results, shown in Figure 3.4b, show good agreement between experimental and theoretical values. The Hertzian component of normal force, that which would be expected in the absence of adhesion, is also shown (yellow squares) to highlight the prevalence of adhesion between the indenter and substrate. In particular, the Hertz contact force (i.e., adhesionless) required to achieve a given contact half-width is much larger than the measured normal force, thereby highlighting the the strong effects of adhesion in our experimental system.

3.4.2 Tissue-Like Elastomer

The first observed difference between the validation case and the tissue-like PVC is the relation between normal force and contact half-width (Figure 3.6a). In contrast to Fig.4b, with

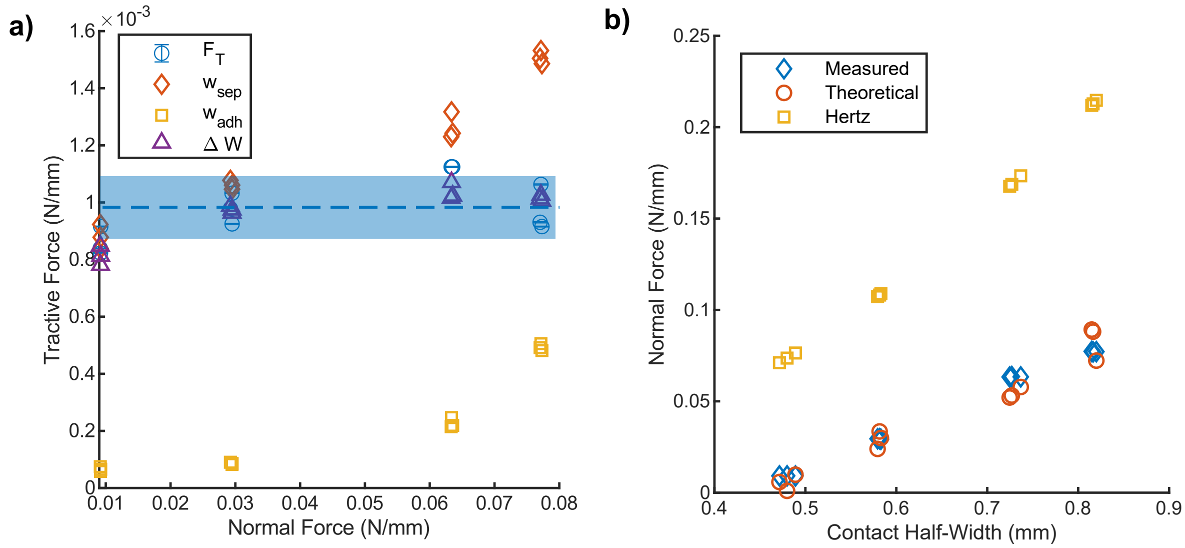

Figure 3.4: Experimental results from the Rigid Acrylic Indenter with PDMS Substrate. (a) tractive force versus normal force: blue circles represent the experimentally measured values, with the blue dashed line and shaded area representing the mean and standard deviation thereof, while purple triangles represent the expected values from Equation 3.9; red diamonds and yellow squares indicate expected values of work of separation and adhesion respectively as per Equations 3.6 and 3.7. Good agreement is found between the measured and theoretical values, and work of separation is consistently higher than work of adhesion, as is predicted. (b) Normal force versus contact width, showing good agreement between measured values (blue diamonds) and theoretical (red circles) as per Equation 3.8. The normal force prediction absent adhesive interactions (Hertzian – yellow squares) is included to highlight the prevalence of adhesive forces in this experimental configuration.

the PVC layer, the normal force required to achieve a given contact half-width is much larger than that predicted by the Hertz solution. This is due to the fact that the PVC is a thin layer (3mm) adhered to a rigid acrylic core. As described by Shull [77] and expounded on in later work for curved spherical shells [54], contact deviates from Hertzian predictions when the relevant contact length grows proportionally closer to the depth of the substrate because the material can no longer be accurately modeled as a half-space, and correction factors must be applied. The experimental results were thus compared to a numerical model. A two-dimensional plane strain model of the indenter and substrate geometries was built using ABAQUS (Dassault Systemes Americas Corp, Waltham, MA), with each material modeled using incompressible, Neo-Hookean hyperelastic materials. The modulus of the PVC was tuned to best match the experimental data resulting in a predicted modulus of 21 kPa, which closely matches the expected value for the material, again considering that the experimental data is taken from the equilibrium rolling portion of the test. A comparison of the Hertz prediction, numerical model, and experimental results is shown in Figure 3.5.

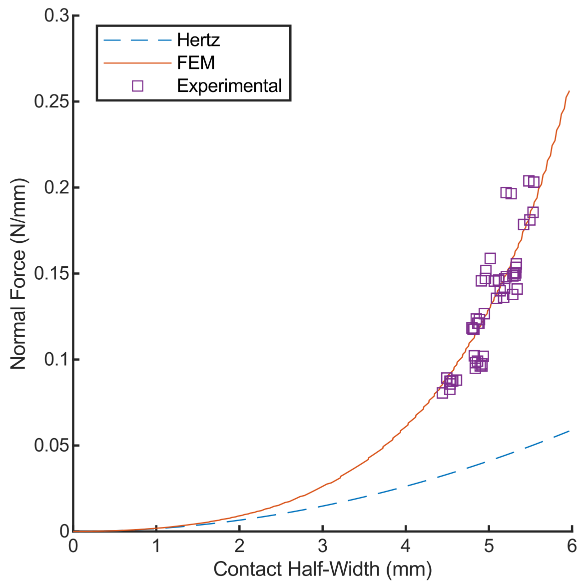

Figure 3.5: A comparison of the relationship between contact half-width and normal force. As shown, when the half-width approaches and exceeds the thickness of the deformable layer on the wheel (3 mm), there is significant deviation from the contact predicted by Hertz (dashed blue line). The FEM simulation results (solid red line) match much more closely to the experimental results (squares).

Because the PVC is mildly viscoelastic, the relations between contact half-width and normal force with relative indentation were affected by translational velocity. Relating normal force P to relative indentation $\hat{\delta}$ (Figure 3.6b), the relational exponents ($P = k\hat{\delta}^n$) ranged from 1.796 to 2.948. The relational exponents for contact half-width b to relative indentation ($b = k\hat{\delta}^n$) were similarly varied (Figure 3.6c), ranging from 0.160 to 0.516. This further illustrates the need to consider both finite-thickness effects and viscoelasticity in similar test configurations.

The intricate coupling between the finite thickness effect and viscoelasticity is further reflected in Figure 3.6d, where the contact width is plotted as a function of the tangential velocity at three different indentation depths. The different scaling exponents between contact width and velocity (i.e., 0.5, 0.4, and 0.2 for shallow, intermediate and deep indentations, respectively) shows that the finite thickness effect can reduce the rate-dependence of contact width by increasing the contact stiffness (Figure 3.5). In contrast, the tractive force exhibits a remarkably consistent scaling relation with the velocity at a mean exponent n of 0.316 +/- 0.01 for all three indentation depths (Figure 3.6e). This is illustrative of the fact that the kinetics of rolling contact are driven primarily by the disparity in surface energies between the leading and trailing edge cracks, quantified by the work of adhesion w_{adh} and separation w_{sep}, both of which are functions of their respective crack tip velocities. Since the data is collected during steady state rolling such that the crack tip velocities match the tangential velocity, it is expected that Kendall's steady state argument still holds, which implies that Equation 3.9 is valid and hence the tractive force, representative of the disparity between the two energies, depends solely on the tangential velocity regardless of the contact width. This feature allows one to decouple the tractive force from the complex contact mechanics and use it as a reliable measurement for the adhesion between the tissue-like material and the PDMS substrate.

3.5 Conclusion

Rolling contact remains an interesting and instructive means of exploring the adhesive interaction of natural and synthetic materials, whether nominally smooth, intrinsically rough, or with engineered features. We have described the design and realization of a 3-DOF rolling contact tribometer and presented the experimental results of two test cases: a validation test case involving a rigid acrylic indenter and rate-independent silicone elastomer (PDMS), and a tissue-mimic case involving a finite-thickness, mildly viscoelastic (PVC) shell indenter rolling across the same PDMS substrate.

The validation test case was chosen since it has been extensively studied in the literature. As a rigid indenter rolling on a smooth elastomeric surface, it presented the simplest means to validate the data output from the device against established contact mechanics theories. The strong correlation between experimental and theoretical values provides confidence in the device itself.

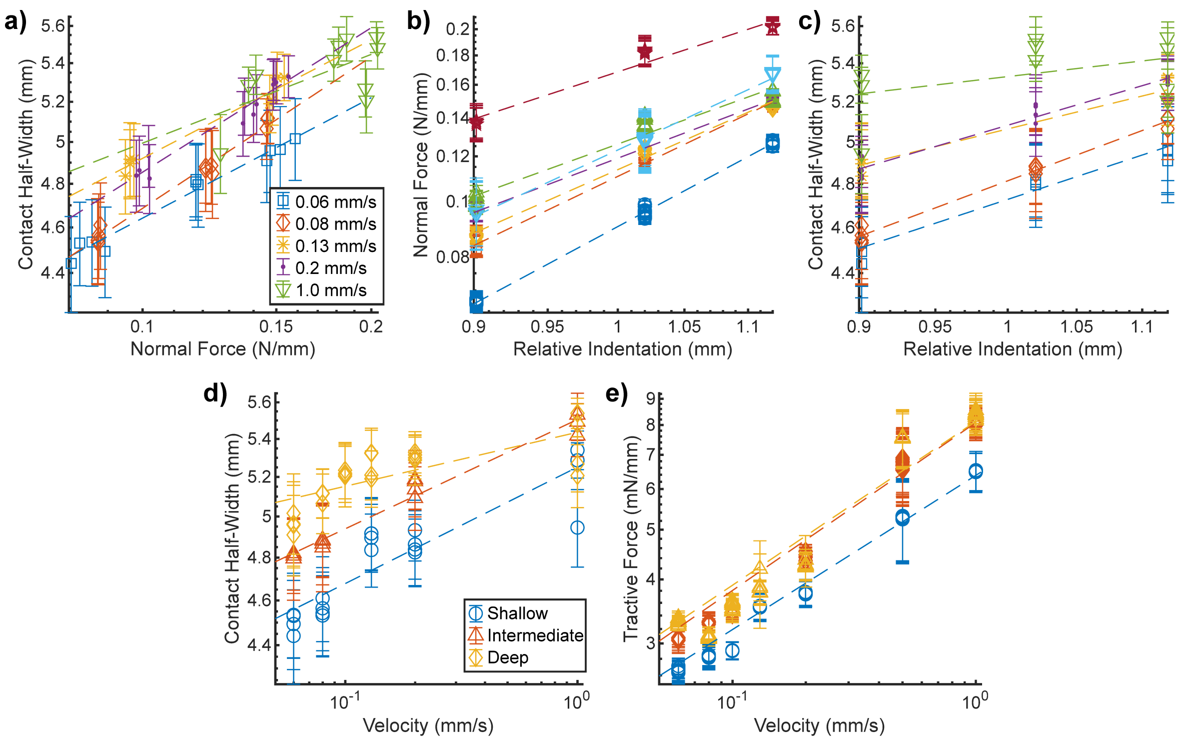

Figure 3.6: Experimental results from PDMS/PVC experiment: **(a)** contact half-width versus normal force; **(b)** normal force versus relative indentation; and **(c)** contact half-width versus relative indentation. Although best fit lines are shown (dashed lines), they were not found to match with conventional contact theories due to the need for finite-thickness correction as the contact half-width approaches the thicknesses for the indenter geometry. The PVC showed substantially more rate-dependence for **(d)** contact half-width, increasing at a power n of 0.4, 0.5, and 0.2 for the shallow, intermediate, and deep indentations respectively; and **(e)** tractive force with a mean power n of 0.316 across all three indentations.

The tissue-like test case, chosen for its novelty, highlights several interrelated aspects of soft tribology. First, the effects of finite-thickness materials was shown through the deviation of compressive behavior from analytical predictions. Second, rate-dependent effects are shown through the reliance of tractive force on crack-tip velocity at the trailing edge. Although no analytical or empirical models are presented, the data can serve as a relevant input for modeling applications involving the adhesion of PDMS with tissue or tissue-like substrates. In particular, our data demonstrate that the tractive force can provide a reliable measurement of the rate-dependent $w_{sep} - w_{adh}$ (or w_{sep} if w_{adh} is much smaller than w_{sep}), despite the intricate viscoelastic contact mechanics involved.

Chapter 4

Characterizing the Rolling Contact between Elastomeric Surfaces and a Soft Synthetic Tissue

4.1 Introduction

The study of adhesion, the interfacial attractive forces between contacting bodies, is a dynamic field of research with a wide range of practical engineering applications. Although the field's analytical roots were established in the 1970s [49, 27, 22], recent decades have seen an abundance of research in applications involving the development of biologically inspired microstructures to effectively tune adhesion [47, 66]. Seeking improved robotic locomotion, researchers drew inspiration from biologically adept climbing insects and lizards, most prominently the gecko, to engineer biomimetic surface structures of diverse geometries to tune adhesive properties [3, 4, 2, 10, 36, 29]. A robust body of research exists to describe the underlying phenomena contributing to adhesion enhancement via microstructures, notably flaw insensitivity [44, 80], contact splitting [1, 51], crack trapping [32, 86], and directional compliance [11]. Currently, the preponderance of microstructure studies involve contact between compliant microstructures and nominally rigid substrates.

To widen the field of applicability for microstructured surfaces, we have chosen to reverse the compliance paradigm and study the interaction of elastomeric microstructured surfaces with materials that are roughly two orders of magnitude softer. This line of inquiry is intended to inform designs in two potential research areas: soft robotics and medical devices/robotics. Over the past several decades, advances in the field of soft robotics have enabled engineers to replace rigid, motorized actuators with soft pneumatic or dielectric actuators [55], expanding potential robotic applications in human interaction and delicate task handling. Similarly, miniaturization of sensors, actuators, and electromechanical systems in general has greatly expanded the field of medical robotics and medical devices. By studying the interaction of engineered surfaces with materials of moduli similar to biological tissue, we aim to provide models informative to practitioners in both fields.

The study of soft material interaction presents several challenges. Because of their inherent deformability, the adhesive interaction in the presence of surface roughness or engineered structures may diverge significantly from the extensively studied mechanisms when dealing with rigid substrates. Moreover, high deformability implies that, even under low contact stresses, the contact area will approach the characteristic dimensions of the test geometry, necessitating the use of correction factors to resolve experimental results and analytical predictions. Finally, because the surface interactions are rate-dependent, characterization requires that experiments be conducted across a range of controlled velocities. When investigating the adhesive properties of soft materials, several experimental methods are available. Indentation and retraction tests involving combinations of rigid or soft probes and substrates [54] are straightforward and can be readily adapted to commercially available material testing systems, but lack the ability to investigate structures which may exhibit directional anisotropy [64]. Peel tests are highly directional and can easily demonstrate anisotropy, but are challenging for soft materials in that they are difficult to grip and to achieve preload control, and often require that the soft material be affixed to an inextensible backing layer so that the progression of the crack front can be decoupled from extension of the material. A third alternative is rolling contact, in which an indenter is brought into contact with a substrate under conditions of fixed indentation or fixed force and translated across the substrate. As the indenter rolls, two crack fronts form - an opening crack at the trailing edge of contact and a closing crack at the leading edge. By observing the relevant forces and contact dimensions during contact, deductions about the adhesive properties of the interface can be made [16, 18, 52].

For this study, we used experimental results from a custom-built rolling contact tribometer [43], along with numerical simulation, to develop a predictive model for the rolling contact between poly(dimethylsiloxane) (PDMS) and a soft, tissue-mimicking substrate of poly(vinyl chloride) (PVC), and have extended our method to include both a flat and micropillared PDMS substrate. Section 4.2 provides a brief overview of contact mechanics theory relevant to numerical modeling of adhesive contact. Section 4.3 discusses the numerical modeling of the system as well as the experimental validation. Section 4.4 discusses relevant experimental and numerical results. Finally, conclusions are presented in Section 4.5.

4.2 Theory

4.2.1 Adhesive Rolling Contact

In the early 1970's, Johnson, Kendall, and Roberts (JKR) extended the foundational contact theory of Hertz [41] to account for the effect of adhesion. Through the minimization of the total energy energy of the system, JKR developed an analytical solution relating the applied normal force P, contact half-width b, and interfacial surface energy between the contacting bodies [49]. Because the experimental observations relating to JKR theory were taken from the indentation and retraction, this interfacial energy can be referred to either as the work of adhesion w_{adh} or work of separation w_{sep} depending on whether the indenter is approaching the substrate or being retracted from it.

The use of indentation experiments with spherical or cylindrical indenters implies that the contact region is symmetric about the center of the indenter and that the crack front at each opposing edge of contact is characterized by the same interfacial energy. This symmetry negates the presence of any lateral tractive force F directed along the plane of contact. For rolling contact however, this is no longer the case. Specifically, we consider the rolling contact between a cylindrical indenter and a flat substrate under a fixed compressive normal force P (Figure 4.1a). As the indenter is rolled across the substrate, two disparate crack fronts are formed. At the leading edge of contact, a closing crack is formed, characterized by the work of adhesion w_{adh}. Similarly at the trailing edge, an opening crack forms, characterized by the work of separation w_{sep}. Because the work of separation is larger than the work of adhesion w_{adh} [16, 18], the center of contact is biased towards the trailing edge by a finite distance d relative to the center of the indenter.

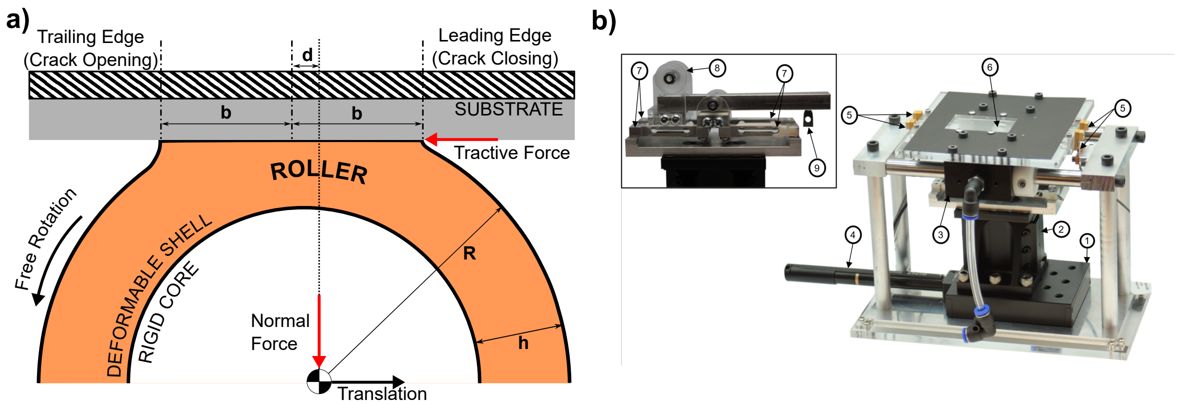

Figure 4.1: **(a)** Graphical depiction of the rolling contact experimental configuration. A free-rolling indenter, comprised of a thin shell of highly-deformable material is translated along an elastomeric substrate under a set Normal Force. Disparity in surface energies causes the contact region to be pulled towards the trailing edge and creates a tractive force. **(b)** The tribometer consists of **(1)** a sliding horizontal base and **(2)** adjustable vertical stage, **(3)** frictionless air bearings, **(4)** DC Motor with lead screw, **(5)** tractive force load cells, **(6)** substrate mount, **(7)** normal force load cells, **(8)** rolling indenter, and **(9)** counterweight attachment point [43].

Accounting for the contact region asymmetry, the normal surface traction distribution for adhesive rolling contact is [16]

$$\overline{\sigma}(r) = \frac{-P/\pi + (E^*/2R)(r^2 - rd - b^2/2)}{(b^2 - r^2)^{1/2}} \tag{4.1}$$

in which $\overline{\sigma}$ represents the normal surface traction at a coordinate r along the plane of contact relative to the center of contact. Because the crack fronts in this type of contact are not equal, r must convey both distance and direction, with positive values towards the leading edge of contact and negative values the trailing edge. P is the applied normal force, b is the contact half-width, and E^* is the plane strain modulus of the indenter shell, related to the Young's Modulus E and Poisson Ratio ν as $E^* = E/(1 - \nu^2)$ (because the substrate is two orders of magnitude stiffer than the indenter shell, it is assumed to be rigid). Using this surface traction distribution to solve for the Mode-I Stress Intensity Factor K_I and relating that to the energy release rate at each crack front, we are left with two expressions:

$$P = \frac{\pi E^* b^2}{4R} - \frac{\pi E^* bd}{2R} - \sqrt{2\pi E^* b w_{adh}} \tag{4.2}$$

at the leading edge ($r = +b$) and

$$P = \frac{\pi E^* b^2}{4R} + \frac{\pi E^* bd}{2R} - \sqrt{2\pi E^* b w_{sep}} \tag{4.3}$$

at the trailing edge of contact ($r = -b$).

Treating the indenter as a body in quasi-static equilibrium, we are further able to relate the surface traction distribution to the normal P and tractive F forces:

$$P = \int_{-b}^{b} \overline{\sigma}(x)dx \tag{4.4}$$

$$F = \frac{1}{R}\int_{-b}^{b} \overline{\sigma}(x)(x-d)dx. \tag{4.5}$$

Integrating the above equations we can relate P, F, and the contact dimensions b, d as [16]

$$P = \frac{\pi E^* b^2}{4R} - \frac{FR}{d}. \tag{4.6}$$

Using equations 4.6, 4.2, and 4.3, we can show that [16]

$$F = w_{sep} - w_{adh} \tag{4.7}$$

which is in agreement with the work of Kendall regarding rolling contact [52]. For a full derivation of this relationship, the reader can refer to Chapter 1.

4.2.2 Correction Factors

An assumption common to the aforementioned contact theories is that the bodies in question may be accurately represented as elastic half-spaces. That is, the dimensions of the contact region are small in comparison to the characteristic geometry of the bodies themselves. This assumption implies that the stress distribution within the bodies is independent of the dimensions of the contacting bodies. With highly-deformable materials, however, this assumption is invalidated even at low normal force. As described by Shull [77], as the dimension of the contact area approaches the thickness of a contacting substrate, the solids can no longer be treated as elastic half-spaces, and the observed behavior deviates significantly from predictions, necessitating the use of finite-thickness corrections. This work was later expounded on to include finite-thickness hemispherical shells [54]. Although the work in [54] involves axisymmetric geometries, we used a similar approach to account for both the curvature and finite thickness of the deformable shell of the indenter (as shown in Figure 4.1a), as will be described in Section 4.3.

4.2.3 Interfacial Friction

Another assumption for the analytical solutions is that the interface is frictionless, thus surface tractions are exclusively normal to the plane of contact and any rolling is a result only of the disparity in surface energies. However, as will be described below, experimental observations strongly implied the presence of some interfacial friction. To model the frictional component of the tractive force, we used Amonton's Law, relating the frictional surface traction $\overline{\tau}(r)$ to the normal surface traction as [48];

$$\overline{\tau}(r) = \mu\overline{\sigma}(r) \tag{4.8}$$

with μ representing the coefficient of sliding friction.

4.3 Materials and Methods

4.3.1 Experimental Section

Materials

For the substrate, we chose to use PDMS (Dow-Corning Sylgard 184 at 10:1 base:curing agent ratio). We chose PDMS because it is biocompatible, has well-documented material characteristics, can be reliably molded, and is optically clear. The mechanical properties of PDMS in this ratio are well documented [54] with a Young's Modulus of 2.9 MPa. The substrate was molded in two configurations: nominally flat and textured with micropillars. The micropillared configuration was created by curing the PDMS in a laser-etched Kapton mold. As shown in Figure 4.2, the ablative nature of the laser-etching process creates mold forms roughly in the shape of conical frustums, with a base diameter of 140 µm, top diameter of 80 µm, and height of 70 µm. The micropillars are arranged in a hexagonal array with a center-to-center spacing of 240 µm. We chose to place the micropillars on the substrate rather than the wheel to avoid straining the micropillars by wrapping a flat mold around a cylindrical roller. As the characteristic geometry of the micropillars is two orders of magnitude smaller than the indenter, the results obtained by introducing micropillars on the roller or on the substrate should be equivalent.

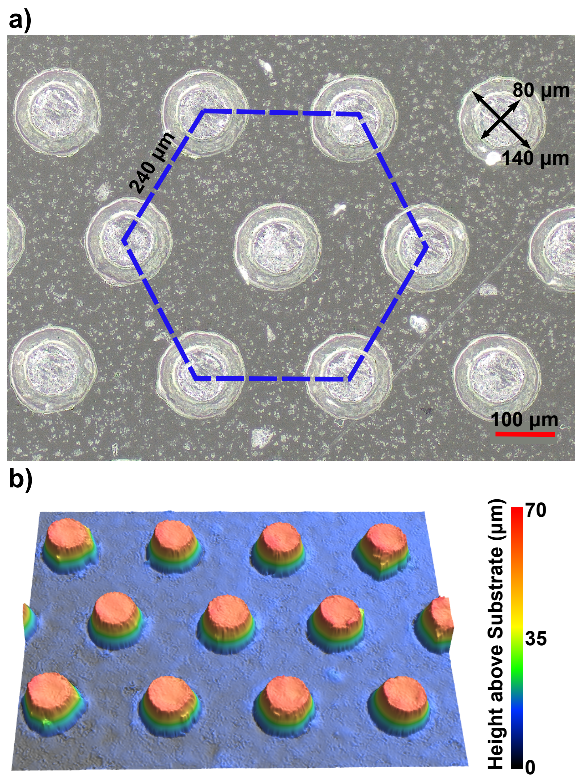

Figure 4.2: **(a)** Optical microscopy image of the PDMS micropillars formed using a laser-etched mold. The 70-µm pillars are arrayed in a repeating hexagonal pattern as indicated by the blue dashed line with center-to-center spacing of 240 µm. The scale bar represents a length of 100 µm. **(b)** A height profile of the same micropillars taken using a confocal laser microscope.

The rolling indenter is comprised of a thin (3 mm) shell of polyvinyl chloride (PVC) (M-F Manufacturing Co, Fort Worth, TX), thermally bonded to an acrylic core (6.5 mm diameter). This material was chosen because it closely matches the biological tissues likely to be encountered within an environment such as the small bowel [78, 84]. To synthesize the PVC for both our test samples and our indenter shell, the PVC was mixed with a softening agent in a 4:1 ratio by weight. The mixture was then vulcanized by heating to 175°C and degassing in vacuum. The liquid mixture was then poured into a mold and allowed to cool.

To characterize the mechanical properties of the PVC, a cylindrical test sample, 20 mm in height with a 40 mm diameter, was subjected to two tests. The first test, to characterize the hyperelastic response of the material, involved compressing the sample between two platens to a depth of 9 mm (45% strain). The data was used to characterize the material in two ways. First, a linear fit was applied to the data within 0-15% strain. Second, several hyperelastic models were compared against the full range of strain to find the most appropriate fit. For our chosen formulation, the linear fit produced an initial modulus E_0 of 18.6 kPa. The most appropriate hyperelastic model for the PVC was determined to be a 2nd-order polynomial model based on the strain energy density function

$$W = \sum_{i=0,j=0}^{2} C_{ij} \left(I_1 - 3\right)^i \left(I_2 - 3\right)^j \tag{4.9}$$

where I_1 and I_2 represent the first two strain invariants of the left Cauchy-Green deformation tensor [74]. The first-order terms for this model, C_{10} and C_{01}, were calculated as 0.0344 and -0.0302 MPa respectively ($C_{00} = 0$). To determine the initial modulus of the PVC from this model, we first calculate the initial Lame constant μ_0 as

$$\mu_0 = 2(C_{10} + C_{01}). \tag{4.10}$$

Because the material is assumed to be incompressible, the initial modulus is related to the just-discussed Lame constant as $E_0 = 3\mu_0$. The use of this model returns a slightly stiffer elastic response with an E_0 of 25.2 kPa.

The second test, to characterize the viscoelastic nature of the PVC, involved compressing the sample to 3 mm (15% strain) and allowing the sample to relax for 60 seconds. The subsequent data was fit to a Standard Linear Solid (SLS) viscoelastic model comprised of two arms: an undamped equilibrium arm (E_1) and damped maxwell arm (E_2 and η). Fitting the data to this model determined an equilibrium arm modulus E_1 of 19.5 kPa and a Maxwell arm modulus E_2 and viscosity η of 3.5 kPa and 13.3 kPa-s respectively. Thus, the PVC is determined to be only mildly viscoelastic. A full treatment of the PVC Characterization is provided in Appendix A.

Tribometer

Experimental characterization of the contact between the rolling indenter and the substrate was achieved using a 3-Degree of Freedom (DOF) tribometer (Figure 4.1b) of our own design. Full details of the tribometer design and validation are found in [43]. Briefly, for indentation normal to the plane of contact, the device can be configured for either positional control via a dial micrometer or force control by means of a fulcrum and counterweights. Translation of the rolling indenter along the substrate is achieved via a sliding stage (THORLABS PT101) actuated by a DC-Servo motor and lead screw combination (THORLABS PT1-Z8R), with PID velocity control through a proprietary motor controller (THORLABS KDC101). The indenter itself is unconstrained rotationally. An optically clear substrate is mounted to the underside of a frictionless sliding stage, above which a camera is mounted to capture the contact area.

During each test run of the device, the tractive force F and normal force P are collected via load cells mounted on the sliding stage and below the indenter base, respectively. The individual load cell signals are collected via a Data Acquisition (DAQ) module (National Instruments NI 9237) and averaged in software (Figure 4.3). In the case of force control, the moment arm due to the tractive force is also subtracted from the normal force calculation. The force data is synchronized with video of the contact area collected by the camera (Figure 4.10). Following the experiments, the force data is smoothed via a moving mean filter and the portion of the data identified as the equilibrium rolling (from 50-95% of the total elapsed time) is isolated. From that time period, ten video frames are selected to identify and measure the mean contact width.

Because of the difficulty in establishing a reliable point of initial contact, particularly for the micropillared substrate, we determined that a force controlled experiment was most appropriate.

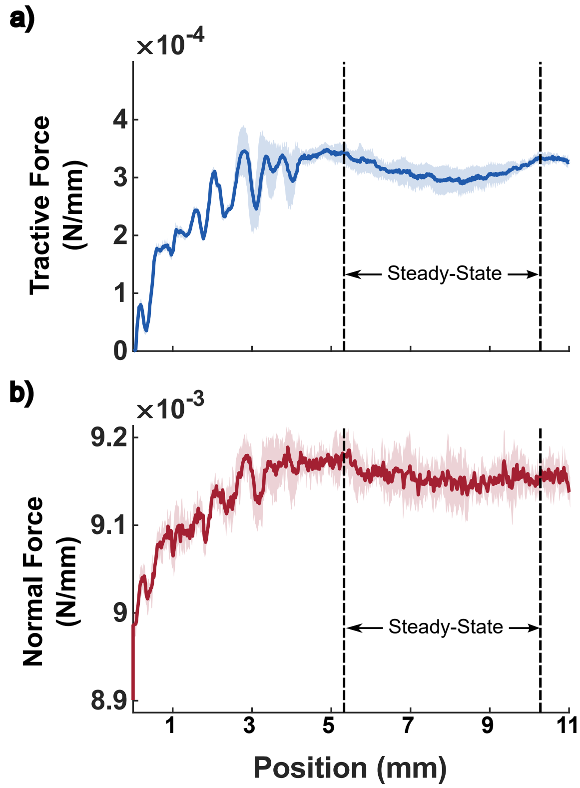

Figure 4.3: Graphical depiction of **(a)** tractive force and **(b)** normal force as measured by the tribometer. The solid line and shaded area represent the mean and standard deviation, respectively, of the measurements taken from eight individual test runs at a fixed translational speed and imposed normal force. The dashed lines indicate the extent of the experiments determined to represent steady-state rolling.

Four imposed counterweights of 10, 20, 30, and 40 g were applied, and each counterweight was tested at four randomly-selected velocities of 0.02, 0.1, 0.32, and 0.75 mm/s. Each counterweight/velocity combination underwent eight individual test runs.

4.3.2 Finite Element Model

A finite element (FE) model of the experimental geometry was developed for two reasons. First, the model was used to determine the appropriate finite-thickness correction factors in the highly deformable PVC. Second, the predicted adhesive and frictional response from the model was compared against experimental results for the flat substrate.

Geometry and Material Models

The FE model for the system was built in ABAQUS (Dassault Systemes Americas Corp, Waltham, MA), using a 2-Dimensional plane strain geometry. The indenter was modeled as a deformable solid with a rigid core which was enforced through kinematic constraints. Because both the PDMS and PVC are considered incompressible, both the substrate and cylindrical shell were modeled using linear quadrilateral elements with hybrid formulation (CPE4H). Because the PDMS is roughly two orders of magnitude stiffer than the PVC, it was assumed that strain in the PDMS would be minimal. Thus, the PDMS was modeled as an incompressible neo-Hookean hyperelastic material with initial modulus E_0^* of 2.9 Mpa ($C_{10}^* = 0.4833$, $D_1 = 0$). The substrate in the simulation is 3 mm deep by 25 mm long.

The PVC was modeled as a second order polynomial hyperelastic material with coefficients from the material characterization described above. The simulated response was then compared with experimental results at one velocity (0.1 mm/s) and the first-order coefficients C_{01} and C_{10} were tuned to better fit the data (Figure 4.8). The coefficients of best fit were C_{01} = 0.0333 and C_{10} = -0.0297, which represent a change of less than 3% from the experimentally determined values. These values lead to an initial modulus E_0 of 21.6 kPa, which falls between the linear and hyperelastic predictions from the material characterization. The full list of coefficients is shown in Table 4.1. The thickness of the cylindrical shell in the simulation is 3 mm to match the experimental geometry.

List of Coefficients - Hyperelastic PVC Model (MPa)	
C_{01}	0.0333
C_{10}	-0.0297
C_{02}	-5.8539
C_{20}	0.8903
C_{11}	5.0248

Table 4.1: The list of coefficients for the second-order polynomial fit used when simulating the hyperelastic behavior of the PVC based on the strain energy density function described in Equation 4.9.

Correction Factor Determination

As described by Shull [77], the assumption that contacting bodies can be treated as elastic half-spaces ceases to be valid once the dimensions of the contact region approach the characteristic geometry of either of the bodies. Once this occurs, it is necessary to apply correction factors to align analytical predictions with experimental observations. Although Shull's work focused on rigid indenters contacting thin substrates, his method was later extrapolated to account for thin deformable shells on a rigid spherical core against a flat substrate [54]. We have chosen an approach similar to [54] because it takes into account both the finite thickness and curvature of the cylindrical shell.

As the two bodies are brought into contact, the state of stress within the PVC quickly reaches a point at which the connection to the rigid core contributes to the resulting normal force. To reconcile analytical predictions with experimental observations, a correction factor f_p must be multiplied by the analytical prediction. This correction factor is a function of the ratio between the contact half-width b and a characteristic dimension h of the experimental configuration. In this case, h represents the thickness of the PVC shell. To determine the appropriate function for the correction factor, analytical predictions must be compared with experimental or simulated observations.

To determine the correction factor for our experimental configuration, we first simulated an adhesionless, frictionless indentation experiment involving the PDMS substrate and PVC cylindrical shell. The data from that simulation was then used to compare the ratio between the measured normal force P with the predicted Hertzian normal force P_H (Figure 4.5 Inset), defined as [18]

$$P_H = \frac{\pi E^* b^2}{4R}. \tag{4.11}$$

The data was then fit with a 3rd-order polynomial

$$f_p = \frac{P}{P_H} = a_4 \left(\frac{b}{h}\right)^3 + a_3 \left(\frac{b}{h}\right)^2 + a_2 \left(\frac{b}{h}\right) + a_1 \tag{4.12}$$

constrained such that the correction factor is equal to one when the contact half-width is zero. The simulation results and subsequent polynomial fit are shown in Figure 4.4 (Inset). The coefficients for the polynomial fit are shown in Table 4.2.

List of Coefficients - Correction Factors	
a_4	0.1021
a_3	0.6888
a_2	-0.0303
a_1	1

Table 4.2: The list of coefficients for the finite-thickness correction factors for the thin cylindrical shell of PVC.

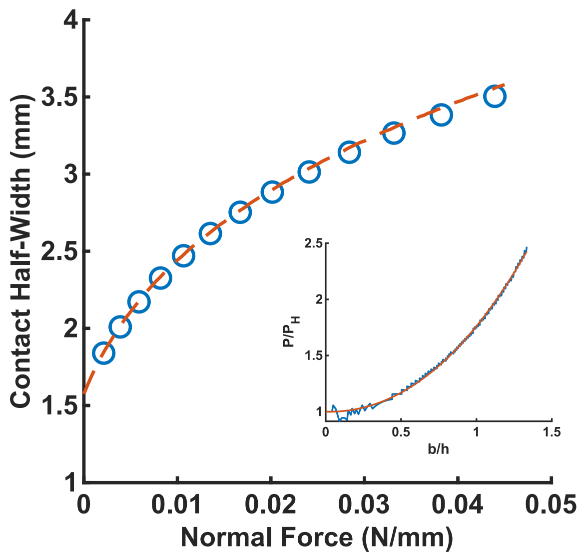

Figure 4.4: Comparison of contact half-width vs. normal force for numerical simulation (blue circles) and analytical solutions with finite-thickness correction factors (red dashed line). Although the correction factors are determined without adhesion, they still provide a reliable approximation for adhesive rolling contact. **(Inset)** Comparison of actual force P to Hertzian predictions P_H with numerical results (blue line) and correction factors (red line).

Adhesive Rolling Contact

The primary consideration when modeling adhesive rolling contact was how to simulate adhesion. Adhesion leads to tensile stresses at the edge of contact. Theoretical approaches of modeling adhesion (e.g., the JKR Theory) treat the gap outside the contact region as an interface crack which implies a square-root singularity of tensile stress at the contact edge (Figure 4.5a). This is problematic for simulations for two reasons. First, the abrupt transition from infinite stress at the edge of contact to zero stress immediately outside the contact area represents a large discontinuity which makes finding a convergent solution difficult. Second, any solution will be dependent upon the mesh size of the model, as finer meshes will allow the stress distribution to approach ever nearer to infinity. To alleviate this singularity, numerical models of adhesion rely on cohesive zone models (CZMs) which place an effective limit on the stress. The first CZMs, developed by Dugdale [23] and Barenblatt [6, 7] to describe the effect of plastic yielding in crack propagation, are referred to as "strip-yield" models, in which stress rises to a set ceiling and remains constant throughout the crack tip region. Several other models for cohesive zones have been developed [67, 45]. For our numerical model, we used a bilinear cohesive zone model (Figure 4.4b). In a bilinear CZM, from the point of separation, surface traction $\overline{\sigma}$ increases linearly with separation distance δ until a critical stress $\overline{\sigma}_c$ or separation δ_c is reached, at which point the stress softens linearly to zero at the separation distance δ_s. Provided that the crack tip region is small compared to the system geometry, and that rate-dependent effects such as visco- or poroelasticity are minimal, CZMs will provide an equivalent solution if the integral of the surface traction through the crack tip region is equal to the interface energy w_{sep}.

Because standard contact implementations within ABAQUS only account for the separation of nodes already deemed in contact, we are only able to simulate the separation at the trail edge, neglecting the closing crack at the lead edge. This requires a slight modification of the analytical solutions. Because w_{adh} is assumed to be zero, the surface traction at the lead edge of contact ($r = +b$) must be precisely zero to preclude a stress singularity. With this constraint, Equation 4.1 simplifies to

$$P = \frac{\pi E^* b^2}{4R} - \frac{\pi E^* bd}{2R}. \tag{4.13}$$

We achieve an identical result by setting w_{adh} to zero in Equation 4.2. Equating the normal force P in Equations 4.3 and 4.13, we derive a new expression for the work of separation:

$$w_{sep} = \frac{\pi E^* bd^2}{2R^2}. \tag{4.14}$$

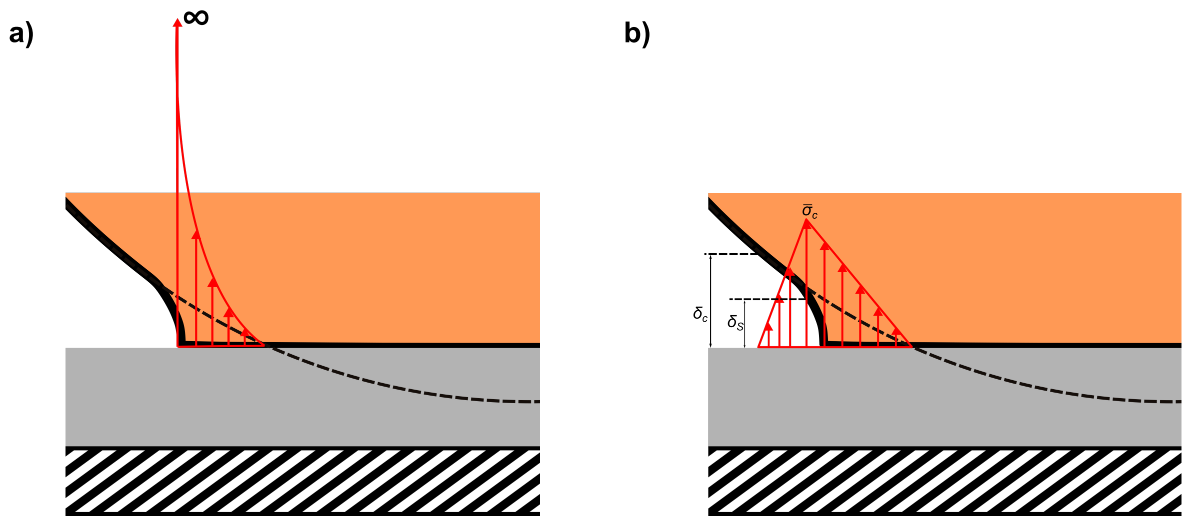

Figure 4.5: Because adhesive forces are present, the analytical solution for surface traction **(a)** approaches infinity at the edge of contact. To eliminate this singularity, we have implemented a bi-linear Cohesive Zone Model (CZM) **(b)**, which provides equivalent results provided that the integral of the resulting surface traction is equal to the surface energy between the contacting bodies.

Similarly, by equating normal force P in Equations 4.4 and 4.13, we find the following expression for tractive force F:

$$F = \frac{\pi E^* b d^2}{2R^2}. \tag{4.15}$$

We see that the expressions for F and w_{sep} are equal, the same conclusion that could be drawn from Equation 4.7 if w_{adh} were zero. Although w_{adh} is not exactly zero in practice, it is generally understood that the work of separation is sufficiently larger than the work of adhesion [16, 75, 54], so it is anticipated to provide a reasonable approximation.

To replicate the conditions of the experiment, the simulation is divided into two steps. In the initial configuration, the indenter and substrate are positioned so as to contact at a singular point. In the first step, the roller is indented perpendicular to the substrate to a fixed indentation. That indentation is held fixed for the second step, in which the indenter is translated 3 mm along the substrate. For this step, the rotation of the indenter is unconstrained - any rotation arises from the adhesive interaction at the trailing edge, defined using the bilinear CZM described above. Both steps of the simulation are dynamic (implicit) quasi-static steps.

Throughout the simulation, relevant time-series data collected included the indentation depth, tangential displacement, and rotation of the indenter (u_2, u_1, and ur_3 respectively), as well as reaction forces $RF1$, corresponding to the adhesive component of tractive force, and $RF2$, equal to the normal force, and contact area. Because the simulation geometry is of unit depth, the output contact area is equivalent to the contact width $2b$.

To confirm the equivalence of the analytical solution with correction factors and simulated data, Equations 4.12, 4.13, and 4.14 were used to solve for the contact half-width for a range of normal forces, which were compared against the numerical outputs. The two compared very favorably, as shown in Figure 4.4.

Interfacial Friction

Current contact formulations within ABAQUS do not allow the combination of frictional and adhesive contact in the context of rolling contact, as elements within the contact zone that are allowed to slip would be identified as not in contact and would not be factored in to the adhesive interaction at the trailing edge. Thus, tractive force due to friction was calculated as a post-processing step to the simulation. We hypothesize that the frictional shear traction within the contact region is equal to the compressive normal traction multiplied by a friction coefficient μ, while adhesion is controlled by the tensile normal traction at the contact edge (i.e., a Mode-I interface crack).

Using the time history of the contact width from the simulation, the equilibrium rolling portion was identified by the point at which the contact area became constant. For each increment within this time period, the contact pressure and stress components were recorded for all the nodes along the surface of the PDMS Substrate. The region of compressive contact ($-a \leq r \leq b$) at each instant was denoted by the nodes reporting positive contact pressure (see Figure 4.6). Using the equilibrium boundary condition for a continuum solid and assuming that the PDMS substrate remains planar, the normal surface tractions at each point were calculated as:

$$\overline{\sigma} = \sigma_{ij} n_j = \sigma_{22} \tag{4.16}$$

Applying Equation 4.8, the total Tractive Force due to friction F_μ is

$$F_\mu = \mu \int_{-a}^{b} \sigma_{22} dx. \tag{4.17}$$

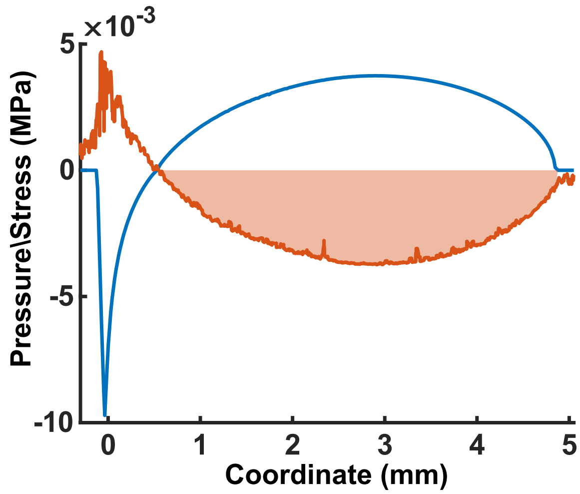

Figure 4.6: The contact pressure (blue line) and normal stress component (red line) for the surface nodes within the contact region of the flat PDMS substrate at an instant of steady-state rolling contact in the finite element model. The shaded area represents the integral of the stress which was subsequently used to calculate the frictional component of the tractive force.

4.4 Results and Discussion

4.4.1 Model Validation

The design of the experiment, specifically the variation in velocity and normal force, was intended to highlight two potential tractive effects. First, by controlling velocity, the rate dependent nature of adhesion could be observed. Second, by controlling normal force, any observed dependence would imply a frictional component to the surface traction. By superimposing the two effects, an expression for the total tractive force

$$F = F_a + F_f = kV^n + \mu P \tag{4.18}$$

could be derived, with V representing the translational velocity of the indenter, P the imposed normal force between indenter and substrate, and F_a and F_f denoting the adhesive and frictional components of the tractive force, respectively. Controlling for Normal Force (Figure 4.7a), a linear best fit was calculated for each velocity. The mean and standard deviation for all velocities are μ of 0.021 $\pm$ 0.004. In a similar fashion, a linear best fit between $\ln(F)$ and $\ln(V)$ was calculated to determine the mean values of k (1.102 $\pm$ 0.88 mN/mm) and n (0.361 $\pm$ .04). For each test condition, defined as a specified normal force/velocity combination, the first test runs were arbitrarily discounted as they exhibited a significantly different response due to run-in effects. From the remaining 112, experiments, 11 were eliminated as outliers for their respective test condition. To test the overall fitness of the model, a Root Mean Square Error (RMSE) for the remaining 101 experiments was calculated. The overall RMSE for the tractive force was 3.4% normalized to the mean experimental tractive force at each normal force/velocity pairing.

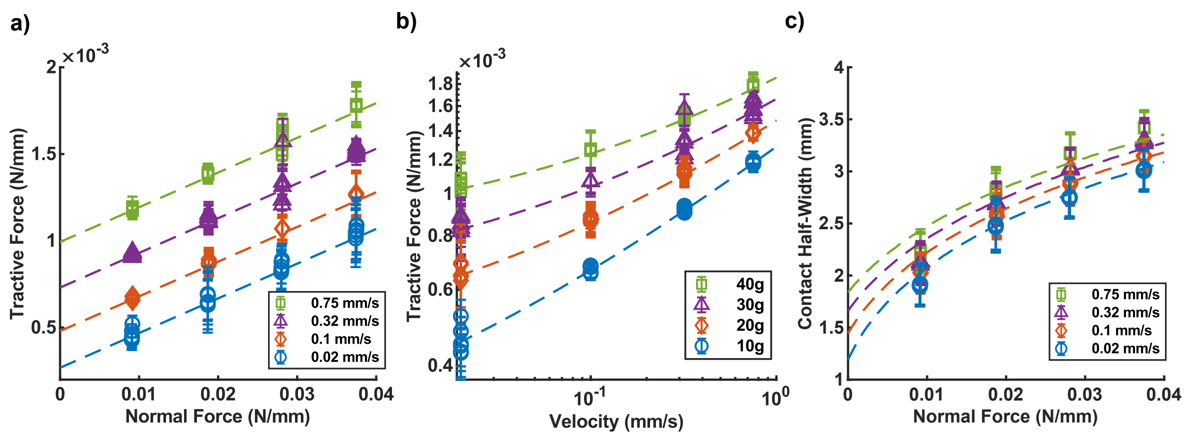

Figure 4.7: Graphical comparison between experimental results (discrete points with error bars) and predictive models (dashed lines): tractive force as compared to **(a)** normal force and **(b)** translational velocity and **(c)** contact half-width as compared to normal force. For each subfigure, each shape and error bar represent the mean and standard deviation for a single experiment. Each velocity/normal force pairing represents between four and seven individual experiments (after removing outliers). The dashed lines in subfigures **(a)** and **(b)** represent the expected values from Equation 4.18, while those in subfigure **(c)** represent values predicted by Equations 4.13 and 4.14, taking into account finite-thickness correction factors as per Equation 4.12. For **(b)**, the values in the legend represent the mass of the counterweight applied to the fulcrum for force control.

To validate the FE model and normal force correction factors, a single velocity (0.1 mm/s) was selected. The subsequent CZM was configured based on the work of separation derived from the velocity-dependent term of Equation 4.18. Other relevant parameters of the CZM were a slope

K_{nn} of 0.5 and critical stress of 14 kPa, leading to an overall CZM width of 64 µm. For the post-processing, the value of μ calculated above was used to determine the frictional contribution to the tractive force.

The results were compared using the relationships between contact half-width and normal force (Figure 4.8a) and tractive force and normal force (Figure 4.8b). From Figure 4.8a, we see that the actual response appears slightly stiffer than predicted, moreso at lower applied load. We believe this discrepancy is a result of two factors. First, the numerical model accounts only for separation at the trailing edge, while experimental results incorporate adhesive interactions at both edges - although the resulting tractive force is comparable, it is difficult to predict how the actual surface interactions will affect the contact width and asymmetry. Secondly, there may be some biasing in the image processing - as shown in Figure 4.10a, it was not possible to achieve perfectly level contact between the cylinder and substrate, so a mean contact area was calculated for each frame - this may have created a more pronounced underestimate at lower normal forces with proportionally smaller contact areas. From Figure 4.8b, we see that the friction seems slightly more pronounced than predicted, a reflection of the fact that the empirical solution incorporates a pooled mean from all the velocities.

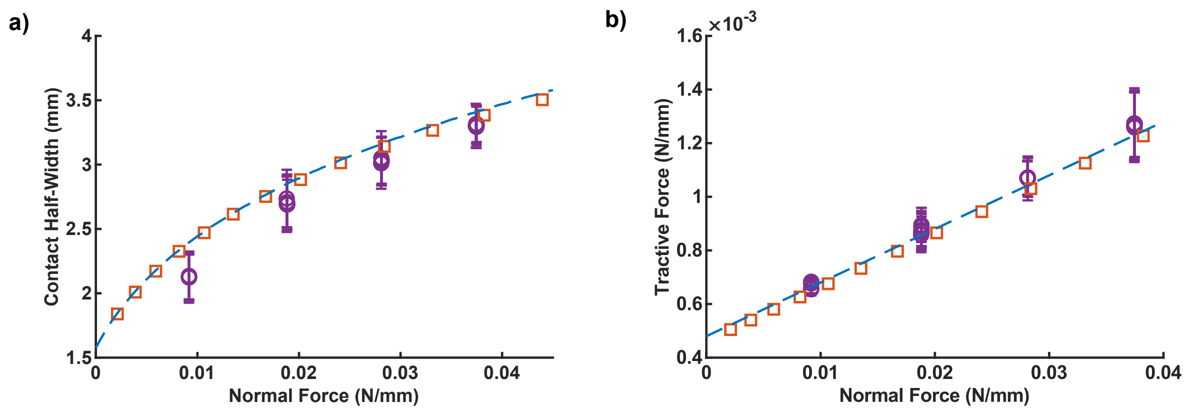

Figure 4.8: Comparison of experimental (purple circles), numerical (red squares), and predictive models (dashed lines) taken at a single velocity: **(a)** Contact half-width vs. normal force and **(b)** tractive force vs. normal force. Each experimental data point (purple) represents the mean and standard deviation of one experiment - each grouping includes between four and eight experiments, after removing outliers.

4.4.2 Micropillared Substrate

To test the effect of micropillared surfaces on the rolling contact of soft elastomers, the flat PDMS substrate was replaced by a substrate formed by curing the PDMS in a mold made from laser-etched Kapton (Figure 4.2). To compare the flat and micropillared response, the same array of counterweights and translational velocities as the flat substrate were used, and a similar fitting process was accomplished. Using this same model, we arrived at adhesional terms of k equal to 1.024 ± 0.13 mN/mm and n equal to 0.357 ± 0.06, as well as a frictional term μ equal to 0.024 ± 0.006. The computed RMSE for the micropillared data, again normalized by mean tractive force at each pairing, was 5.4%. A comparison of relevant terms between the flat and micropillared substrates is shown in Table 4.3.

Tractive Force Modeling		
	Flat	Micropillared
k (mN/mm)	1.102 ± 0.88	1.024 ± 0.13
n	0.361 ± 0.04	0.357 ± 0.06
μ	0.021 ± 0.004	0.024 ± 0.006

Table 4.3: A comparison of the relevant coefficients for the predictive model for tractive force for both flat and micropillared substrates.

Figures 4.9a and 4.9b depict the relevant tractive force relationships for the micropillared substrate in comparison to the flat substrate (flat data are depicted as gray dash-dot lines intersecting their respective micropillared trend lines). As shown in the figures, as well as by comparing the coefficients of the empirical model from Table 4.3, we see that, in the case of very soft materials, the effect on rolling contact from the addition of micropillars is very modest. Comparing the values of k, it appears that the addition of micropillars has the effect of lowering the adhesive component of tractive force by approximately 7%. We believe this moderate lowering of adhesion is a reflection of the ratio between real and apparent contact area due to the addition of micropillars. The highly deformable PVC readily conformed to the pillared substrate and backing layer contact was observed even under the lowest applied normal loads (Figure 4.10b). If we represent the micropillars as regular conical frustums, it is possible to estimate the bounds of real contact

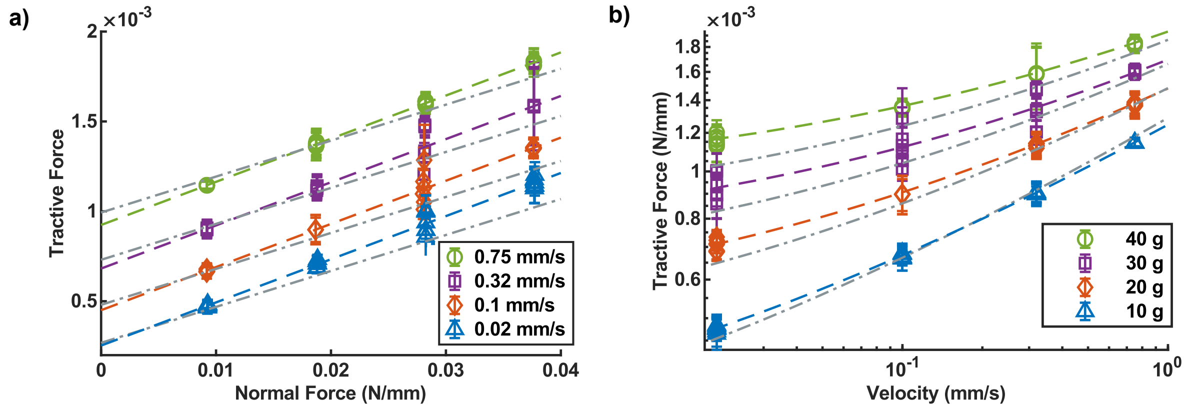

Figure 4.9: Graphical comparison between experimental results (discrete points with error bars) and predictive models (dashed lines): tractive force as compared to **(a)** normal force and **(b)** translational velocity. For each subfigure, each shape and error bar represent the mean and standard deviation for a single experiment. Each velocity/normal force pairing represents between four and seven individual experiments after removing outliers. The dashed lines in subfigures **(a)** and **(b)** represent the expected values from Equation 4.18. To highlight the modest effect of micropillars when using a highly-deformable material such as PVC, the expected values from the flat substrate experiment (see Figure 4.7) are included as gray dash-dot lines overlain on the micropillared data of corresponding velocity **(a)** and normal force **(b)**.

area for a representative hexagonal element as shown in Figure 4.2. Assuming uniform frustums, a minimal contact scenario, involving contact with only the tops of the micropillars, would have a real to apparent contact ratio of 0.101. Conversely, a maximal contact scenario, with contact at the tops and sides of the frustums as well as the interstitial backing layer, would have a contact ratio of 1.28, keeping in mind that the actual contact area would likely be considerably less due to surface roughness. If the change in adhesion (0.93) reflects the change in real contact area, this would imply that the soft PVC is achieving near maximal contact with the micropillared substrate, as reflected in our experimental observations. As shown in Figure 4.10b, only one or two rows of micropillars at the periphery of contact exhibits partial contact, while the preponderance of the contact region exhibits near maximal contact with sustantial backing layer contact.

Comparing the frictional contributions of tractive force, it appears that the addition of micropillars raises the coefficient of friction μ by approximately 14%. Because friction, like adhesion, is an areal phenomenon, one would predict that the addition of micropillars would similarly decrease the frictional response. We believe the increase in friction arises because the micropillars, when in

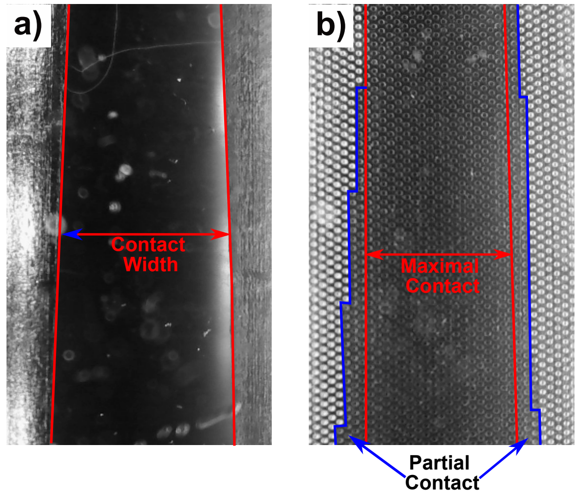

Figure 4.10: Comparison of contact areas for the soft PVC indenter against **(a)** smooth PDMS substrate and **(b)** micropillared substrate. As delineated in **(b)**, a majority of the micropillared contact region appears to be in a state of maximal contact - the extent of backing layer contact explains why micropillars lead to very modest changes to rolling contact when interacting with highly-deformable materials.

contact with the highly deformable PVC, act as grousers. While sliding along the substrate, the PVC is compacted against the leading edges of the pillars, leading to internal shear stresses and increasing the frictional response. This effect likely explains the observed improvement in tractive response when incorporating micropillars in wheeled robots [25, 56] and endoscopy balloons [14] interacting with highly deformable tissues.

4.5 Conclusion

Advancements in the fields of medical and soft robotics have greatly increased new and potential applications in which devices can be expected to interact dynamically with soft biological tissue. Improved predictive models can help to narrow the space for designers in choosing materials and structures for the locomotive components of their devices and could also help tune the control algorithms of motive devices to perform more efficiently. In this study, we have collected experimental observations on the rolling contact between a bio-compatible elastomer and a highly deformable, tissue-like material in order to characterize the tractive response. Through these experiments, we observed what we believe to be an adhesive, velocity-dependent component and a frictional, normal force-dependent component. These observations were compared against analytical and numerical solutions, and were incorporated into a predictive model relaying tractive force to both velocity and normal force.

Comparison of experimental results between a flat and micropillared substrate showed very modest changes between the two, which we attribute to the fact that the relative softness of the PVC leads to a very small difference between the real and apparent contact areas. These results suggest that better micropillar efficacy could be derived from choosing micropillars which are more densely packed or of higher aspect ratio so as to reduce the degree of backing layer contact.

Chapter 5

Experimental Investigation of Mesopillar Geometry Factors by means of Rapid Prototyping

5.1 Introduction

Through the last several chapters, we have described efforts towards the characterization of the rolling contact of soft elastomers through both experimental and numeric means. Ultimately, this was to show the effect of adding microtextures to the contacting substrate. However, as shown in Chapter 4, the overall effect, in both contact stiffness and tractive response, was very modest for the highly deformable PVC. We believe this is due to the fact that, for such a soft material, interpenetration between the micropillars and backing layer contact occur even at very low load. This phenomenon could potentially be prevented by altering the pillar geometry to either (a) tighten the spacing between micropillars or (b) increase the aspect ratio of the pillars, making them taller. Unfortunately, these modifications are not easily accomplished with the current micropillar manufacturing techniques. To effectively test the effect of geometric factors, such as pillar shape and aspect ratio, we are proposing to increase the geometric scale of our pillars from the micro- to the sub-millimeter (hereafter referred to as meso) scale, thus enabling the use of readily-available rapid prototyping techniques.

For this study, we have adapted two manufacturing methods, 3D printing and laser writing, for the development of mesopillars using commercially available, comparatively low-cost systems that would conceivably be available in the labs or shared-use facilities for most researchers at academic institutions today. To test the efficacy of the mesopillars, we have tested them under three conditions: rolling contact with a rigid (acrylic) indenter, rolling contact with a highly-deformable (PVC) indenter, and sliding contact with the same deformable indenter. The resultant tractive forces were compared to those of a flat substrate, as well as a substrate with micropillars formed from a laser-etched Kapton mold.

Before discussing our own manufacturing and testing methods, Section 5.2 will outline the two most prominent manufacturing methods for micropillars: photolithography and laser-etched negative molds. In Section 5.3, we will discuss our own manufacturing methods and testing procedures. Section 5.4 will compare the resultant mesopillar geometries, as well as their observed effects on the aforementioned contact regimes. The conclusion of this study is found in Section 5.5

5.2 Micropillar Manufacturing

This section is not intended as an exhaustive review of the state-of-the-art in micropillar manufacturing. This is undoubtedly a burgeoning field, with an ever-growing list of techniques in micro-machining [20, 21], direct laser writing [85, 65] and other procedures [88, 58]. Instead, we discuss what are likely the two most used and readily available techniques from a research standpoint - photolithography and laser etching - within the context of rapid prototyping.

5.2.1 Photolithography

For the manufacture of monolithic[1] micropillars, the use of photolithographic molds is arguably the most prominent technique [50, 30, 87]. The production of a lithographic mold is a time-consuming, multi-step process (Figure 5.1b) [62]:

(1) The design for the mold must be generated using Computer-Aided Design (CAD) software. Depending on the file format needed, this may require the use of proprietary software.

(2) The design is etched onto a glass mask coated in a photo-resistive film using a direct laser writer. Once the writing process is complete, a chemical developer is used to permanently set the etched pattern.

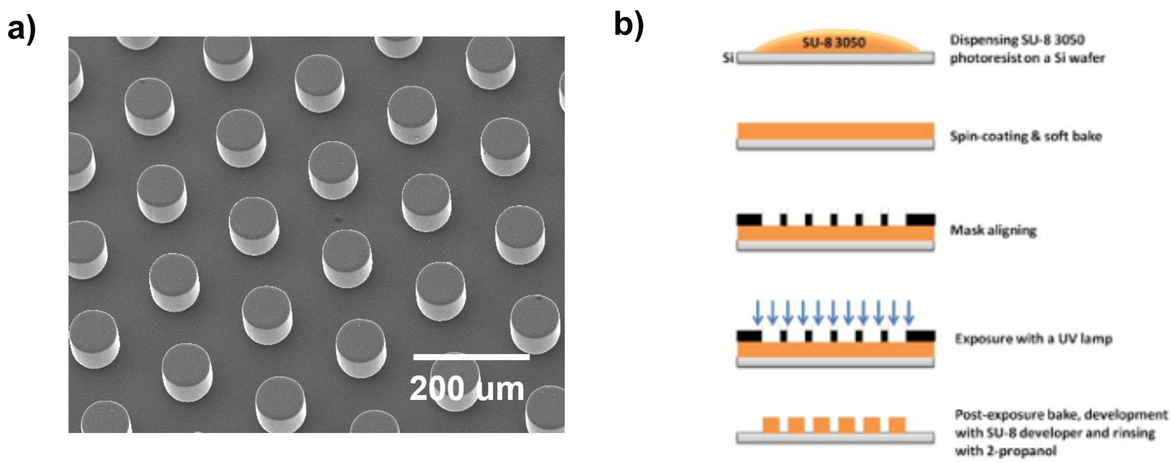

Figure 5.1: **(a)** A scanning electron microscope (SEM) image of micropillars formed using an SU-8 Lithography mold, **(b)** The major steps in developing a photolithograhic mold, a process which typically takes 5-6 hours per mold. Subfigure (b) courtesy [62], ©InTechOpen 2020.

(3) In a cleanroom environment, a photoresistive compound (SU-8 or similar) is deposited on a silicon wafer and spun at high RPM to achieve a film of consistent thickness. The height of the film, which will correspond to the height of the pillars, is determined by the rate of spin.

(4) After the photoresist is subjected to initial heat treatment, the silicon wafer and mask are aligned using a mask aligner, which then exposes the photoresist to focused ultraviolet light. Unmasked areas of the photoresist are crosslinked by the UV exposure.

(5) A chemical developer is used to remove the un-crosslinked photoresist, leaving a negative mold.

Photolithography has many advantages for micropillars. First, the resolution for the mask and photoresist is typically in the micrometer range, so it is possible to create pillars with complex shapes. Additionally, SU-8 lithography is a well-established procedure so there is a wealth of information and best practices, both from photoresist manufacturers and the research community. Finally, photoresists can generate high aspect ratio pillars, with heights of 100-150 µm, provided the right material and careful procedural control.

The primary drawback of photolithography is time: mask and mold development are both time-consuming processes, likely requiring weeks from mask design to pillar molding. If resources are available on site, the researcher has the option to print the mask and develop the mold themselves, but by doing so incur the liability in time and cost of failed prints, which are very likely. Additionally, the production of anything other than monolithic pillars using this technique typically requires a multi-step exposure and development process requiring precise alignment of mulitple masks, or else complicated secondary procedures. A second disadvantage is that any desired change in the desired height of the pillars (and thus the mold) will likely require the development of an entirely new process: beyond the need to adjust the spin speed, mold height will effect the time at which the mold must be exposed, cured, and developed. Although photoresist producers provide guidelines which take mold height into account, these can be effected by any number of environmental factors, so high resolution applications like micropillars and microfluidics require the researcher to tune their own process through trial-and-error.

5.2.2 Laser-Etching

A second widely-used method for producing micropillar molds is laser etching, a process by which a precision laser is used to directly etch a micropillar negative into a rigid substrate, either metal or a rigid plastic. This has the distinct advantage that the mold is directly written from the CAD file, allowing the process to be automated. However, the major disadvantage is that laser writing is an ablative process which has implications in the resolution, verticality, and surface characteristics of the pillars. As can be seen in Figure 5.2a, pillars formed via this method are much more conical, do not have a flat top surface, and have clearly evident surface texturing, likely in the order of 10s of micrometers. All of these factors can be minimized through the use of highly-controlled laser bursts, but that requires access to highly specialized femtosecond lasers which are not likely readily available to most researchers.

[1] For the purposes of this paper, we define monolithic as having straight vertical profiles.

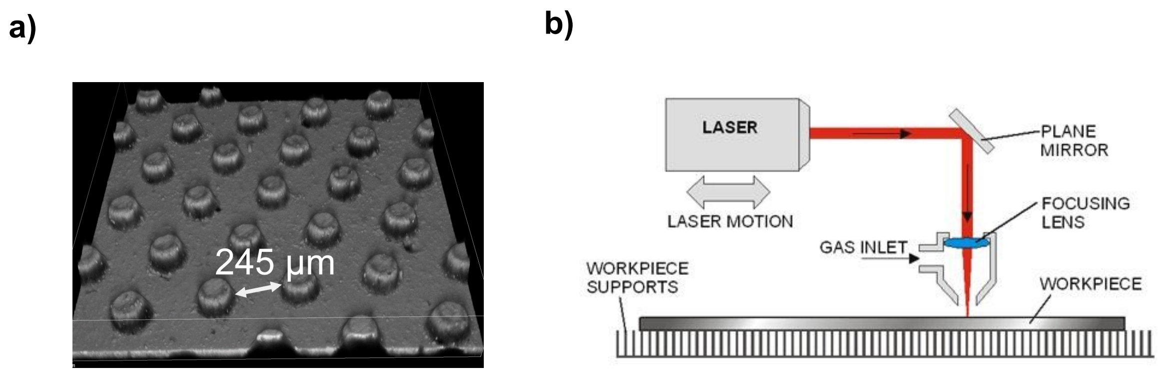

Figure 5.2: **(a)** A laser confocal microscope (LCFM) image of micropillars formed using a laser written mold. **(b)** A schematic of the laser writing process. Subfigure (b) courtesy dkphotonics.com

5.3 Methods and Materials

Given the limitations of the above procedures, we are proposing to use two readily-accessible technique - 3D printing and laser engraving - to rapidly prototype and test novel pillar geometries. Both techniques, as described below, will necessarily require that the scale of the pillars be increased by roughly an order of magnitude from the micro- to the mesopillar range.

5.3.1 Mesopillar Manufacturing

Pillar Geometry

To highlight the ability of our prototyping techniques in producing pillars with novel geometries, we have chosen two pillar shapes: a standard circular pillar and a "goldfish" pillar (Figure 5.3, both of which we attempted to produce at four aspect ratios: 1:1, 2:1, and 4:1, with aspect ratio defined as the height of the mesopillar compared to its major diameter. The goldfish design was chosen because it could be scaled such that it presented an equal cross-sectional area to the circle, and because one direction of contact, the convex, would present a leading edge equal to the circular pillar, while contact from the concave side should be noticeably different. For both geometries, the major diameter was selected to be 500 µm.

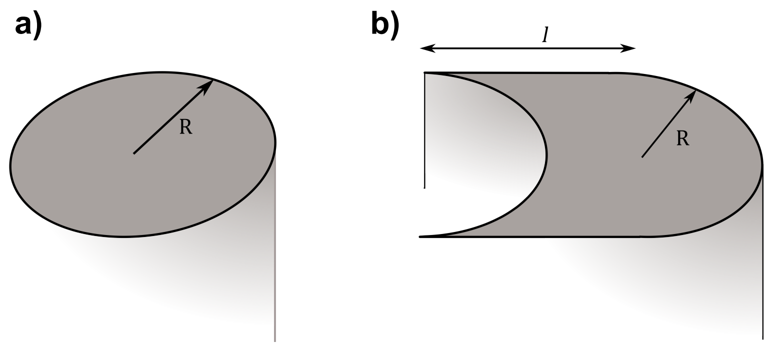

Figure 5.3: Schematic of the selected geometries for mesopillar prototyping: **(a)** a standard circular pillar and **(b)** a "goldfish" pillar. The goldfish was chosen because, by tuning length l, the cross-sectional area can be made equal to that of the circle. Additionally, the convex side presents a leading edge identical to the circle, while the concave is radically different. Attempts were made to manufacture each geometry at aspect ratios of 1:1, 2:1, and 4:1.

3D Printing

For the 3D-printed pillar molds, we will be using a FormLabs Form2 printer (Formlabs, Inc., Somerville, MA), located in our lab. The Form2 is a stereolithography (SLA) printer, capable of printing high-resolution (to 25 µm) objects using a UV-cured resin. Producing a mold is a three-step process (Figure 5.4):

(1) The mold is designed using a commercially-available CAD software, in this case Solidworks (Dassault Systemes Americas Corp, Waltham, MA). The geometry is imported into Formlabs proprietary software, PreForm, which arranges the piece and supports and generates the code instructions for the printer. Once complete, the print is started.

(2) After printing and curing the mold, a flexible silicone (Smooth-Sil 945, Smooth-On Corp., Waltham, MA) is poured into the mold and allowed to cure.

(3) Once cured, the silicon is removed, forming a negative pillar mold.

Laser Engraving

For the laser-engraved mesopillars, we will be using a Trotec Speedy 360 (Trotec USA, Plymouth, MI), a commercially-available and readily-accessible laser cutter, also located in our lab

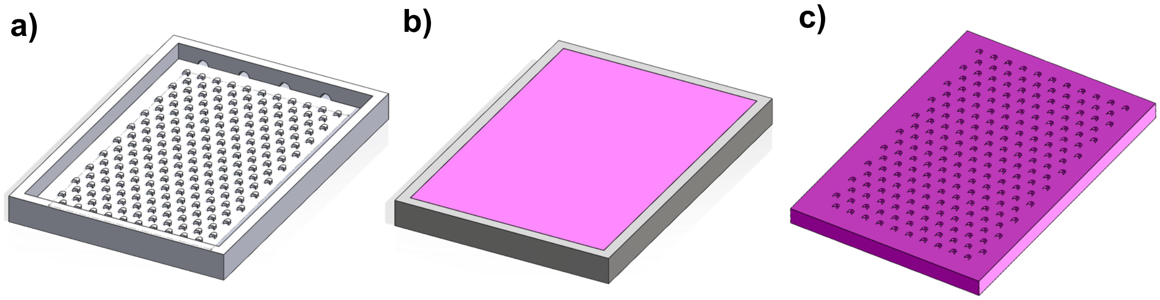

Figure 5.4: Graphical depiction of the 3D Printed molding process: **(a)** A positive pillar mold is printed using the Form2 Printer, **(b)** a flexible silicon is poured into the mold and allowed to cure, and **(c)** the negative silicone mold is removed.

space. This is also a three-step process (Figure 5.5):

(1) The CAD file with array of pillar geometries is exported as a drawing (.dwg) file which is post-processed using CorelDraw (Corel Corp., Ottowa, ON, CAN).

(2) The drawing is sent to proprietary printer software. Within the software, the color of features is used to determine the parameters by which they are cut or engraved. The depth to which the material is engraved can be tuned through the combination of printhead speed, laser power, and number of passes.

(3) The print job is executed by the printer. Because the laser is being used to develop a positive mold, material is engraved away around the pillars. Depending on the parameters chosen for engraving, a typical mold takes 7-12 minutes.

(4) As with the 3D printing process, a flexible silicone mold is poured into the positive mold and allowed to cure.

5.3.2 Testing

Experimental Materials

For all experiments in this study, the substrate material was poly(dimethylsiloxane) (PDMS) (Sylgard 184, Dow-Corning) in a 10:1 base:curing agent ratio. PDMS was chosen because it is

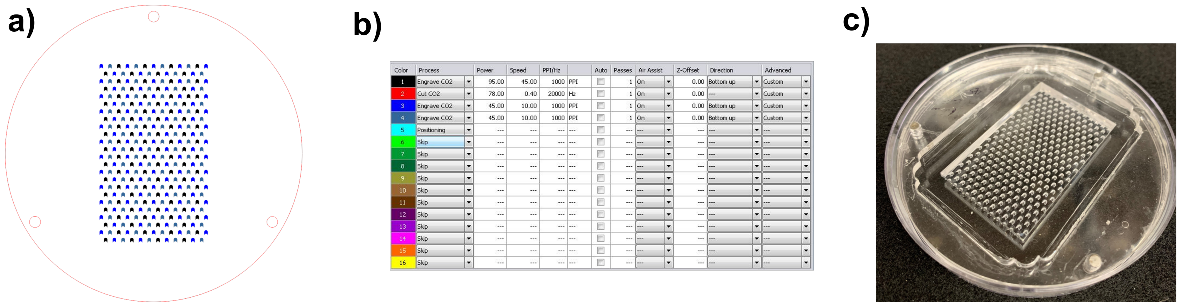

Figure 5.5: A graphical depiction of the laser-engraving process: **(a)** The CAD file is exported as a drawing and post-processed in CorelDraw, **(b)** Parameters for cutting and engraving are set based on feature color from the drawing, and **(c)** the print job is executed.

bio-compatible, has well-documented physical properties, and is optically clear, allowing for image capture of the contact area through the substrate. As documented in the literature, PDMS is an incompressible material with an elastic modulus E of 2.9 MPa [54, 18].

To test the mesopillar efficacy under different contact conditions, two indenters were chosen. The first consisted of a nominally smooth acrylic cylinder with a radius of 9.525 mm. The second indenter comprised a thin (3 mm) layer of highly-deformable poly(vinyl chloride) (PVC) (M-F Manufacturing, Fort Worth, TX) in a 4:1 base:plasticizing agent mix thermally bonded to a rigid acrylic core. The composite roller has an outer radius of 9.525 mm. As discussed in Chapter 4, along with full derivation in Appendix A, PVC is roughly two orders of magnitude softer than the PDMS. It can be described in the linear regime with an initial modulus E_0 of 18.6 kPa, or can be more fully characterized using a second-order polynomial hyperelastic model with an initial modulus E_0 of 25.2 kPa. The soft indenter was subsequently subjected to two modes of contact: free rolling and sliding contact.

Tribometer

To observe the effect of our manufactured mesopillars, the resulting pillar forms were tested using a purpose-built benchtop tribometer of our own design (Figure 5.6. A full discussion of the design and validation of the tribometer is discussed in Chapter 3 or [43]. To briefly reiterate, the device is a three degree-of-freedom (DOF) tribometer. The indenter is brought into contact with the substrate under conditions of either fixed indentation (by means of a dial micrometer) or fixed force (via application of a counterweight to the opposing end of a fulcrum), and translated across the substrate at a fixed velocity to a distance specified by the user. Translational velocity is achieved via a proprietary PID motor-controller driving a DC-servo motor attached to a lead screw. The indenter may then be allowed to rotate freely to observe rolling contact, or it may be fixed if shearing behavior is desired.

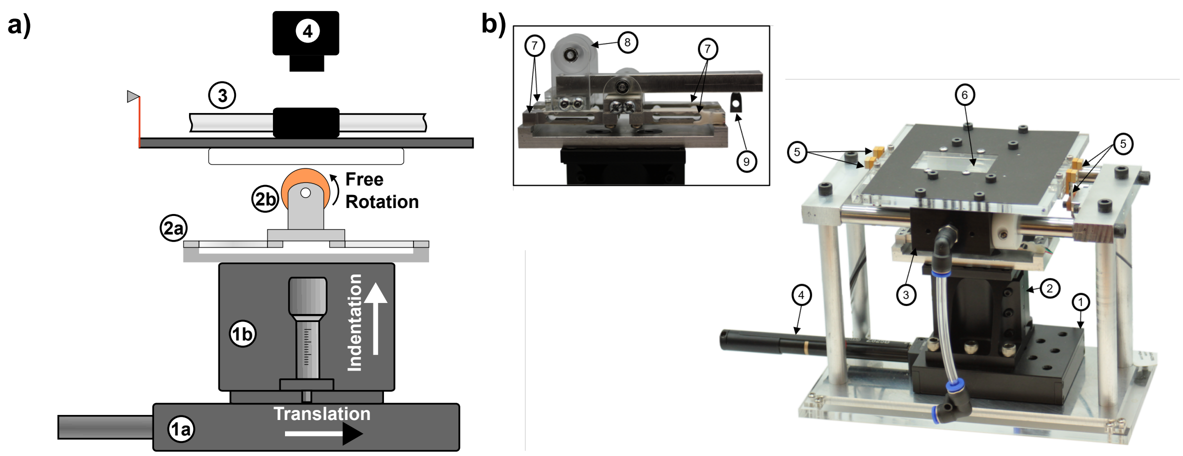

Figure 5.6: **(a)** Schematic showing major components of the tribometer: **(1a)** horizontal translation stage, **(1b)** vertical positioning, **(2a)** normal force sensing, **(2b)** rolling indenter, **(3)** frictionless stage and tractive force sensing, and **(4)** camera for contact area imaging. **(b)** As-built picture of the tribometer: **(1)** horizontal and **(2)** vertical stages, **(3)** frictionless air bearings, **(4)** DC servo motor and lead screw, **(5)** tractive force load cells, **(6)** substrate mount. **(inset)** Indenter housing configured for force control expirments: **(7)** normal force load cells, **(8)**, rolling indenter, and **(9)** counterweight attachment point.

Because of the difficulty in establishing an initial point of contact in soft materials and micro-textured surfaces, we chose to conduct force-controlled experiments. For consistency of results, all indenter and substrate concentrations were subjected to the same test conditions: an applied counterweight of 20 grams (196 mN) and a translational velocity of 0.1 mm/s. Each indenter/substrate combination was subjected to ten individual tests - the tests were unidirectional, and the indenter and substrate were separated as the translational stage returned to its starting position.

During each test run, video was captured of the contact area. Because most of the experiments involved contact with micro- or mesopillars, the video data was not used to extract and quantify the extent of the contact area, but was instead used to identify qualitative aspects of the contact, most notably the extent of pillar bending.

Data Collection and Analasysis

During each trial run, normal and tractive data is collected in real-time via load cells. Tractive force was collected via a single thin-beam full-bridge load cell (OMEGA LGL-227G) with a 250-g capacity. Normal force data was collected using an array of four 100-g load cells mounted below the indenter housing. The voltage signals for each channel were collected via a DAQ and converted to force values in the CPU. The normal force signals were averaged to a single force value and post-processed to account for the added moment of the tractive force at the indenter/substrate interface. The force data from each set of experiments was then smoothed using a linear regression with a window of approximately 200 ms (examples of recorded tractive force are shown in Figure 5.13). An appropriate equilibrium window of 20-140 s was deemed appropriate for all test conditions. From that window, the mean normal force was calculated, as well as either the mean tractive force, or mean peak tractive force, as appropriate, a distinction which will be discussed in Section 5.4.

To determine the efficacy of the pillar geometries, the tractive forces for each geometric configuration were compared using a one-way Analysis of Variance (ANOVA) test with a value of $p = 0.05$ to determine a significant difference of means between the flat substrate and each pillar configuration. The resultant analyses are shown for each case in Figures 5.10, 5.11, and 5.12 and discussed in Section 5.4.

5.4 Results and Discussion

5.4.1 Mesopillar Geometry

3D Printing

Using 3D printed molds, we were able to manufacture pillars at three aspect ratios - 1:1, 2:1, and 4:1, in both the circular (Figure 5.7) and goldfish (Figure 5.8) configurations. As can be seen

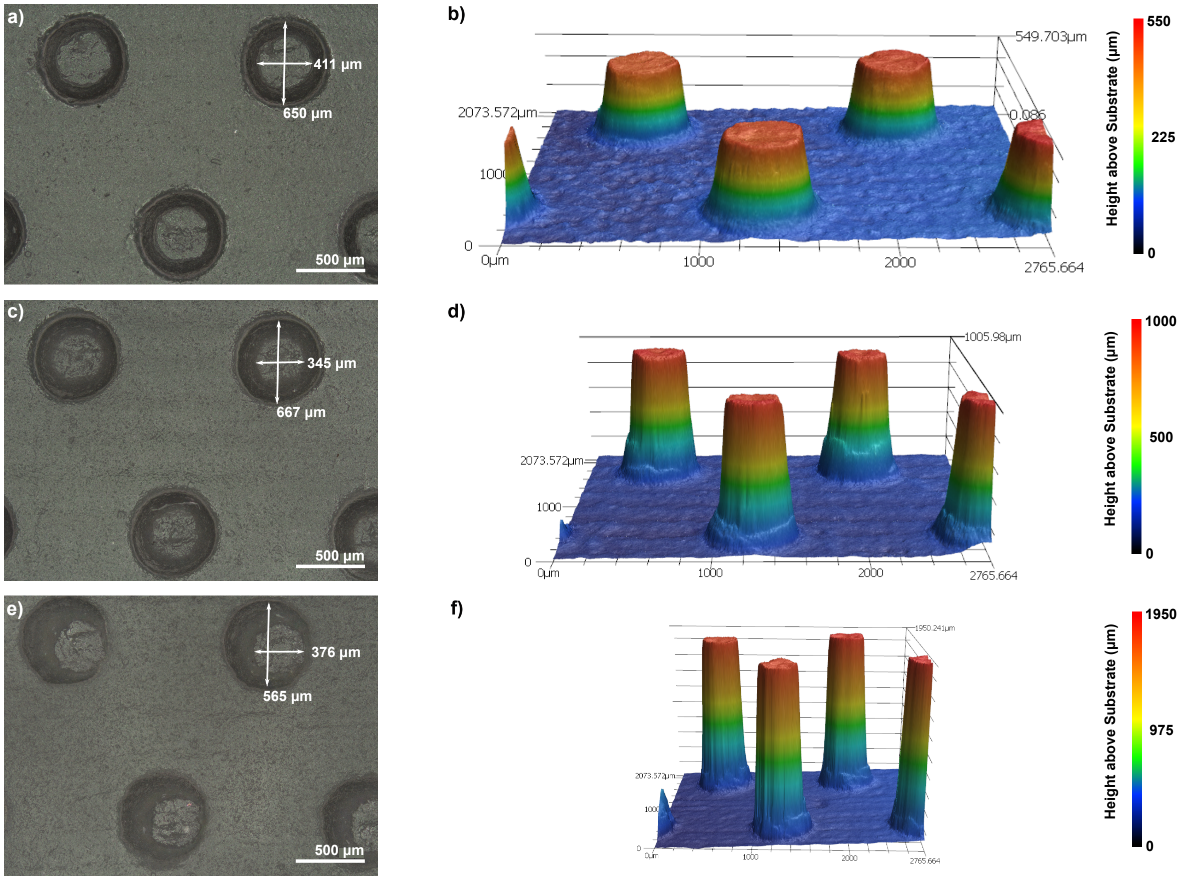

Figure 5.7: The images on the left are optical microscopy scans of mesopillars formed using 3D printed molds, while the images on the right are height profiles of the same taken from a focus variation scanning profilometer. Figures **(a-b)**, **(c-d)**, and **(e-f)** represent pillars at aspect ratios of 1:1, 2:1, and 4:1, respectively. The 3D printing process loses some degree of verticality, as the bases at all heights are larger than the desired 500 µm and the tops are smaller, an effect more pronounced on the taller pillars. The deviation of the pillar height from the desired also increases with height, from roughly 25 µm at the shortest to 120 µm at the tallest.

from Figure 5.7, the 3D printing process does not create perfectly monolithic mesopillars, as the base of the pillars is slightly larger than the desired diameter of 500 µm, with values of 658 $\pm$ 32, 667 $\pm$ 40, and 565 $\pm$ 35 µmin order of increasing aspect ratio. Additionally, the tops of the pillars are slightly smaller than the desired diameter, with top diameters of 476 $\pm$ 7, 344 $\pm$ 29, and 377 $\pm$ 12 µm arranged by aspect ratio. This is likely attributable to the 3D printing process itself, with the wider bases caused by excess resin curing in the transition from a level surface to the base of a mesopillar. Likewise, the narrowing likely occurs due to printer resolution - finite limitations on resolution restrict the actual diameter printed. And because each layer must be bonded to its predecessor, this lack of resolution is compounded for taller structures. The manufactured pillars were also somewhat shorter than intended, with average heights of 476 $\pm$ 7, 907 $\pm$ 35, and 1838 $\pm$ 52 µm for intended heights of 500, 1000, and 2000 µm respectively. At the lowest height, this is attributable to printer resolution, as the intended and actual heights are within the stated resolution of the Formlabs printer (25 µm). The increased disparity at the higher aspect ratios is likely a function of both printer resolution and surface tension - although the PDMS was degassed in a vacuum after being poured into the molds, surface tension likely led to a higher degree of air entrapment in the taller molds.

The goldfish molds (Figure 5.8) exhibited similar height and major diameter trends as those observed for the circular pillars. For the goldfish molds, an additional measure of interest was the sharpness of the terminal points for the concave sides - as friction and adhesion are both areal phenomena, the degree of sharpness, as it would ultimately affect the amount of contact area, should have a noticeable effect on tractive force. Because the printer has a finite resolution of 25 µm, it was not expected that singular points would be achieved, and that proved to be the case. The average "fin" radii for the goldfish mesopillars were 57 $\pm$ 8, 43 $\pm$ 6, and 39 $\pm$ 2 µm at 1:1, 2:1, and 4:1 aspect ratios, respectively. Interestingly, it appears that the same phenomenon that limits the overall verticality of the pillars also leads to sharper terminals at higher aspect ratios.

A final consideration for our rapid manufacturing technique is the surface roughness of the pillar tops. Much research has been devoted over the past two decades to the effect of surface roughness on contact mechanics and adhesion [70, 91, 81, 69]. Briefly, at the interface between two bodies, surface roughness leads to incomplete contact limited to aspersions and some interstitial areas. Because adhesion is an areal phenomenon, the difference between real and apparent contact areas affects the overall adhesion between the two bodies. Although this is negated somewhat in the case of highly-deformable materials, it must still be considered.

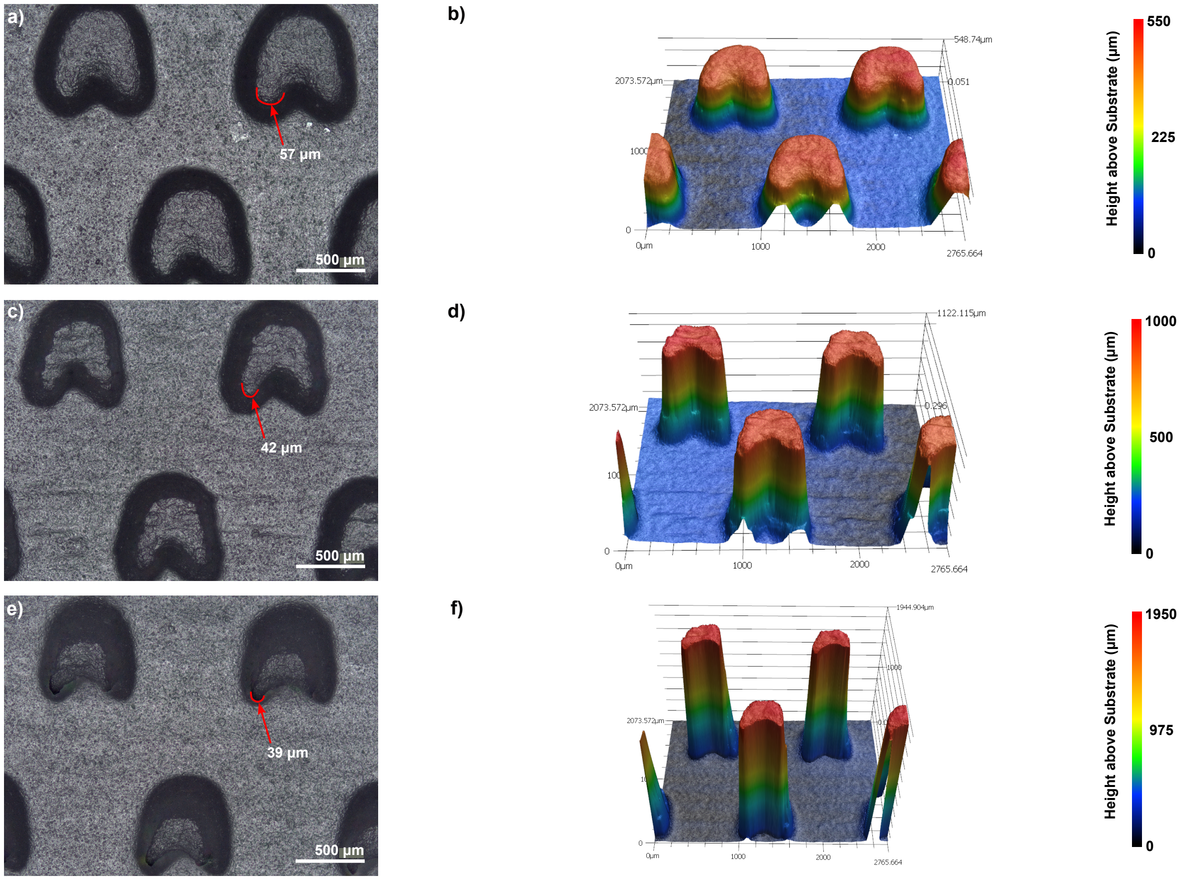

Figure 5.8: The images on the left are optical microscopy scans of goldfish mesopillars formed using 3D printed molds, while the images on the right are height profiles of the same taken from a focus variation scanning profilometer. Figures **(a-b)**, **(c-d)**, and **(e-f)** represent pillars at aspect ratios of 1:1, 2:1, and 4:1, respectively. The 3D printing process loses some degree of verticality, as the bases at all heights are larger than the desired 500 µm and the tops are smaller, an effect more pronounced on the taller pillars. Limited by the resolution of the printer (25 µm), the "fins" at the termini of the concave side could not reach a singular point, but the radii do appear to tighten as the aspect ratio is increased.

Laser Engraving

Unlike 3D printing, laser engraving does not allow the arbitrary assignment of pillar heights. Instead, the height of the pillars is achieved through the tuning of engraving parameters within the printer control software, specifically the laser power, printhead speed, and number of passes to which the print job is subjected. To narrow the design space, we sought to achieve our desired aspect ratios by fixing all parameters save one, in this case the printhead speed. To achieve three aspect

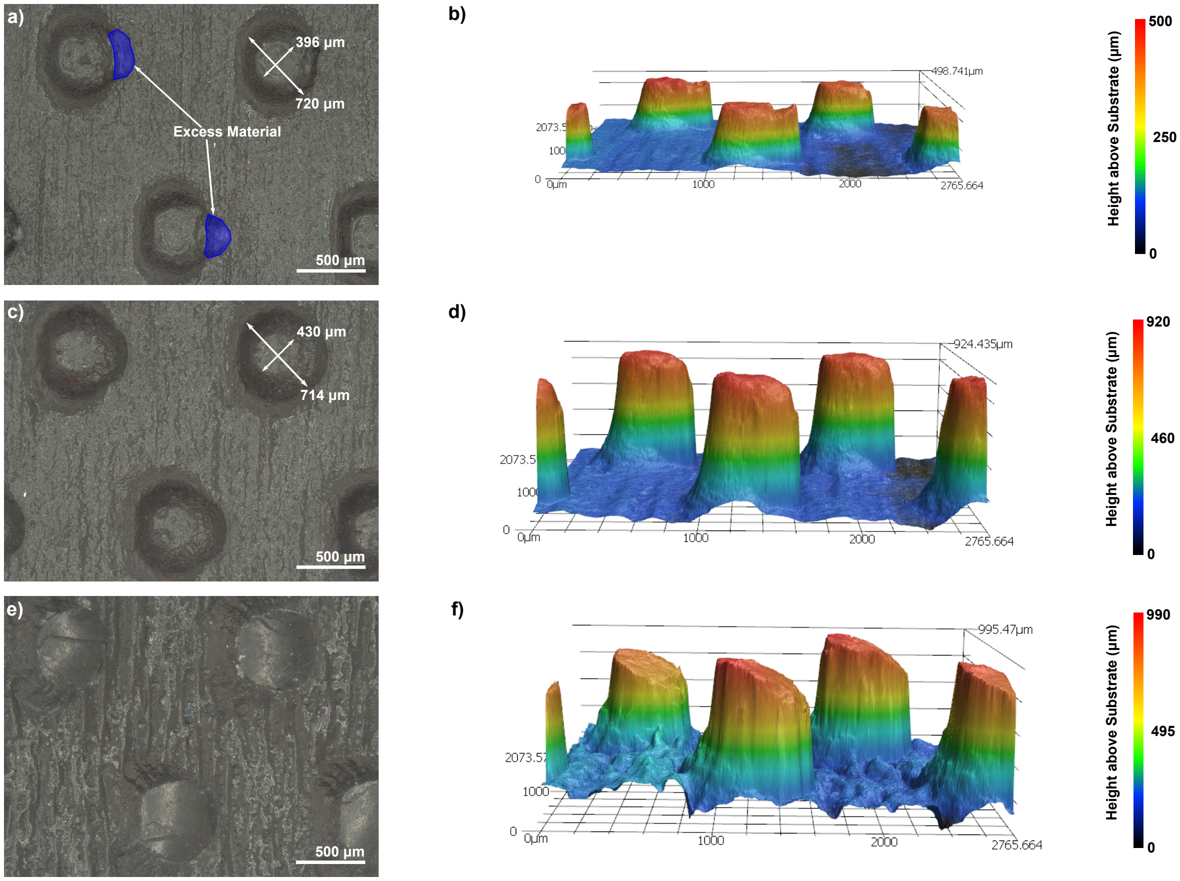

Figure 5.9: The images on the left are optical microscopy scans of circular mesopillars formed using laser engraved molds, while the images on the right are height profiles of the same taken from a focus variation scanning profilometer. Figures **(a-b)**, **(c-d)**, and **(e-f)** represent pillars at aspect ratios of 1:1, 2:1, and 4:1, respectively. The laser engraving process suffers greater loss of verticality than the 3D printing process, as remnant ablated material is remelted during subsequent passes, which also tends to create overhangs of excess material, as highlighted in Figure **(a)**. This overhanging material likely led to the failure of the 4:1 aspect ratio pillars **(e-f)** to separate from the mold, causing them to shear off at roughly 900 µm.

ratios, we used printer speeds of 17.75, 35.5, and 71 cm/s (speeds are programmed as percentages of the maximum speed of 355 cm/s). As can be seen in Figure 5.9, these settings reached aspect ratios comparable to the 3D prints for the lower two aspect ratios, with average heights of 390 $\pm$ 15 and 812 $\pm$ 25 µm respectively. As will be discussed below, the tallest pillars failed to separate from the mold.

A primary drawback of the laser engraving process is the difficulty in removing abraded material from the print area. Recently abraded acrylic forms a fine powder - although the printer uses forced air to remove particulates from the print area, it was not able to fully remove material from the small interstitial spaces between the mesopillars. Remnant material could then potentially be melted back onto the mold during subsequent print lines. This led to two observed outcomes in the molded pillars. First, the laser engraved pillars were more obviously sloped than the 3D printed pillars, with bases of 721 ± 37 and 714 ± 21 µm and tops of 396 ± 52 and 432 ± 23 µm at aspect ratios of 1:1 and 2:1 respectively. Secondly, the molds and subsequently the molded pillars, tended to accumulate overhangs of re-accumulated material on one side. For the shorter pillars, this affected the overall geometry of the pillar top; for the tallest pillars, we believe this accumulation of material caused the pillars to fail to separate from the mold, as they all sheared off at roughly 950 µm (see Figure 5.9f).

As with the 3D printing process, we were also concerned with the surface roughness of our molded pillars. As discussed in Chapter 4, and shown again in Figure 5.2, the ablative nature of the laser etching/engraving process can have marked effects on the surface of the pillars. Because we were creating positive molds and thus engraving the space around the pillars, we were uncertain about the overall effect on the pillar tops. However, as can be seen clearly in Figure 5.9, the heat from the engraving process was sufficient to substantially affect the surface roughness of the tops and sides of the pillars.

Analysis of the laser engraved goldfish was not conducted because the accumulated material in the concavity was prevalent enough to negate any potential shape factors.

5.4.2 Experimental Results

To test the effectiveness of the selected geometric parameters, as well as the two manufacturing processes, the experimental results for each shape/aspect ratio combination were pooled and compared using a one-way ANOVA test. A Tukey Test with a significance value of $p = 0.05$ was used to determine if populations represented a statistically significant difference in means. For clarity, the populations are grouped and plotted by manufacturing method, but all were compared back against both the flat substrate and laser-etched micropillar substrate, shown as gray and red boxplots, respectively, in all plots. Each contact method (rolling rigid indenter, rolling soft indenter, and shearing soft indenter) were considered separately, and through-running trends are considered below as appropriate.

Rigid Rolling Indenter

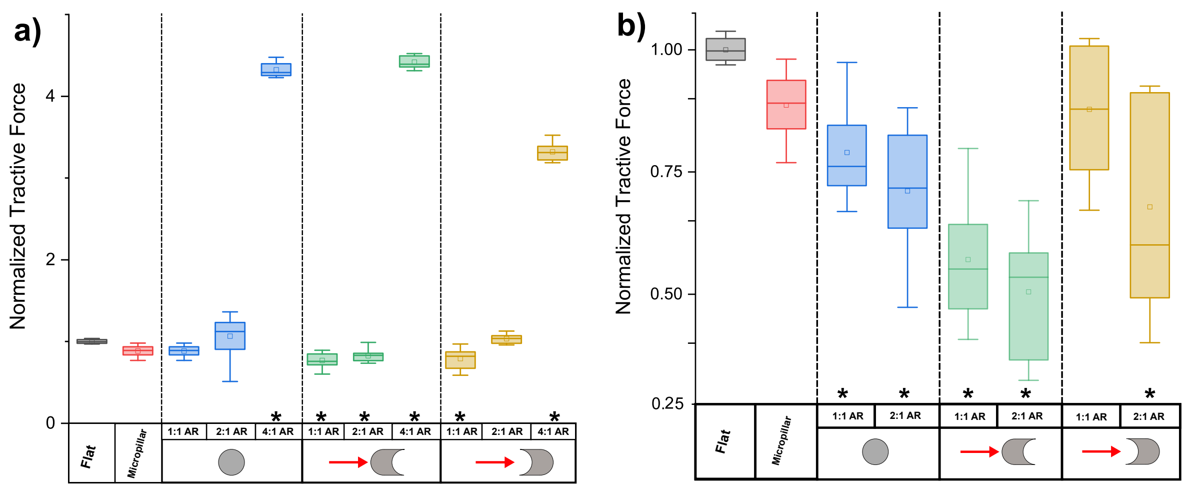

Figure 5.10: Comparison of the tractive force for the rigid, rolling indenter with **(a)** 3D printed and **(b)** laser engraved mesopillars. The tractive force values are normalized to the mean of the flat substrate tractive force results. In general, it is observed that, in the absence of pillar bending, pillared substrates, both micro and meso, tend to lower the tractive force, likely due to decreased contact area. However, at the highest aspect ratio, pillar bending leads to a significant increase tractive force. It is also noteworthy that direction of contact plays a significant role in the behavior of the goldfish pillars. Because the laser-engraved pillars could not be manufactured above a 2:1 aspect ratio, no bending was observed, but all other trends are similar (note the difference in scale).

The measured tractive force for the rigid rolling experiments is shown in Figure 5.10a. Before discussing the results, a brief explanation of the plot is appropriate, and will apply to all subsequent plots. The tractive force values depicted are normalized to the mean of the tractive force for the flat substrate experiment. The limits of each box represent the 25th and 75th percentiles, with whiskers representing the range of values. The mean is depicted by a small internal square, and median by the horizontal bar. Outliers, such as they were identified, are shown as solid diamonds. For all plots, the gray and red boxes represent the flat and micropillared substrates, respectively. Blue boxes denote circular mesopillars, while green denotes goldfish oriented with the convex face leading contact and gold denotes goldfish oriented with the concave face towards the leading edge of the indenter. Asterisks denote a statistically significant difference in means between that population and the flat substrate. It should also be noted that, for every contact case, pillar bending was observed only for the 4:1 aspect ratio pillars.

Because the indenter is rigid and nominally smooth, it was expected that the tractive force would decrease due to the decreased real contact area, both at the macro level due to the presence of pillars and micro level due to surface roughness, and this matched with observations for those pillars which did not bend. However, for the high aspect ratio pillars, it was noted that the onset of pillar bending led to a significant increase in the tractive force, increasing by roughly a factor of four. It should also be noted that, using the same ANOVA criteria, there is no significant difference between the indenter encountering a tall circular pillar or the convex face of a goldfish. Contact with the concave side, however, leads to a significant decrease as compared to the circular pillar.

Because we were not able to create laser-engraved mesopillars higher than 1000 µm, similar bending effects could not be observed. However, at the lower aspect ratios, the tractive behavior (Figure 5.10b) was similar to their 3D printed counterparts. The difference in scale must be considered when comparing the two plots.

Soft Rolling Indenter

As was the case with the rigid rolling indenter, it is apparent (Figure 5.11a) that pillar bending has a significant effect on contact mechanics, as the 4:1 aspect ratio pillars create an almost three-fold increase in tractive force. Also similar to the rigid indenter, the goldfish mesopillar behaves almost identically to the circular mesopillar when contact is initiated from the convex side, while the tractive force is significantly reduced when contacted from the concave side. This again suggests that the extent of contact area plays a key role in the tractive force for this type of contact. A difference between soft and rigid rolling is that, for the most part, the presence of mesopillars tends to increase the tractive force, often more so than the presence of micropillars, although not necessarily to a statistically significant amount. This appears to hold true for all goldfish pillars,

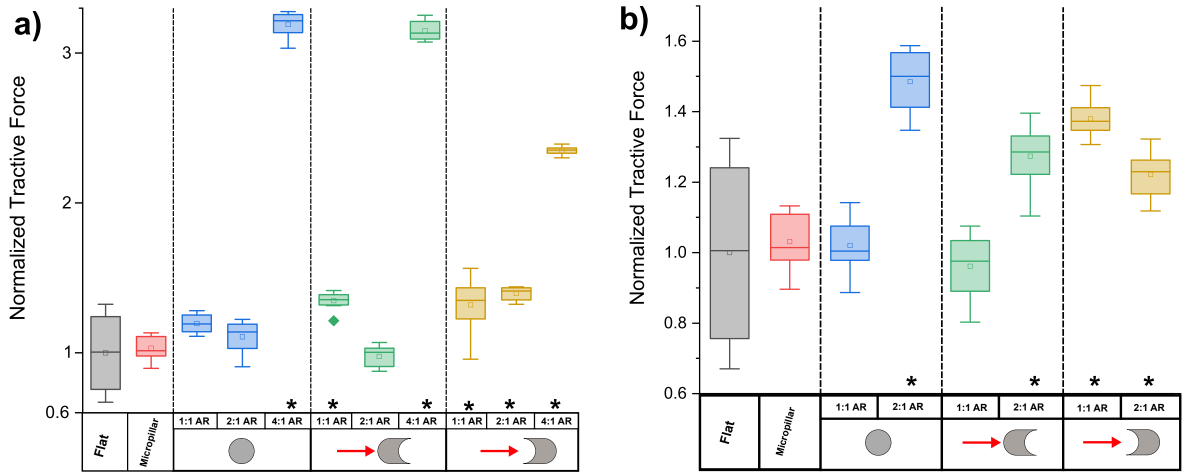

Figure 5.11: Comparison of the tractive force for the soft, rolling indenter with **(a)** 3D printed and **(b)** laser engraved mesopillars. The tractive force values are normalized to the mean of the flat substrate tractive force results. As with the rigid rolling indenter (Figure 5.10, the presence of pillar bending leads to a significant increase in tractive force, which is again directionally specifice in the goldfish pillar. Because the laser-engraved pillars could not be manufactured above a 2:1 aspect ratio, no bending was observed, but all other trends are similar (note the difference in scale).

and for all the laser engraved pillars at a 2:1 aspect ratio. This could be caused by taller pillars reducing significantly or eliminating backing layer contact and giving rise to previously documented phenomena such as contact splitting []. However, given the high degree of surface roughness, it is most likely that some as-yet identified aspect of their respective geometries makes them more effective as grousers when interacting with the soft PVC shell of the roller.

Soft Shearing Indenter

For the final series of experiments, the soft shell indenter was fixed to prevent rotation so as to observe the effects of pillar geometry in the case of soft material shearing. The results are depicted in Figure 5.12. This contact scenario is particularly interesting in that the tractive behavior between different mesopillar aspect ratios was most obviously distinct, as shown in Figure 5.13. Figure 5.13a, depicting the contact between the indenter and flat substrate, clearly shows rapid fluctuations indicative of stick-slip behavior. Transitioning to the mesopillars of 1:1 or 2:1 aspect ratios, typified by Figure 5.13b, clearly distinct peaks and valleys are formed, indicating

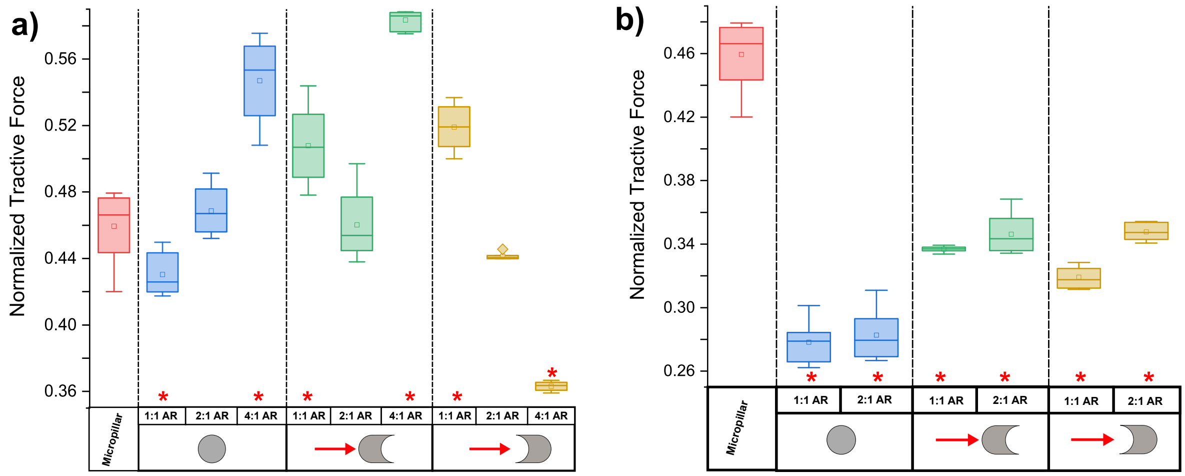

Figure 5.12: Comparison of the tractive force for the soft, sheared indenter with **(a)** 3D printed and **(b)** laser engraved mesopillars. Experimental observations indicate that the presence of features of any size reduces the frictional force between substrate and indenter (to preserve scaling on the graph, the flat substrate box is omitted). Because all surfaces were significantly below the flat substrate, we chose instead to compare mesopillars to the micropillared substrate. Thus, the red asterisks represent a significant difference in mean from the micropillared sample. The difference in manufacturing method was most pronounced in this contact scenario, as the 3D printed mesopillars in general created an increase in tractive force, while the laser engraved mesopillars tended to decrease tractive force. This could be caused by the more pronounced slope of the laser-engraved pillars, or to the increased surface roughness on the leading edges creating a decrease in real contact area.

periods of maximal and minimal contact between the indenter and the unbending pillars. Finally, with high aspect ratio pillars (Figure 5.13c), we see the fluctuation between peak and valley is greatly attenuated, implying that the bending of the pillars leads to more consistent contact as the indenter is sheared across the substrate.

Contrary to the previous experiments, the results from the soft shearing experiments indicate that the presence of texturing at any scale reduces the frictional force between indenter and substrate. Because the tractive force for all surfaces was well below the flat substrate, for this scenario we chose to compare our mesopillars against the micropillared substrate. Doing so, we see that pillar bending still contributes most significantly to the tractive force, although the effect is not as pronounced in this case as with the rolling cases. It should also be noted that the raw tractive forces in the sliding case are roughly an order of magnitude higher than the rolling case, which may explain the difference. Additionally, in the case of the goldfish pillar, the difference in tractive force is such that it actually decreases the tractive force relative to the flat control. Sliding contact also appears to be the only case in which manufacturing method plays a significant role, as the 3D printed mesopillars tend to increase tractive force, while the laser engraved mesopillars lead to a decrease. We believe that the fact that all textures reduce friction from the flat substrate, and that laser engraved pillars do so to a greater extent highlights the fact that surface roughness and the subsequent reduction in real contact area, plays a significant role in the friction between soft materials, which aligns with the findings of [39].

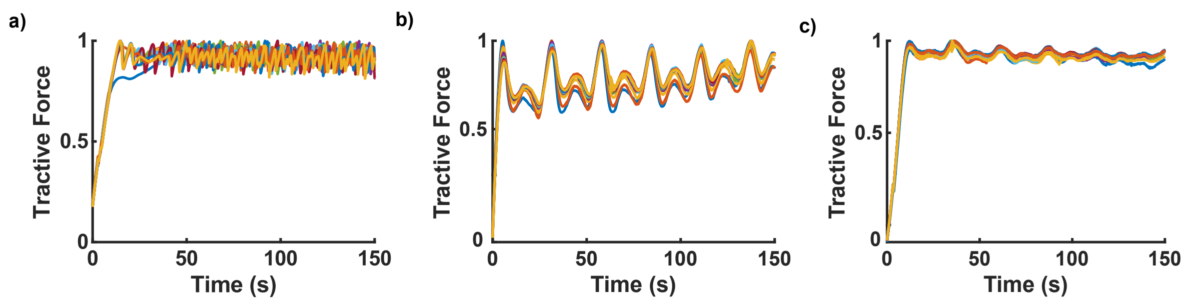

Figure 5.13: Generalized tractive force behavior observed while shearing a soft shell indenter across various substrate geometries. With a flat substrate **(a)**, the tractive force fluctuates comparatively rapidly, indicative of stick-slip behavior. With 1:1 or 2:1 aspect ratio mesopillars, **(b)**, very distinct peaks and valleys are observed, indicating separate periods of maximal and minimal contact as the indenter encounters the more rigid pillars. Finally, with high aspect ratio pillars **(c)**, the peak and valley fluctuation is greatly attenuated, implying that the bending of the pillars leads to more consistent contact across the length of travel. The tractive force values are normalized against their maximum values to better show qualitative differences.

Considering the experimental results holistically, it is apparent that the bending stiffness of individual pillars can have a significant impact on the contact mechanics between two surfaces for both rolling and sliding contact. Further, the geometry of the leading edge of contact, at least in such cases where pillar bending is induced, further influences the overall tractive force between substrate and indenter. Moreover, the significance role of pillar bending highlights the utility of our meso-scale prototyping techniques. Although the manufacture of varying aspect ratio pillars is almost trivial for our methods (particularly 3D printing), doing so with the conventional micromanufacturing techniques described above would be anything but. For a photolithographic mold, each new aspect ratio would likely require the development through trial-and-error of a unique mold-making protocol, requiring days or weeks in a cleanroom. Likewise, a laser-etched negative mold would reach an effective height limit beyond which the accumuluation of material in the pillar spaces would render the subsequent pillars so geometrically different from monolithic pillars as to be unusable from a research perspective.

5.5 Conclusion

Although the overall body of research on microstructured surfaces is well-established, the application of structured surfaces with soft, deformable substrates is comparably nascent. Although the efficacy of microstructured surfaces in tuning the contact mechanics has been demonstrated both from an adhesional [54] and frictional [56] standpoint, as well as demonstrated practically in both robotic capsule endoscopes (RCEs) [25] and balloon endoscopy [14] (to cite specific examples), much opportunity still exists both in developing descriptive models for this type of contact and in optimizing pillar geometries for specific applications. To accomplish either efficiently, researchers have the option to either develop accurate numerical models or to conduct experiments using prototyped structures. Using the techniques described in this work, researchers could rapidly navigate a given design space incorporating multiple pillar geometries, orientations, and aspect ratios in a comparatively short amount of time.

Using this work as a small example of the same, we have investigated two techniques, 3D printing and laser engraving, incorporating technologies that are conceivably already available to most researchers in their own lab or a readily-accessible shared-use facility, and used those techniques to develop sub-millimeter mesoscale pillar geometries. Moreover, we have shown that at least one technology, 3D printing, could develop those mesopillars in an array of aspect ratios limited only by the material stiffness of the pillars themselves, and have shown through experimental observation that the subsequent bending stiffness of the pillars produced plays a significant rolling in both rolling and sliding contact mechanics.

Chapter 6

Conclusions

The conclusions of this work, separated into individual research aims, are listed below.

Aim 1

- The design and construction of a benchtop tribometric device capable of quanitifying the normal and tractive forces involved in adhesive rolling contact, correlated in time to contact area imaging to fully characterize the rolling contact between elastomeric surfaces.

- The experimental validation of said tribometer using a rigid, nominally-smooth acrylic indenter and a flat Poly(dimethylsiloxane) (PDMS) substrate. Experimental results were validated against predicted values from both Hertz and Johnson-Kendall-Roberts (JKR) contact theories.

- Demonstration of the device's utility by changing the experimental setup to incorporate a rolling indenter comprised of a thin (3 mm) shell of highly-deformable Poly(vinyl Chloride) (PVC) bonded to a rigid acrylic core, demonstrating both the effects of rate-dependent surface effects and finite-thickness factors in contact.

Aim 2

- The characterization of the rolling contact between a PDMS substrate and a rolling indenter comprised of a thin PVC shell surrounding a rigid core.

- Experimental observations at various translational speeds and imposed normal forces used to correlate data to a predictive model relating tractive force to both speed (due to rate-dependent surface effects) and normal force (due to partial slip conditions)

- Development of a 2D numerical model to develop finite thickness correction factors for cylindrical contact and to demonstrate the contributions of both adhesion and friction to the overall tractive force.

- Experimental observations of same indenter but replacing the flat PDMS substrate with consisting of micropillars formed using a laser-etched Kapton mold. It was determined that the change in rolling contact mechanics due to the presence of micropillars was very modest, likely due to the extent of backing layer contact in the interstitial layers between the micropillars.

Aim 3

- The development of two novel manufacturing techniques (3D Printing and Laser Engraving) to develop sub-millimeter scale "mesopillars" using commercially-available technologies that could reasonably be considered available to most researchers either in their own labs or in a shared-use facility.

- Using the aforementioned technologies, successfully manufactured mesopillars of two distinct geometries (circular pillars and "goldfish") and, in the case of 3D printing, achieved pillars in three aspect ratios ranging from 1:1 to 4:1.

- Through experimental observation, determined that the presence of mesopillar bending at the interface significantly affects the tractive force for both rolling and sliding contact, an effect that can be further altered by the geometry of the leading edge of contact in bending pillars.

Chapter 7

Discussion

In this work, I have described our efforts to better understand the complex phenomena contributing to the rolling contact of soft elastomers with engineered surfaces and, in doing so, have hopefully outlined the challenges involved in characterizing the contact mechanics of highly deformable materials. High deformability, rate-dependent effects, finite thickness concerns, and the interplay of adhesion and friction pose myriad challenges to researches attempting to understand the behavior of these materials. Despite the challenges, the range of potential applications, from wearable devices and medical robotics to soft robotics, offer compelling reasons to advance this field of scientific inquiry.

A primary challenge to researchers and designers alike is that, because of advances in manufacturing technologies, the pillar morphology space is effectively limitless, with the ability to alter materials, heights, geometries, and orientations to name but a few. Advancing research in this field, then, becomes a matter of narrowing or more efficiently navigating that space. To do so, researchers have two primary options - either to combine efficient prototyping methods and experimental procedures to test an array of morphologies and identify trends, or to develop effective numerical models that can efficiently and accurately predict the behavior of proposed morphologies. To that end, we have developed and described an experimental method to quantify the contact mechanics of soft materials that can adapt relatively easily to various load conditions, substrate and indenter geometries, and velocities, and have combined that experimental method with two potential rapid prototyping techniques using equipment that could reasonably considered available to most researchers in the field today. Moreover, we describe efforts toward a numerical method to quantify rolling contact mechanics, although this method ultimately fell short of our goal to extend the method towards novel geometries such as micro- and mesopillars.

Regarding further development of our tribometer and associated experimental techniques, there is still a great deal of potential in contact area imaging and quantification. Contact area is a key physical quantity regarding rolling contact and cylindrical contact in general, and the extent of backing layer contact appears to play a crucial role in the contact mechanics of textured surfaces. Our device proved entirely sufficient in identifying the contact area for flat substrate experiments, although automation of the process would greatly improve the efficiency of analysis, and was also able to identify the bulk contact areas of textured surfaces as well as capture mesopillar phenomena such as pillar bending. However, the actual determination of contact area for such scenarios was largely qualitative. Improved imaging hardware and procedures, as well as post-processing techniques involving machine vision could better identify the true contact area, which could then be more effectively correlated to recorded forces.

The next logical step in mesopillar experimentation would be to conduct *ex vivo* or *in vivo* tests on actual biological tissue. Although the PVC used in our experiments is an adequate tissue mimic from a mechanical standpoint, the use of nominally flat, unlubricated surfaces limits our ability to accurately claim pillar efficacy, given that the actual operating environments will exhibit surface fluctuations at both the macro- and microscopic scales [60, 26], as well as the presence of mucosal or fluid layers [83]. These factors will undoubtedly affect the efficacy of proposed pillar morphologies.

Regarding our proposed prototyping techniques, two avenues of further development are readily apparent: application and manufacturing at scale. The fact that both prototyping techniques produce soft, flexible silicone mesopillar molds, these molds could easily be adapted to the production of PDMS treads for small-scale medical robotics, as described in [25] or in the production of texture enteroscopy balloons as presented in [14]. These devices have already been tested on biological tissues, so no further testing protocols would need to be developed. Manufacturing at scale remains difficult because of the need to degas material under vacuum for reliable mold infiltration and curing times to prevent feature collapse. Because both issues are largely unavoidable, scaling production will likely require advancements in the automation of batch processes to manufacture many units simultaneously.

There remains a great deal of potential in the simulation of contact with microtextured surfaces in general, and with rolling contact specifically. Current technologies pose a trade-off between accurate physical representation, as can be achieved through full-body 3D simulations, and computational tractability using 2D representational models. Concurrent advances in supercomputing throughput and application of machine learning algorithms could potentially negate this dilemma, but in the meantime, a potential bridging technique would be to develop 3D representative volume element (RVE) simulations that describe contact of a small cluster of microfeatures which can then be extrapolated to the entire contact area. Although already explored for indentation and retraction experiments [53], the extension to rolling contact would pose several interesting challenges regarding boundary conditions. Successful implementation of this technique could greatly accelerate the development and evaluation of novel pillar geometries tuned to various applications.

Continued development in this field holds the potential to greatly improve the interaction of robots, sensors, and electromechanical devices in general with soft, deformable materials, leading to potential improvements in the fields of medical robotics, delicate task handling, and food production automation.

Bibliography

[1] E. Arzt, S. Gorb, and R. Spolenak. From micro to nano contacts in biological attachment devices. Proc. Nat. Acad. Sci., 100:10603–10606, 2003.

[2] K. Autumn, S. T. Hsieh, D. M. Dudek, J. Chen, C. Chitaphan, and R. J. Full. Dynamics of geckos running vertically. J. Exp. Biol., 209:260–272, 2006.

[3] K. Autumn, Y. A. Liang, S. T. Hsieh, W. Zesch, W. P. Chan, T. W. Kenny, R. Fearing, and R. J. Full. Attachment force of a single gecko foot-hair. Nature, 405:681–685, 2000.

[4] K. Autumn and A. M. Peattie. Mechanisms of adhesion in geckos. Integr. Comp. Biol., 42:1081–1090, 2002.

[5] S. Baik, H. J. Lee, D. W. Kim, J. W. Kim, Y. Lee, and C. Pang. Bio-inspired adhesive architectures: From skin patch to integrated bioelectronics. Adv. Mater., 31:1803309–1–18, 2019.

[6] G. I. Barenblatt. The formation of equilibrium cracks during brittle fracture. J. Appl. Math. Mech., 23:622–636, 1959.

[7] G. I. Barenblatt. The mathematical theory of equilibrium cracks in brittle fracture. Adv. Appl. Math., 7:55–129, 1962.

[8] M. Barquins. Aherence and rolling kinetics of a rigid cylinder in contact with a natural rubber surface. J. Adhesion, 26:1–12, 1988.

[9] M. Barquins and D. Maugis. Tackiness of elastomers. J. Adhesion, 13:53–65, 1981.

[10] V. Barreau, R. Hensel, N. K. Guimard, A. Ghatak, R. M. McMeeking, and E. Arzt. Fibrillar elastomeric micropatterns create tunable adhesion even to rough surfaces. Adv. Func. Mater., 26:4687–4694, 2016.

[11] M. D. Bartlett, A. B. Croll, D. R. King, B. M. Paret, D. J. Irschick, and A. J. Crosby. Looking beyond fibrillar features to scale gecko-like adhesion. Adv. Mater., 24:1078–1083, 2012.

[12] L. F. Boesel, C. Greiner, E. Arzt, and A. del Campo. Gecko-inspired surfaces: A path to strong and reversible dry adhesives. Adv. Mater., 22:2125–2137, 2010.

[13] E. Bou-Chakra, J. Cayer-Barrioz, D. Mazuyer, F. Jarnias, and A. Bouffet. A non-newtonian model based on ree–eyring theory and surface effect to predict friction in elastohydrodynamic lubrication. Tribol Lett, 43:1674–1682, 2010.

[14] L. K. Bowen, K. Johannes, E. Zuetell, K. N. Calahan, S. A. Edmundowicz, R. Long, and M. E. Rentschler. Patterned enteroscopy balloon design factors influence tissue anchoring. J. Mech. Beh. of Biomed. Matls., 111:103966–1–13, 2020.

[15] G. Carbone and E. Pierro. Contact mechanics of mushroom-shaped adhesive structures. In L. Heepe, L. Xue, and S. N. Gorb, editors, Bio-Inspired Structured Adhesives: Biological Prototypes, Fabrication, Tribological Properties, Contact Mechanics, and Novel Concepts, pages 245–276. Springer, 2019.

[16] J. C. Charmet and M. Barquins. Adhesive contact and rolling of a rigid cylinder under the pull of gravity on the underside of a smooth-surfaced sheet of rubber. Intl. J. of Adhesion and Adhesives, 16:249–254, 1996.

[17] M. K. Chaudhury and M. J. Owen. Adhesion hysteresis and friction. Langmuir, 9:29–31, 1993.

[18] M. K. Chaudhury, T. Weaver, C. Y. Hui, and E. J. Kramer. Adhesive contact of cylindrical lens and a flat sheet. J. Appl. Phys., 80:30–37, 1996.

[19] V. Chauveau, D. Mazuyer, F. Dassenoy, and J. Cayer-Barrioz. In situ film-forming and friction-reduction mechanisms for carbon-nanotube dispersions in lubrication. Tribol Lett, 47:467–480, 2012.

[20] S. T. Chen. Fabrication of high-density micro holes by upward batch micro edm. J. Micromech. Microeng., 18:085002–1–9, 2008.

[21] P. Day, E. V. Eason, N. Esparza, D. Christensen, and M. Cutkosky. Microwedge machining for the manufacture of directional dry adhesives. J. Micro Nano-Manuf., 1:011001–1–10, 2013.

[22] B. V. Derjaguin, V. M. Muller, and Y. P. Toporov. Effect of contact deformations on adhesion of particles. J. Colloid Interface Sci, 53:314–326, 1975.

[23] D. S. Dugdale. Yielding of steel sheets containing slits. J. Mech. Phys. Solids, 8:100–104, 1960.

[24] W. Federle, W. J. P. Barnes, W. Baumgartner, P. Dreschler, and J. M. Smith. Wet but not slippery: boundary friction in tree frog adhesive toe pads. J. R. Soc. Interface, 3:689–697, 2006.

[25] G. A. Formosa, J. M. Prendergast, S. A. Edmundowicz, and M. E. Rentschler. Novel optimization-based design and surgical evaluation of a treaded robotic capsule colonoscope. IEEE Trans. on Robotics, 36:545–552, 2020.

[26] Y. Y. Fu, C. W. Lin, G. Enikolopov, E. Sibley, A. S. Chiang, and S. C. Tang. A microtome-free 3-dimensional confocal imaging method for visualization of mouse intestine with subcellular-level resolution. Gastroenterology, 137:453–465, 2009.

[27] K. Fuller and D. Tabor. The effect of surface roughness on adhesion of elastic solids. Proc. R. Soc. London, Ser. A, 345:327–342, 1975.

[28] K. N. G. Fuller and A. D. Roberts. Rubber rolling on rough surfaces. J. Phys. D: Appl. Phys., 14:221–239, 1981.

[29] H. Gao, X. Wang, H. Yao, S. Gorb, and E. Arzt. Mechanics of hierarchical adhesion structures of geckos. Mech. of Matls., 37:275–285, 2005.

[30] J. Gao, J. Zhao, L. Liu, and W. Xue. Dimensional effects of polymer pillar arrays on hydrophobicity. Surf. Eng., 32:125–131, 2016.

[31] S. M. Gernay, S. Labousse, P. Lambert, P. Compere, and T. Gilet. Multi-scale tarsal adhesion kinematics of freely-walking dock beetles. J. R. Soc. Interface, 14:20170493–1–16, 2017.

[32] N. J. Glassmaker, A. Jagota, C. Y. Hui, W. L. Noderer, and M. K. Chaudhury. Biologically inspired crack trapping for enhanced adhesion. Proc. Natl. Acad. Sci., 104:10786j–10791, 2007.

[33] P. Glick, S. A. Suresh, D. Ruffatto, M. Cutkosky, M. T. Tolley, and A. Parness. A soft robotic gripper with gecko-inspired adhesive. IEEE R.A. Letters, 3:903–910, 2018.

[34] S. Gorb, Y. Jiao, and M. Scherge. Ultrastructure architecture and mechanical properties of attachment pads in *Tettagoina viridissima* (orthoptera tettigoniidae). J Comp. Physiol. A, 186:821–831, 2000.

[35] S. Gorb and M. Scherge. Biological microtribology: Anisotropy in frictional forces of orthopteran attachment pads reflects the ultrastructure of a highly deformable material. Proc. R. Soc. Lond. B, 267:1239–1244, 2000.

[36] N. Gravish, M. Wilkinson, and K. Autumn. Frictional and elastic energy in gecko adhesive attachment. J. R. Soc. Interface, 5:339–348, 2008.

[37] A. A. Griffith. Vi. the phenomena of rupture and flow in solids. Phil. Trans. of the Royal Soc. London, Ser. A, 221:163–198, 1921.

[38] P. R. Guduru. Detachment of a rigid solid from an elastic wavy surface: Theory. J. Mech. and Phys. of Solids, 55:445–472, 2007.

[39] B. He, W. Chen, and Q. J. Wang. Surface texture effect on friction of a microtextured poly(dimethylsiloxane) (pdms). Tribol Lett, 31:187–197, 2008.

[40] Z. He, N. M. Moyle, C. Y. Hui, B. Levrard, and A. Jagota. Adhesion and friction enhancement of film-terminated structures against rough surfaces. Tribol Lett, 65:1–8, 2017.

[41] H. Hertz. On the contact of elastic solids. J. reine und angewandte Mathematik, 92:156–171, 1882.

[42] N. Hosoda, M. Nakamoto, T. Suga, and S. N. Gorb. Evidence for intermolecular forces involved in ladybird beetle tarsal setae adhesion. Science Reports, 11:7729–1–9, 2021.

[43] B. K. Hoyer, R. Long, and M. E. Rentschler. A tribometric device for the rolling contact of soft elastomers. Tribol Lett, 70, 2022.

[44] C. Y. Hui, N. J. Glassmaker, T. Tang, and A. Jagota. Design of biomimetic fibrillar interfaces: 2. mechanics of enhanced adhesion. J. R. Soc., Interface, 1:35–48, 2004.

[45] C. Y. Hui, A. Ruina, R. Long, and A. Jagota. Cohesive zone models and fracture. J. Adhes., 87:1–52, 2011.

[46] D. J. Irschick, C. C. Austin, K. Petren, R. N. Fisher, J. B. Losos, and O. Ellers. A comparative analysis of clinging ability among pad-bearing lizards. Biol. J. Linn. Soc., 59:21–35, 1996.

[47] A. Jagota and C. Y. Hui. Adhesion, friction, and compliance of bio-mimetic and bio-inspired structured interfaces. Mater. Sci. and Eng. R, 72:253–292, 2011.

[48] K. L. Johnson. Contact Mechanics. Cambridge University Press, Cambridge, UK, 1985.

[49] K. L. Johnson, K. Kendall, and A. D. Roberts. Surface energy and contact of elastic solids. Proc. R. Soc. London, Ser. A, 324:327–342, 1971.

[50] Y. Kameya. Wettability modification of polydimethylsiloxane surface by fabricating micropillar and microhole arrays. Matl. Lett., 196:320–323, 2017.

[51] M. Kamperman, E. Kroner, A. del Campo, R. McMeeking, and E. Arzt. Functional adhesive surfaces with "gecko" effect: The concept of contact splitting. Adv. Eng. Mater., 12:335–348, 2010.

[52] K. Kendall. Rolling friction and adhesion between smooth solids. Wear, 33:351–358, 1975.

[53] M. D. Kern, R. Long, and M. E. Rentschler. A rpresentative volume element model for the adhesion between a micropillared surface and a compliant substrate. Mech. of Matls., 119:65–73, 2018.

[54] M. D. Kern, Y. Qi, R. Long, and M. E. Rentschler. Characterizing adhesion between a micropatterned surface and a soft synthetic tissue. Langmuir, 33:854–864, 2017.

[55] J. Kim, J. W. Kim, H. C. Kim, L. Zhai, H. U. Ko, and R. M. Muthoka. Review of soft actuator material. Intl. J. of Prec. Eng. & Manu., 20:2221–2241, 2019.

[56] J. Kwon, E. Cheung, S. Park, and M. Sitti. Friction enhancement via micro-patterned wet elastomer adhesives on small intestinal surfaces. Biomed. Mater., 1:216–220, 2006.

[57] J. K. A. Langowski, D. Dodou, M. Kamperman, and J. L. van Leeuwen. Tree frog attachment: Mechanisms, challenges, and perspectives. Frontiers in Zoology, 15:1–21, 2018.

[58] S. H. Lee, C. W. Park, and M. K. Kwak. Continuous fabrication of wide-tip microstructures for bio-inspired dry adhesives via tip inking process. J. Chem., 2019:4827918–1–5, 2019.

[59] W. Li, B. Belmont, and A. Shih. Design and manufacture of polyvinyl chloride (pvc) tissue mimicking material for needle insertion. Procedia Manufacturing, 1:866–878, 2015.

[60] V. Mahadevan. Anatomy of the small intestine. Surgery, 32:391–395, 2014.

[61] D. P. Manning, J. E. Cooper, I. Stirling, C. M. Jones, M. Bruce, and P. C. McCausland. Studies on the footpads of the polar bear (ursus maritimus) and their possible relevance to accident prevention. J. Hand Surg. Brit. and Euro. Vol., 10:303–307, 1985.

[62] A. Milionis, I.S. Bayer, D. Fragouli, F. Brandi, and A. Athanassiou. Combination of lithography and coating methods for surface wetting control. In S. Hosaka, editor, Updates in Advanced Lithography. InTech Open, 2013.

[63] M. J. Moon, J. G. Park, and W. J. Choi. Fine structural analysis of fibrillar adhesion apparatus in ladybird beetle. Entomological Research, 42:196–205, 2012.

[64] N. Moyle, Z. P. He, H. B. Wu, C. Y. Hui, and A. Jagota. Indentation versus rolling: Dependence of adhesion on contact geometry for biomimetic structures. Langmuir, 34:3827–2827, 2018.

[65] C. V. Ngo, G. Davaasuren, H. S. Oh, and D. M. Chun. Transparency and superhydrophobicity of cone-shaped micropillar array textured polydimethylsiloxane. Intl. J. Precis. Eng. Manuf., 16:1347–1353, 2015.

[66] R. D. O'Rorke, T. W. J. Steele, and H. K. Tayor. Bio-inspired fibrillar adhesives: a review of analytical models and experimental evidence for adhesion enhancement by surface patterns. J. Adh. Sci. and Tech., 30:362–391, 2015.

[67] K. Park and G. H. Paulino. Cohesive zone models: a critical review of traction-separation relationships across fracture surfaces. Appl. Mech. Rev., 64:060802–1–20, 2011.

[68] B. N. J. Persson. Adhesion between an elastic body and a randomly rough hard surface. European Phys. J. E, 8:385–401, 2002.

[69] B. N. J. Persson and M. Scaraggi. Theory of adhesion: Role of surface roughness. J. Chem. Phys., 141:124701–1–14, 2014.

[70] B. N. J. Persson and E. Tosatti. The effect of surface roughness on the adhesion of elastic solids. J. Chem. Phys., 115:5597–5610, 2001.

[71] A. A. Pitenis, J. M. Uruena, E. O. McGhee, S. M. Hart, E. R. Reale, J. Kim, K. D. Schulze, S. L Marshall, A. I. Bennett, S. R. Niemi, T. E. Angelini, W. G. Sawyer, and A. C. Dunn. Challenges and opportunities in soft tribology. Tribology - Materials, Surfaces, & Interfaces, 11:180–186, 2017.

[72] B. Poerschke, S. Gorb, and C. F. Schaber. Adhesion of individual attachment setae of the spider cupiennius salei to substrates with different roughness and surface energy. Frontiers in Mech. Eng., 7:702297–1–11, 2021.

[73] R. S. Rivlin. Large elastic deformation of isotropic materials.iv.further developments of the general theory. Phil. Trans. R. Soc. London Ser. A - Math. and Phys. Sci., 241:379–397, 1948.

[74] R. S. Rivlin and D. W. Saunders. Large elastic deformation of isotropic materials.vii.experiments on the deformation of rubber. Phil. Trans. R. Soc. London Ser. A - Math. and Phys. Sci., 243:251–288, 1951.

[75] H. Q. She and M. K. Chaudhury. Estimation of adhesion hysteresis using rolling contact mechanics. Langmuir, 16:622–625, 2000.

[76] H. Q. She, D. Malotky, and M. K. Chaudhury. Estimation of adhesion hysteresis at polymer/oxide interfaces using rolling contact mechanics. Langmuir, 14:3090–3100, 1998.

[77] K. R. Shull. Contact mechanics and adhesion of soft solids. Mater. Sci. & Eng. R.-Reports, 36:1–45, 2002.

[78] L. J. Sliker, M. D. Kern, and M. E. Rentschler. An automated traction measurement platform and empirical model for evaluation of rolling micropatterned wheels. IEEE-ASME Trans. on Mechatronics, 20:1854–1862, 2015.

[79] S. A. Suresh, C. Kerst, M. Cutkosky, and E. Hawkes. Spatially variant microstructured adhesive with one-way friction. Interface, 16:20180705–1–8, 2019.

[80] T. Tang, C. Y. Hui, and N. J. Glassmaker. Can a fibrillar interface be stronger and tougher than a non-fibrillar one? J. Roy. Soc., Interface, 2:505–516, 2005.

[81] A. Tiwari, L. Dorogin, A. I. Bennett, K. D. Schulze, W. G. Sawyer, M. Tahir, G. Heinrichc, and B. N. J. Persson. The effect of surface roughness and viscoelasticity on rubber adhesion. Soft Matter, 13:3602–3621, 2017.

[82] L. R. G. Treloar. Elasticity and related properties of rubber. Rpt. on Prog. in Phys., 36:755–826, 1973.

[83] F. J. O. Varum, F. Veiga, J. S. Sousa, and A. W. Basit. Mucus thickness in the gastrointestinal tract of laboratory animals. J. Pharm. Pharmacol., 64:218–227, 2012.

[84] X. Wang, J. A. Schoen, and M. E. Rentschler. A quantitative comparison of soft tissue compressive viscoelastic model accuracy. J. Mech. Behav. Biomed. Mater., 20:126–136, 2013.

[85] X. D. Wang, H. B. Yu, T. Yang, X. F. Wang, T. Yang, Z. X. Ge, Y. B. Xie, X. Liao, P. W. Li, Z. Liu, and L. Q. Liu. Density regulation and localization of cell clusters by self-assembled femtosecond-laser fabricated micropillar arrays. ACS Appl. Mater. Interfaces, 13:58261–58269, 2021.

[86] H Wu, N. Moyle, A. Jagota, C. Y. Khripin, F. Bremond, and C. Y. Hui. Crack propagation pattern and trapping mechanism of rolling a rigid cylinder on a periodically structured surface. Extreme Mechanics Letters, 29:100475–1–9, 2019.

[87] J. Yeo, M. J. Choi, and D. S. Kim. Robust hydrophobic surfaces with various micropillar arrays. J. Micromech. Microeng., 20:025028–1–8, 2010.

[88] H. Yi, M. Kang, M. K. Kwak, and H. E. Jeong. Simple and reliable fabrication of bioinspired mushroom-shaped micropillars with precisely controlled tip geometries. ACS Appl. Mater. & Interfaces, 8:22671–22678, 2016.

[89] S. Yim and M. Sitti. Design and rolling locomotion of a magnetically actuated soft capsule endoscope. IEEE Trans. on Robotics, 28:183–194, 2012.

[90] Y. P. Zhao, L. S. Wang, and T. X. Yu. Mechanics of adhesion in mems - a review. J. Adh. Sci. and Tech., 17:519–546, 2003.

[91] S. Zilberman and B. N. J. Persson. Adhesion between elastic bodies with rough surfaces. Solid State Comm., 123:173–177, 2002.

Appendix A

Mechanical Characterization of Relevant Materials

Mechanical Properties of Poly(dimethylsiloxane)

A key consideration in reconciling experimental data with both analytical/empirical models and numerical simulations was the accurate characterization of the materials with which we were experimenting. The materials of concern in this case were Poly(dimethylsiloxane) (PDMS) and Poly(vinyl Chloride) (PVC). PDMS is a commonly used elastomer in biomimetic studies because it is biocompatible, optically clear, and there is an abundance of literature characterizing its mechanical properties. Because PDMS has been thoroughly characterized, we chose to use mechanical properties from the literature. At a 10:1 base:curing agent mix ratio, the consensus in the literature is that PDMS is an incompressible material ($\nu = 0.5$) with an initial modulus E_0 of 2.9 MPa [54, 18]. For the analytical/empirical models, which generally assume elastic behavior, this value was used for the Young's Modulus or, as appropriate, in the solution for the plane-strain modulus E^*. For numerical simulations, PDMS was modeled as a neo-hookean hyperelastic material with coefficient $C_{10} = 0.4833$. Although the neo-hookean model fails to capture non-linear behavior at high strain, this model still replicates experimental conditions accurately as the PDMS is roughly two orders or magnitude stiffer than the PVC (shown below) and thus experiences minimal strain.

Mechanical Properties of Poly(vinyl Chloride)

Characterization of the PVC was of greater concern because of its very high deformability and because our experimental configuration involved thin cylindrical shells of the material, necessitating that we consider finite thickness effects in our models. Thus, we determined it was worthwhile to characterize the PVC for three characteristics: elasticity, hyperelasticity, an viscoelasticity.

To test PVC's material properties, we formed PVC cylinders 40 mm in diameter and 20 mm in height. Two formulations were used: a 4:1 PVC:softener mix, which has been used commonly in our lab to mimic human tissue [78, 84, 54], and a purely PVC mix with no softener. All samples were vulcanized by heating to 175°C and degassed under vacuum. These samples were then subjected to two tests: a compression test to determine both small-strain elasticity and hyperelasticity, and a compress and dwell test to determine viscoelasticity.

The testing was conducting using a Dynamic Material Analyzer (DMA) (Test Resources, Shakopee, MN) with a 100-lb load cell. For the compression tests, the samples were compressed between two platens from 0-9 mm (0-45% strain) at a rate of 0.5 mm/s.

Hyperelastic Model for the large strain behavior of PVC

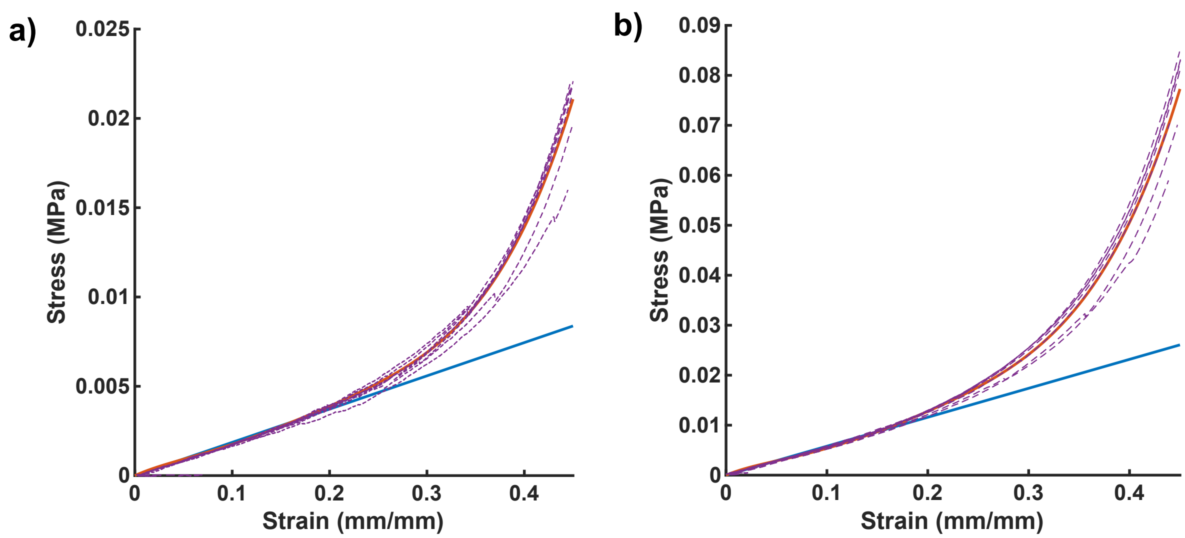

Figure A.1: Comparison of experimental results with linear and hyperelastic models for PVC formulations **(a)** 4:1 PVC:softener by volume and **(b)** no softening. The purple dashed lines represent data recorded using a DMA while compressing the samples from 0-45% strain. The blue line represents a linear fit applied to the small (0-15%) strain regime, while the red line represents a second-order polynomial fit.

The data from the compression tests was used to determine two characteristics. First, the portion of the data from 0-15% strain was used to create a linear fit between stress and strain to determine an initial Young's Modulus. Secondly, the entire stress-strain curve was used to determine an appropriate an appropriate hyperelastic model (discussed below) and solve for best-fit coefficients for the numerical material model. The experimental output, along with linear elastic and best hyperelastic model fit for both materials are shown in Figure A.1.

In fitting the stress-strain data to a hyperelastic model, three models were considered: neo-hookean, Ogden, and a second-order polynomial model. Because it fit the data substantially better than the other models, the second-order polynomial model was chosen and brief derivation follows.

Originally developed by Rivlin and Saunders [74], the Polynomial relates the the strain energy W to the strain invariants I_1 and I_2 as

$$W = \sum_{i=0,j=0}^{n} C_{ij} \left(I_1 - 3\right)^i \left(I_2 - 3\right)^j \tag{A.1}$$

where C_{ij} represent fitting coefficients.

In order to apply a curve fit, the strain invariants must first be related to physical quantities, in this case the stretch ratios λ_{1-3}. As described in [82], the three strain invariants can be expressed in terms of the stretch ratios as

$$I_1 = \lambda_1^2 + \lambda_2^2 + \lambda_3^2 \tag{A.2}$$

$$I_2 = \lambda_1^2\lambda_2^2 + \lambda_2^2\lambda_3^2 + \lambda_3^2\lambda_1^2 \tag{A.3}$$

$$I_3 = \lambda_1^2\lambda_2^2\lambda_3^2. \tag{A.4}$$

Further taking into account that the material is incompressible and is being subjected to a state of uniaxial normal stress, we can simplify the stretch ratios as follows:

$$\lambda_1 = \lambda \tag{A.5}$$

$$\lambda_2 = \lambda_3 = \lambda^{1/2} \tag{A.6}$$

which allows us to express the invariants in terms of the primary stretch variable λ as

$$I_1 = \lambda^2 + 2\lambda^{-1} \tag{A.7}$$

$$I_2 = \lambda^{-2} + 2\lambda \tag{A.8}$$

$$I_3 = 1. \tag{A.9}$$

To fit the curves, the engineering stress $j\sigma_e$ is equated to the stretch ratios and partial derivative of the strain energy as [73]:

$$\sigma_e = 2\left(\lambda - \lambda^{-2}\right)\left(\frac{\partial W}{\partial I_1} + \frac{1}{\lambda}\frac{\partial W}{\partial I_2}\right). \tag{A.10}$$

Using the expression for Strain Energy from Equation A.1, differentiating, and expressing the strain invariants in terms of the stretch ratio as per Equations A.7 and A.8, our curve-fitting expression becomes

$$\begin{aligned}\sigma_e = 2\left(\lambda - \lambda^{-2}\right)\big[C_{10} + C_{01}\lambda^{-1} + 2C_{20}\left(\lambda^2 + 2\lambda^{-1} - 3\right) \\ +2C_{02}\left(2\lambda + \lambda^{-2} - 3\right) + 3C_{11}\left(\lambda - 1 - \lambda^{-1} + \lambda^{-2}\right)\big].\end{aligned} \tag{A.11}$$

Using this relationship, the experimental data was fit using a standard MATLAB non-linear regression algorithm (nlinfit) to determine the appropriate fitting coefficients. The subsequent coefficients for each formulation are as follows:

Fitting Coefficients - PVC second-order polynomial model (MPa)		
	4:1 PVC:Softener	PVC Only
C_{01}	0.0344	0.1468
C_{10}	-0.0302	-0.1327
C_{11}	5.0248	19.1128
C_{02}	-5.8539	-22.2122
C_{20}	0.8903	3.3498

Table A.1: A listing of the second-order polynomial model fit coefficients for both formulations of PVC.

Using the second-order polynomial model to determine the initial elastic modulus $E_0 = 3\mu_0 = 6(C_{10} + C_{01})$, we find initial moduli of 25.2 kPa and 84.6 kPa, respectively, for the 4:1 and unmixed

PVC. These values are both slightly stiffer than the values determined from the linear fit in the small-strain regime, which were 18.6 kPa and 57.9 kPa.

Standard Linear Solid Model for the Viscoelastic Behavior of PVC

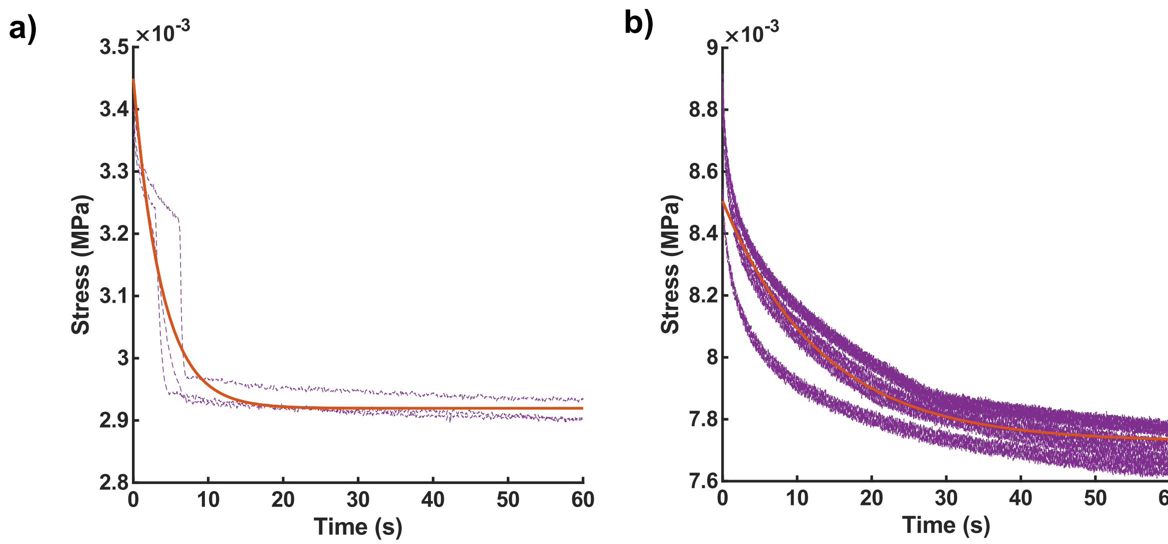

Figure A.2: Comparison of experimental results with the Standard Linear Solid (SLS) viscoelastic model for PVC formulations **(a)** 4:1 PVC:softener by volume and **(b)** no softener. The purple dashed lines represent data recorded during a 60 s dwell period following compression to 15% strain for each sample. The red line represents the SLS model comprised of an undamped equilibrium arm and Maxwell Arm with spring and damper in series.

To characterize the viscoelastic response of the PVC, the samples were compressed to a depth of 3 mm (15% strain) and held for a dwell time of 60 s to observe the stress relaxation. The data was then fitted to a Standard Linear Solid (SLS) model. The experimental data and subsequent best fit lines are shown for both materials in Figure A.2. In the SLS viscoelastic model, the material is modeled as a two-armed system. The first, or equilibrium, arm is modeled as a linear spring with no damping. The second, or Maxwell, arm, is modeled as a linear spring and dashpot in series. The two arms are then combined in parallel. For stress relaxation, the material is subjected to an initial strain which is then held constant as the stress relaxes. Under such conditions, the relationship of stress as a function of time is expressed as

$$\sigma(t) = \epsilon_0 \left(E_1 + E_2 \exp\left(-t/\tau\right)\right) \quad \text{(A.12)}$$

in which E_1 and E_2 represent the spring constants of the equilibrium and Maxwell arms, respectively, and τ is a time constant relating the dashpot viscosity η to the Maxwell spring constant as $\tau = \eta/E_2$. Fitting our experimental data from the compress and dwell experiments to this model, we determined the following constants:

Fitting Coefficients - SLS Viscoelastic Model		
	4:1 PVC:Softener	PVC Only
E_1 (kPa)	19.5	51.5
E_2 (kPa)	3.5	5.2
η (kPa-s)	13.3	69
τ (s)	3.8	13.3

Table A.2: A listing of the SLS viscoelastic model fit coefficients for both formulations of PVC.